



UNIVERSIDADE ESTADUAL DE CAMPINAS

Instituto de Física *Gleb Wataghin*

Diego Scolfaro da Silva

**Acoustic modulation of exciton
dynamics in transition metal
dichalcogenide monolayers**

**Modulação acústica da dinâmica excitônica em
monocamadas de dicalcogenetos de metais de
transição**

Campinas

2022

Diego Scolfaro da Silva

Acoustic modulation of exciton dynamics in transition metal dichalcogenide monolayers

Modulação acústica da dinâmica excitônica em monocamadas de dicalcogenetos de metais de transição

Tese apresentada ao Instituto de Física “Gleb Wataghin” da Universidade Estadual de Campinas como parte dos requisitos exigidos para a obtenção do título de Doutor em Ciências, na área de Física Aplicada.

Thesis presented to the Physics Institute “Gleb Wataghin” of the University of Campinas in partial fulfillment of the requirements for the degree of PhD in Science, the area of Applied Physics.

Orientador: Odilon Divino Damasceno Couto Junior

ESTE EXEMPLAR CORRESPONDE À VERSÃO FINAL DA TESE DEFE-
FENDIDA PELO ALUNO E ORIENTADA PELO PROF. DR. ODILON
DIVINO DAMASCENO COUTO JUNIOR

Campinas

2022

Ficha catalográfica
Universidade Estadual de Campinas
Biblioteca do Instituto de Física Gleb Wataghin
Lucimeire de Oliveira Silva da Rocha - CRB 8/9174

Si38a Silva, Diego Scolfaro da, 1992-
Acoustic modulation of exciton dynamics in transition metal dichalcogenide monolayers / Diego Scolfaro da Silva. – Campinas, SP : [s.n.], 2022.

Orientador: Odilon Divino Damasceno Couto Junior.
Tese (doutorado) – Universidade Estadual de Campinas, Instituto de Física Gleb Wataghin.

1. Metais de transição. 2. Ondas acústicas superficiais. 3. Efeito Stark. 4. Semicondutores. I. Couto Junior, Odilon Divino Damasceno, 1979-. II. Universidade Estadual de Campinas. Instituto de Física Gleb Wataghin. III. Título.

Informações para Biblioteca Digital

Título em outro idioma: Modulação acústica da dinâmica excitônica em monocamadas de dicalcogenetos de metais de transição

Palavras-chave em inglês:

Transition metals

Acoustic surface waves

Stark effect

Semiconductors

Área de concentração: Física Aplicada

Titulação: Doutor em Ciências

Banca examinadora:

Odilon Divino Damasceno Couto Junior [Orientador]

Pierre Louis de Assis

Antonio Riul Júnior

Yara Galvão Gobato

Jorlandio Francisco Felix

Data de defesa: 15-07-2022

Programa de Pós-Graduação: Física

Identificação e informações acadêmicas do(a) aluno(a)

- ORCID do autor: <https://orcid.org/0000-0003-1127-4990>

- Currículo Lattes do autor: <http://lattes.cnpq.br/3636859018525865>

MEMBROS DA COMISSÃO JULGADORA DA TESE DE DOUTORADO DO ALUNO DIEGO SCOLFARO DA SILVA - RA 108425 APRESENTADA E APROVADA AO INSTITUTO DE FÍSICA “GLEB WATAGHIN”, DA UNIVERSIDADE ESTADUAL DE CAMPINAS, EM 15/07/2022.

COMISSÃO JULGADORA:

- Prof. Dr. Odilon Divino Damasceno Couto Junior - Presidente e Orientador (IFGW/UNICAMP)
- Prof. Dr. Pierre Louis de Assis (IFGW/UNICAMP)
- Prof. Dr. Antonio Riul Junior (IFGW/UNICAMP)
- Dra. Yara Galvao Gobato (Universidade Federal de São Carlos)
- Dr. Jorlandio Francisco Felix (Instituto de Física - Universidade de Brasília)

OBS.: Ata da defesa com as respectivas assinaturas dos membros encontra-se no SIGA/Sistema de Fluxo de Dissertação/Tese e na Secretaria do Programa da Unidade.

Acknowledgements

Agradeço, primeiramente, a Deus e a Nossa Senhora pela proteção, pela força, pela coragem sem as quais nada teria sido possível.

Agradeço a meu orientador, Odilon, pela oportunidade de trabalhar no desenvolvimento deste projeto, pela orientação e pela formação que me foi dada e por ter me guiado e extraído o meu melhor neste processo. Agradeço muito também ao professor Fernando por toda a ajuda em diversos momentos e por ter me ensinado tanta coisa. Agradeço a ambos também pela amizade.

Agradeço ao Milton Tanabe por ter dado suporte para tudo que foi feito durante o meu doutorado e por tudo que me ensinou neste período.

Agradeço ao pessoal da Criogenia, especialmente o Milton e o Gustavo, e o André da oficina do DFMC por terem sido tão solícitos e prestativos. Agradeço também à secretaria do DFMC, em especial à Emília.

Agradeço a dona Isabel por ter cuidado com tanto carinho e atenção dos nossos ambientes de trabalho e por todo o carinho.

Agradeço à Dra. Bárbara Rosa e o prof. Dr. Ângelo Malachias (UFMG) pelas amostras de monocamadas de dicalcogenetos de metais de transição e pelas discussões.

Agradeço ao Dr. Paulo Santos (Paul-Drude Institute) por ter fornecido os dispositivos utilizados neste trabalho e pelas discussões.

Agradeço ao prof. Dr. Andrey Chaves (UFC) pelos cálculos de energia de ligação excitônica e pelas discussões.

Agradeço ao prof. Dr. Christoph Deneke pela pelas oportunidades que me foram dadas para participar de colaborações durante o meu doutorado.

Agradeço ao CCS Nano, especialmente a Emílio Bortolucci pelo auxílio com as caracterizações elétricas, a Luana Espindola pelo auxílio com a fotolitografia e José Eudoxio pelas medidas de elipsometria.

Agradeço ao LAMULT - IFGW e sua equipe por todo o apoio.

Agradeço a toda a equipe da secretaria de pós-graduação do IFGW por toda a estrutura e pela ajuda que me deram, especialmente para que tudo corresse bem na defesa.

Agradeço à extensão do IFGW por ter me alcançado há tanto tempo e ter despertado o meu interesse pela academia. Agradeço em especial à Viviane pela amizade em todos estes anos.

Dedico esta tese e todos os frutos deste trabalho a meus pais, Geraldo e Hosana. Sou muito grato a por o apoio, amor e carinho que me deram desde sempre. Dedico também à minha irmã Andréia, minha sobrinha Lara e meu cunhado Marcio.

Deixo meu agradecimento especial para a minha querida consagrada, a Natália, com quem eu divido minha vida. Amo você! Agradeço demais aos seus pais, José Roberto e Vanda, e suas irmãs, Dimíttria e Vitória (você também, Celso!) por serem tão carinhosos e me dado tanta força e apoio, além de terem me acolhido como parte da família.

Agradeço muito a meus amigos Gustavo, Marcos, Hiro, Paola, Wagner, Alexandre e Vanessa por terem me ajudado tanto neste período do doutorado, tanto no pessoal quanto no profissional.

Agradeço aos meus amigos do GPO, que se tornaram pessoas muito importantes para mim: Matheus, Luca, Diego, Bethânia, Marcos, Ailton, Augusto e João Victor.

Agradeço ao Ministério da Ciência, Tecnologia e Inovações, ao Conselho Nacional de Desenvolvimento Científico e Tecnológico – CNPq e à Fundação de Amparo à Pesquisa do Estado de São Paulo - FAPESP (processo FAPESP 12/11382-9) pelo apoio financeiro. Agradeço também à UNICAMP por fornecer toda a estrutura de pesquisa e vivência que me possibilitaram a realização deste trabalho.

Por fim, agradeço também aos que vieram antes de mim e saúdo a estrutura de pesquisa que foi construída no Brasil que, apesar dos tempos sombrios, há de crescer cada vez mais.

Abstract

Two-dimensional transition metal dichalcogenide (TMD) monolayers (MLs) have attracted attention of the scientific and technological communities due to the robustness of their singular optical properties, such as spin-valley effects and efficient photoluminescence (PL) emission at room temperature. Surface acoustic waves (SAWs) have been employed as an efficient tool to manipulate and transport elementary excitations, such as charge carriers and spins in low-dimensional III-V semiconductor systems. In this work, we tune the optical emission energies and dissociate neutral and charged excitonic states in MoSe₂ and MoS₂ MLs employing the in-plane piezoelectric field carried by propagating SAW beams. We transfer the MLs to high dielectric constant piezoelectric LiNbO₃ substrates, where the neutral exciton binding energy is reduced, allowing us to efficiently quench (above 90 %) and redshift the excitonic optical emissions. Time transient measurements show that the PL quenching is progressively built after the SAW is turned on. Quenching time ranges from 30 seconds to 2 minutes, which is consistent with experimental evidences of electron trapping and release processes at potential fluctuations during transport induced by the SAW in-plane electric field. A model for the acoustically-induced Stark effect allows us to obtain neutral exciton and trion in-plane polarizabilities as $530 \times 10^5 \text{ meV}/(\text{kV}/\text{cm})^2$ and $630 \times 10^5 \text{ meV}/(\text{kV}/\text{cm})^2$, respectively. Our findings open new possibilities to manipulate and modulate multi-exciton interactions in two-dimensional semiconductor systems for novel optoelectronic applications.

Keywords: Transition Metals, Surface acoustic waves, Stark effect, Semiconductors.

Resumo

Monocamadas (MLs) bidimensionais de dicalcogenetos de metais de transição (TMD) tem atraído a atenção das comunidades científica e tecnológica devido à robustez de suas propriedades ópticas singulares, como efeitos spin-valley e emissão de fotoluminescência (PL) eficiente à temperatura ambiente. Ondas acústicas de superfície (SAWs) tem sido empregadas como uma ferramenta eficiente para manipular e transportar excitações elementares, como portadores de carga e spins em sistemas semicondutores III-V de baixa dimensionalidade. Neste trabalho, sintonizamos as energias de emissão óptica e dissociamos estados excitônicos neutros e carregados em MLs de MoSe₂ e MoS₂ empregando o campo piezoelétrico transportado pela SAW. Nós transferimos as MLs para substratos piezoelétricos de LiNbO₃ de alta constante dielétrica, onde a energia de ligação do exciton neutro é reduzida, permitindo-nos suprimir de maneira eficiente a intensidade de PL (acima de 90%) e deslocar as emissões ópticas excitônicas. Medidas de transientes de tempo mostram que o *quenching* PL é construído progressivamente depois que a SAW é ligada. O tempo típico de *quenching* varia de 30 segundos a 2 minutos, o que é consistente com evidências experimentais dos processos de captura e liberação de portadores de carga em flutuações de potencial ao longo do caminho de transporte da SAW. Um modelo para o efeito Stark induzido pela SAW nos permite obter as polarizabilidades no plano para o exciton neutro e o trion negativo como 530×10^5 meV/(kV/cm)² e 630×10^5 meV/(kV/cm)², respectivamente. Nossas descobertas abrem novas possibilidades para manipular e modular interações multi-exciton em sistemas semicondutores para novas aplicações optoeletrônicas.

Palavras-chave: Metais de transição, Ondas acústicas superficiais, Efeito Stark, Semicondutores.

List of acronyms

Acronym	Meaning
a_H	Hydrogen Bohr radius
a_X^{3D}	Effective three-dimensional exciton radius
a_X^{2D}	Effective two-dimensional exciton radius
α_{X^0}	Neutral exciton in-plane polarizability
α_{X^-}	Negative trion in-plane polarizability
c_{ijkl}	Stiffness tensor
c	Speed of light
CW	Continuous wave
CB	Conduction band
CVD	Chemical vapour deposition
$\frac{\delta V}{V}$	Volumetric strain
ΔE_{SO}^{CB}	Conduction band spin-splitting energy
ΔE_{SO}^{VB}	Valence band spin-splitting energy
ΔE_{Stark}	Stark effect-related energy modulation
ΔE_{Strain}	Strain-induced energy modulation
e	Electron charge
e_{ijl}	piezoelectric tensor
E_B^{3D}	Three-dimensional neutral exciton binding energy
E_B^{2D}	Two-dimensional neutral exciton binding energy
E_{X^0}	Neutral exciton emission energy
E_{X^-}	Negative trion emission energy

$E_B^{X_0}$	Neutral exciton binding energy
$E_B^{X^-}$	Negative trion binding energy
E_{GAP}	Bandgap energy
E_1	In-plane SAW piezoelectric field
E_3	Out-of-plane SAW piezoelectric field
ε	Dielectric constant
$\bar{\varepsilon}$	Average dielectric constant
ε_{TMD}	TMD dielectric constant
ε_T	Top material dielectric constant
ε_B	Bottom material dielectric constant
ε_0	Electric permittivity of free-space
ε_{eff}	Effective dielectric constant (full potential model)
ε^{\parallel}	In-plane component of the dielectric constant
ε^{\perp}	Out-of-plane component of the dielectric constant
ϵ_{kl}	Dielectric tensor
f_n	Oscillator strenght of n -th exciton state
ϕ_{SAW}	SAW piezoelectric potential
FET	Field-effect transistor
FEUDT	Floating Electrode Unidirectional Transducer
FEM	Finite elements methods
Γ_0^{rad}	Radiative decay rate
GaAs	Gallium arsenide
GaN	Gallium nitride
H_0	Zero order Struve function
h-BN	hexagonal Boron Nitrate
\hbar	Reduced Plank constant
IDT	Interdigital Transducer
I_{PL}	Photoluminescence intensity
J_0	Zero order Bessel function

k^2	Electromechanical coupling coefficient
K, K', Γ , M	First Brillouin zone symmetry points
K_{exc}	Exciton center-of-mass momentum
k_0	Light wave-vector
λ_{SAW}	SAW wavelength
LiNbO ₃	Lithium niobate
LS	Localized states
μ	Effective mass
μ PL	Micro-photoluminescence
MoS ₂	Molybdenum disulfide
MoSe ₂	Molybdenum diselenide
MBE	Molecular beam epitaxy
ML	Monolayer
m_0	Electron rest mass
m_e	Electron effective mass
m_h	Hole effective mass
Mo	Molybdenum
n	Principal quantum number
N_P	Number of periods in a SAW-generating device
PL	Photoluminescence
P_{RF}	RF input power
P_{SAW}	SAW output power
P_{exc}	Laser excitation power
PML	Perfectly matched layer
Q_{PL}	Photoluminescence quenching degree
ρ^{POL}	Degree of spin polarization
RF	Radio-frequency
R_H	Hydrogen Rydberg constant
R_X	Exciton Rydberg constant

r_0	Exciton screening length
SAW	Surface acoustic wave
σ^+	Right-handed circularly polarized light
σ^-	Left-handed circularly polarized light
Si	Silicon
SiO ₂	Silicon dioxide
S_{ii}	Electrical reflection coefficient
$S_{ij}, i \neq j$	Electrical transmission coefficient
\hat{S}_{ij}	Strain
SO	Spin-orbit
t_{on}	Time instant in which the SAW is turned on
t_{off}	Time instant in which the SAW is turned off
τ_{dis}^{-1}	Field-induced exciton dissociation rate
τ_0^{rad}	Radiative lifetime
T_{ij}	Stress
TMD	Transition metal dichalcogenides
V_{e-h}^{2D}	Two-dimensional electron-hole Coulomb potential
V_{e-h}^{RK}	Rytova-Keldysh interaction potential
VB	Valence band
X^0	Neutral exciton
X^-	Negative trion
Y_0	Zero order Neumann function
WS ₂	Tungsten disulfide
WSe ₂	Tungsten diselenide
W	Tungsten
W_A	SAW-generating device aperture

List of Figures

2.1	Highlighted elements that form about 40 different known layered TMD compounds. Transition metals from groups 4 to 7 tend to form thermodynamically stable layered TMD. Extracted from [7]	36
2.2	(a) Schematic representation of a typical MX_2 structure, with the chalcogen atoms (X) in black and the metal atoms (M) in red. The gray surface represents the substrate. Two MLs are represented to illustrate the stacking. The addition of more MLs forms the bulk. (b) Trigonal prismatic (2H) coordination. (c) Side view of lattice structure of 2D TMD in the t2H) coordination. (d) Top view of the honeycomb lattice of 2D TMD in the trigonal prismatic coordination. (e) Atomic structure of a single layer of a TMD exhibiting the lack of spatial inversion symmetry. (f) First Brillouin zone of the TMD showing the main symmetry points Γ , M, K and K'	37
2.3	Evolution of the electronic band structure of semiconductor MoS_2 as the sample is thinned from bulk to ML, calculated using Density Functional Theory. As the number of layers is decreased, the indirect energy gap increases between points Γ^V and Λ^C . For the the ML limit, a direct energy gap is observed at the K point. Extracted and adapted from [9].	39

2.4	General electronic band structure of the MoX ₂ TMD ML systems. Non-equivalent K (left) and K' (right) valleys of the Brillouin zone (represented on the top) are locked to opposite spin states due to time-reversal symmetry. The subsequent optical selection rules for the A excitons allow selective excitation of K (K') valley through σ^+ (σ^-) excitation and the ground state is optically active (bright) for MoX ₂ . The B excitons are also represented for the K valley.	41
2.5	(a) Representation of the X ⁰ and the X ⁻ quasi-particles on the TMD structure. Red and blue circles represent the electrons and holes, respectively. (b) Energy diagram showing the X ⁰ ground (n=1) and excited (n=2, 3... and the continuum) states and the X ⁻ ground state. The X ⁰ binding energy $E_B^{X^0}$ is the difference between E_{GAP} and the exciton energy E_{X^0} . The trion energy level lies below the X ⁰ ground state with an energy separation of $E_B^{X^-}$, the trion binding energy. The excited states of the X ⁻ are not represented. E_{X^0} and E_{X^-} are commonly observed in PL experiments.	44
2.6	(a) Real-space representation of a 3D exciton in a bulk system, where field lines are screened inside the material. (b) Typical absorption spectrum of a 3D system, with the $1/n^2$ hydrogenic series of the exciton states.	45
2.7	(a) Side view of a TMD ML with the representation of a 2D exciton. The ML is sandwiched between two materials with dielectric constants ϵ_B (bottom) and ϵ_T (top) which are permeated by the electric field the X ⁰ . (b) Representation of a typical absorption spectrum of a 2D system system with excitonic interaction.	46

2.8	Neutral exciton binding energy (E_B^{X0}) as a function of the substrate dielectric constant ε_B calculated using the 2D Hydrogen model (red), the Rytova-Keldysh approximation (blue), and the full interaction potential [94] (green). The dielectric constants of LiNbO_3 (≈ 56) and h-BN (≈ 4) are indicated by the vertical lines. The calculations were carried out by Andrey Chaves (Departamento de Física - Universidade Federal do Ceará).	53
2.9	Side view of a TMD ML with the representation of a 2D exciton. The dielectric environment is not uniform within the ML, since each atomic sheet exhibits a different electric susceptibilities χ_1 and χ_2 . The screening from the chalcogen sheets helps to confine the field lines of the trion within the ML, reducing the dependence on the surrounding materials. On the other hand, the neutral exciton field lines leak outside the ML and a more pronounced dependence is observed on the top and bottom materials.	55
2.10	Exciton dynamics in a single-particle picture. Excitons are formed with a finite center-of-mass momentum K_{exc} . Through phonon scattering, excitons relax (cyan arrows) into the light cone, which is marked by the free-space photon dispersion ck_0 , and decay radiatively (purple arrow) with a lifetime τ_{eff}^{rad} . However, at finite temperatures, optically active excitons can be re-scattered (cyan arrows) away from the light cone, causing the thermal population to extend beyond the light cone edge k_0 and increasing the radiative lifetime as a consequence. Adapted from [5]	56

2.11	Neutral exciton radius (a_X^{2D}) as a function of the substrate dielectric constant ϵ_B calculated using the 2D Hydrogen model (red), the Rytova-Keldysh approximation (blue), and the full interaction potential [94] (green). The dielectric constants of LiNbO ₃ (≈ 56) and h-BN (≈ 4) are indicated by the vertical lines. The calculations of a_X^{2D} were carried out by Andrey Chaves (Departamento de Física - Universidade Federal do Ceará).	58
3.1	Illustration of an extensible string that is fixed to a rigid wall on the left and is being pulled to the right. The string undergoes elastic deformation, increasing its length (L). At the top, the string is unstressed and the points A and B, which are located in x and $x + \Delta x$, respectively. At the bottom, the string is stressed by the application of an external force \vec{F} , which causes the points A and B to be displaced to points A' and B' located in x' and $x' + \Delta x'$, respectively. The total length increases from L to $L + \Delta L$. Adapted from [115]. . .	62
3.2	Representation of different elastic modes in solids. (a) Bulk longitudinal (compressive) wave. (b) Bulk transverse (shear) wave. (c) Rayleigh wave. Adapted from [114].	68
3.3	Representation of the piezoelectric effect. In the absence of a net stress (a) the piezoelectric crystal is charge-balanced and no electric field is induced. However the application of compressive (b) and tensile (c) stresses lead to opposite charge unbalances.	69
3.4	Strain profile of a propagating Rayleigh wave with wavelength λ_{SAW} and velocity v_{SAW} in the x_1 direction. The regions of compression and tension are indicated in blue and red, respectively. The particle exhibits an elliptic motion due to the superposition of transverse and longitudinal modes.	71

3.5	Type-I (a) and type-II SAW-induced carrier spatial separation along the propagatino direction (x_1). In the type-I spatial modulation, the mechanical displacement traps the charge carriers in the same position. On the other hand, in the type-II spatial modulation electrons and holes are trapped with a separation of $\lambda_{SAW}/2$ due to the piezoelectric potential.	78
4.1	Illustration of a bidirectional (a) single-finger and (b) double-finger IDTs. The RF input launches SAW beams on both sides side of the transducer. Finger width (L_f), aperture (W_A), and SAW wavelength λ_{SAW} are indicated.	83
4.2	Schematic illustration of the stages of the photolithography fabrication.	84
4.3	Micrographs of a single-finger (a) and a double-finger (b) IDT fabricated on Y-128° LiNbO ₃ substrate.	86
4.4	Representation of RF electrical reflection and transmission measurements. The electrical input signal is applied (green) through port 1 on IDT A. Part of the signal is reflected (red) and read at port 1. Part of the signal is converted into SAW (beige arrows and green speaker), which propagates through the substrate until it reaches IDT B and induces an electrical signal (output from IDT B) that can be read at port 2.	87
4.5	Measured Rf reflection (orange) and transmission (green) coefficient spectra of a single-finger delay line in (a) and (b) and a double-finger delay line in (c) and (d), respectively.	88
4.6	Bidirectional IDT equivalent circuit. Adapted from [120].	90
4.7	Acoustic conductance spectra (black) of single-finger (a) and double-finger (b) IDTs. The red curve is the fitting with the proposed model. The curves are obtained from the experimental data shown in Figure 4.5.	91

4.8	Illustration of the FEUDT transducer that was used in the modulation experiments. The RF input excites a single SAW beam to the right of the device (in the case of the illustration). Values of finger widths are indicated. The finger spacing is $1 \mu\text{m}$ so $\lambda_{SAW} = 35 \mu\text{m}$. We used devices with aperture values of $212 \mu\text{m}$ and $424 \mu\text{m}$	94
4.9	Experimental setup for μPL spectroscopy measurements. Linearly polarized laser ($\lambda = 457\text{nm}$ or $\lambda = 532\text{nm}$), selected using a flip mirror, becomes circularly polarized after passing a quarter waveplate; an objective focuses the beam on the sample inside the cold finger cryostat; the emitted PL is collected by the same objective. Before entering the monochromator, the p (PL_P) and s (PL_S) components are separated by a polarization displacement prism and simultaneously detected in different areas of a CCD camera. SAW is generated on the sample using a RF generator. Network analyzer is used to characterize the SAW generating devices. The cryostat also has a positioning system which is used to move the sample and allows the PL mapping. The setup is controlled by a computer. Representation of the setup was constructed using the ComponentLibrary by Alexander Franzen.	96
4.10	Device illustration: the SAW beam is launched along the x direction by a FEUDT towards the TMD ML, where PL is excited by a focused laser beam and collected by an optical objective (not shown).	97
4.11	Optical micrographs of the MoS_2 (a) and MoSe_2 (b) MLs, respectively, and the SAW generating device used with each one, taken with 5X magnification. The approximate position of the MLs are indicated by the black arrows. (c) Representation of a ML positioned in front of the FEUDT output indicating that it lies on the acoustic path.	98

5.1	Representation of the model used for the numerical calculations. (a) Three-dimensional representation of the SAW-generating FEUDT device on the LiNbO ₃ substrate with a cut of the 2D model. The electric potential is highlighted in each finger of the device where the RF potential (V_{RF}), ground and floating potential ($V=0$) are represented in red, blue and green respectively. The 2D cut shows a single period of the model employed on the calculations. (b) Representation of the complete 2D model with the device fingers and the TMD ML (in red). The electric boundary conditions are the same of (a) but we point the presence of the PML. Elements are not in scale.	100
5.2	Discretization of the 2D model showing the mesh of the substrate, FEUDT fingers and the PML. The TML ML is not visible due to the small thickness.	102
5.3	Measured (blue solid line) and calculated (orange solid line) S_{11} parameter for the three lower acoustic resonances of the FEUDT device.	103
5.4	Two-dimensional plots of (a) the total particle displacement; and (b) the piezoelectric potential of the SAW simulated for the FEUDT resonance at 225 MHz.	104
5.5	Piezoelectric field and hydrostatic strain frequency sweep. (a) Piezoelectric field: in-plane piezoelectric field (E_1) calculated on the LiNbO ₃ surface (blue) and at the MoSe ₂ ML (green). The out-of-plane piezoelectric field component (E_3) is also calculated on the LiNbO ₃ surface (red) and at the MoSe ₂ ML (orange). (b) Hydrostatic strain component ($\frac{\delta V}{V}$) at the LiNbO ₃ substrate without the ML (blue circles) and at the MoSe ₂ ML (green circles).	105
6.1	(a) Optical microscopy image of the MoSe ₂ sample showing the ML. (b) Low-temperature μ PL spectra of the MoSe ₂ ML acquired with a 457nm laser at an excitation power of 100 μ W with a 100X objective lens in the absence of a SAW beam.	108

6.2	(a) Optical microscopy image of the MoS ₂ sample, in which the ML is outlined in yellow. (b) Low-temperature μ PL spectra of the MoS ₂ acquired with a 457nm laser at an excitation power of 350 μ W with a 100X objective lens in the absence of a SAW beam (blue) and in presence of a 25dBm SAW beam (orange). (c) Low-temperature μ PL spectrum of the MoS ₂ after the degradation. Measurement was carried out using a 532nm laser at an excitation power of 1mW with a 20X objective lens in the absence of a SAW beam.	110
6.3	Map of the MoSe ₂ ML PL emission as a function of time recorded at 5 K with 100 μ W laser excitation. The white horizontal dashed lines indicate when the SAW ($E_1 = 24$ kV/cm) is turned on and off during the experiment. The horizontal orange lines indicate the time window of 2 minutes from where PL is averaged to calculate Q_{PL} . The white spectrum illustrates the PL emission before the SAW is turned on.	111
6.4	Spectral regions used to integrate the individual emission lines of the MoSe ₂ ML in the absence of SAW (a), and under the maximum applied SAW power (b). We indicate the X^0 and X^- regions in green and red, respectively.	112
6.5	Fits of the PL decay (red solid line) and recovery (cyan solid line) transients of the X^- emission line when the sample is submitted to a 24 kV/cm in-plane field of the SAW.	113
6.6	Fast PL decay component (τ_{q1}) as a function of SAW E_1 for the X^- (blue circles) and X^0 (red circles) emission lines of the MoSe ₂ ML and the $X^0 + X^-$ (green squares) and LS (orange squares) emission bands of the MoS ₂ ML.	114
6.7	Slow PL decay component (τ_{q2}) as a function of E_1 for the X^- emission of the MoSe ₂ ML.	115

6.8	PL recovery (τ_r) time as a function of SAW E_1 for X^- (blue circles) and X_0 (red circles) emission lines of the MoSe ₂ ML and the $X^0 + X^-$ (green squares) and LS (orange squares) emission bands of the MoS ₂ ML.	116
6.9	Illustration of the conduction and valence bands potential fluctuations along the carrier transport path. The SAW modulated piezoelectric potential ϕ_{SAW} (not to scale with the potential fluctuations) is represented by the dashed line.	118
6.10	Time transients of X^- (a) and X^0 (b) emissions of the MoSe ₂ ML sample and excitonic ($X^0 + X^-$) (c) and defect-related (d) emission bands of the MoS ₂ ML sample for different values of E_1	120
6.11	PL quenching (Q_{PL}) as a function of E_1 for X^- (blue circles) and X_0 (red circles) emission lines of the MoSe ₂ ML and $X^0 + X^-$ (green squares) and LS (orange squares) emission bands of the MoS ₂ ML. . .	121
6.12	(a) PL spectra of the MoS ₂ ML and the LiNbO ₃ substrate before and after a SAW beam with 9kV/cm in-plane electric field is turned on. (b) Degree of Q_{PL} achieved in the SAW experiments conducted on the MoS ₂ ML and the LiNbO ₃ substrate. Q_{PL} of the substrate is calculated using the same spectral window of each emission band of the ML.	122
6.13	PL quenching (Q_{PL}) as function of the temperature for $X^0 + X^-$ (green squares) and LS (orange triangles) emission bands of the MoS ₂ ML.	123
6.14	Q_{PL} as function of P_{exc} for the $X^0 + X^-$ and LS emission bands of the MoS ₂ ML at 5K (blue and cyan, respectively) and 78K (dark and light green, respectively).	124
6.15	PL saturated quenching map of the MoSe ₂ X^0 and X^- emission lines at the highest acoustic power applied on this sample (26 dBm). White dashed line is a guide for the eye. The map starts and finishes at the minutes 10 and 25, when the SAW is turned on and off, respectively. .	125

6.16	X^- and X^0 intensity ratio $I_{PL}^{X^-}/I_{PL}^{X^0}$ as a function of E_1	127
6.17	Field-induced dissociation rate τ_{dis}^{-1} as a function of the SAW in-plane electric field E_1 . τ_{dis}^{-1} is calculated with Equation 3.43 for the neutral exciton on SiO_2 substrate (orange circles) where $E_B^{X^0} = 500$ meV, neutral exciton (purple circles) and negative trion (green circles) on LiNbO_3 substrate, where $E_B^{X^0} = 52$ meV and $E_B^{X^0} = 35$ meV respectively.	128
6.18	MoSe_2 (a) and MoS_2 (b) ML PL spectra (average for 2 minutes) before the SAW is turned on (blue) and for different in-plane SAW fields (remaining spectra) before it is turned off. The inset in (a) shows the normalized PL intensity in the absence of a SAW (in blue) and with a 50 kV/cm in-plane SAW piezoelectric field E_1 (in purple) indicating the redshift of X^0 and X^- emission lines.	130
6.19	MoSe_2 X^- (blue circles) and X^0 (red circles) emissions redshift (ΔE) as a function E_1 . The gray dashed line is the calculated hydrostatic strain contribution (ΔE_{strain}). The solid blue and red lines are fits to the experimental data of X^- and X^0 emissions, respectively. The dashed cyan and orange lines are the Stark shift contributions (ΔE_{Stark}) to ΔE extracted from the fits. The values of ΔE for the $X^0 + X^-$ emission of MoS_2 (green squares) are also shown.	131

List of Tables

2.1	Values of E_{GAP} , ΔE_{SO}^{CB} , ΔE_{SO}^{VB} and the neutral exciton binding energy $E_B^{X^0}$ of the main TMDs of the group VI in the ML form. Values were extracted from Ref. [17].	42
2.2	Measured and calculated values of $E_B^{X^-}$ for MoSe ₂ ML. The calculated values were extracted from Ref. [103].	54
2.3	Measured and calculated values of τ_{rad}^0 for the neutral exciton of the MoSe ₂ ML. The calculated values were extracted from Ref. [111]. . .	57
3.1	Characteristics of piezoelectric materials related to generation and propagation of SAWs and PSAWs. Adapted from Refs. [50,116]. . .	74
4.1	Electric and acoustic parameters of the IDTs extracted from the electric characterization measurements.	92
5.1	Calculated amplitude of the SAW in-plane piezoelectric field (E_1) at the sample for each nominal RF input power (P_{RF}) used on the experiments.	106
6.1	Values of X^0 and X^- in-plane polarizabilities (α) of MoSe ₂ and WSe ₂ MLs placed on different substrates, which are labeled by the dielectric constant ε in terms of the vacuum permittivity (ε_0).	132

Acknowledgements

Abstract

Resumo

List of acronyms

List of figures

List of tables

1	Introduction	28
1.1	Transition Metal Dichalcogenides	28
1.2	Surface Acoustic Waves	31
1.3	Acoustic Modulation of TMDs	32
1.4	This Thesis	33
2	Two-Dimensional Transition Metal Dichalcogenides	35
2.1	Crystal structure	35
2.2	Band structure	38
2.3	Exciton dynamics	43
2.3.1	Hydrogen model approximation	44
2.3.2	Rytova-Keldysh model	48
2.3.3	Full-interaction potential	50

2.3.4	Trion binding energy	54
2.3.5	Exciton radiative lifetime	55
3	Surface Acoustic Waves	60
3.1	Wave propagation in piezoelectric solids	60
3.1.1	Strain	60
3.1.2	Stress	63
3.1.3	Generalized Hooke's law	64
3.1.4	Matrix notation	65
3.1.5	Equation of motion in non-piezoelectric solids	66
3.1.6	Piezoelectricity	67
3.1.7	Wave equation for piezoelectric solids	70
3.2	The Rayleigh mode in piezoelectric solids	70
3.2.1	Rayleigh waves in LiNbO_3	73
3.3	Acoustic modulation	76
3.3.1	Exciton dynamics modulation	76
3.3.2	Acoustic transport and exciton dissociation	77
3.4	SAWs in 2D TMDs	79
4	Experimental methods	82
4.1	SAW generation and detection	82
4.1.1	Interdigital transducers for SAW generation	82
4.1.2	Fabrication	83
4.1.3	Electrical characterization - Scattering parameters	86
4.1.4	Extraction of acoustic parameters	89
4.1.5	Unidirectional transducers	92
4.2	Acoustic modulation experiments	94
4.2.1	Optical spectroscopy setup	94
4.2.2	Optical spectroscopy measurements	95
4.2.3	The samples	98

5	Computational methods	99
5.1	Simulation model	99
5.2	SAW strain field and piezoelectric potential	102
6	SAW-driven carrier dynamics in MoX₂ monolayers	107
6.1	PL emission in the absence of a SAW	108
6.2	Acoustically modulated PL spectroscopy	111
6.3	PL quenching dynamics	113
6.4	SAW-induced PL quenching degree	118
6.4.1	Acoustic power	119
6.4.2	Temperature	123
6.4.3	Laser power	123
6.4.4	Thermal stability	124
6.5	Exciton dissociation	126
6.6	SAW-induced excitonic Stark effect	129
7	Conclusions	134
8	Publications	136
	Bibliography	136

CHAPTER 1

Introduction

This introductory chapter brings the basic description of Transition Metal Dicalchogenides (TMDs) and surface acoustic waves (SAWs) along with the contextualization of this work, based on the state of art of the interface between TMDs and SAWs. At first, we bring the basic physical phenomena involving TMDs, which is our system of interest, and put it as a platform for basic research and technology development. In addition, we discuss different approaches of using external fields to manipulate exciton dynamics and light emission properties in such material. In sequence, we present SAWs as a tool which is widely employed in technological development and manipulation of elementary excitations, such as charge carriers, spins and excitons, in solid media. Furthermore, we bring the state of art of the interface of SAWs with TMD systems and discuss the main results of the literature. The final section brings the outline of this thesis.

1.1 Transition Metal Dicalchogenides

The attention of the scientific community turned to the use of 2D systems for the development of nanotechnology platforms and basic research after the emergence of graphene in the works of Novoselov and coworkers [1, 2] in the early 2000's. Graphene exhibits very attractive physical properties such as high carrier mobility, optical transparency, high Young modulus, and excellent thermal transport, which led to the development of a wide variety of devices in the contexts of electronics and

photonics [3,4]. Despite the outstanding set of physical properties of graphene, the absence of a bandgap imposes a limit for its potential employment in light-emitting devices, for example. This fact has opened a new research field in the direction of incorporating the finite bandgap characteristics to the list of graphene properties. The initial efforts pointed to the possibility of opening a bandgap by the use of doping, and the application of external fields [3] but eventually turned into the search for different 2D materials.

Due to the advanced capability of production, handling, and characterization of ultrathin atomic layers gained with the graphene-based research [5], a huge variety of novel 2D materials has been discovered and investigated in the last decade, reaching over 150 families of materials such as TMDs, hexagonal boron nitride (h-BN), black phosphorous (BP), transition metal halides, transition metal oxides, and perovskite-type oxides [6].

The TMD family is a class of more than 40 composites [5,7] which exhibits as main characteristics (i) a layered structure and (ii) a general chemical composition on the form MX_2 , where M is a transition metal and X represents a chalcogen atom. Such materials can be thinned down to few-layered structures and even monolayers (MLs), exhibiting substantially different properties from the bulk form as a consequence of the reduction of dimensionality and symmetry. In particular TMDs of VII group ($\text{M} = \text{Mo}, \text{W}$) are semiconductors that exhibit an indirect bandgap when comprised of two or more layers, and a direct bandgap when in ML form. This indirect-to-direct change is responsible for an intense light emission of the MLs when compared to bulk and few-layered systems, as observed simultaneously by Mak [8] and Splendiani [9] in 2010.

The 2D TMDs have attracted attention due to pronounced excitonic resonances even at room temperature and unique multi-exciton and spin-valley properties [5,10–16]. The neutral exciton binding energy reaches up to 600 meV [17] under the conditions of weak dielectric screening, which is commonly achieved in substrates with low dielectric constant as compared to the TMD, such as SiO_2 or h-BN [5]. Moreover, the reduced dimensionality causes the electronic properties to

be highly sensitive to the environment [18].

Besides single MLs, Van der Waals (VdW) heterostructures comprised of stacked MLs of different TMDs have been fabricated [19] allowing the observation of interlayer exciton features [20, 21], which are excitonic complexes whose constituents comes from different layers, and the presence of different electronic phases in twisted bilayers with different properties, such as superconductivity [22]. Currently, optically inactive excitons [23–26] and the emission of single photon via localized states [27–29] also have attracted the attention of the community [16].

From an application point of view, the first MoS₂ ML field-effect transistor (FET) has been demonstrated in 2011 by Kis and coworkers [30], which led to the fabrication of atomically thin phototransistors [31] in 2012 by Yin and coworkers. Furthermore, 2D TMD-based p–n junctions allowed for the realization of optoelectronic and photovoltaic devices such as light-emitting diodes and solar cells [16]. In particular, the achievability of a near-unity photon quantum yield in TMD MLs, as demonstrated by Amani and coworkers [32] created the expectation of highly efficient devices based on the manipulation of charge carriers, spins, and excitonic complexes.

Many different approaches have been employed to manipulate excitonic optical emissions in these 2D systems. Optical fields [33, 34] as well as in-plane [35–39] and out-of-plane [40, 41] electric fields in field-effect devices have been employed to tune emission energies and to dissociate excitons via the Stark effect. Static mechanical strain has also been used to tune emission energies [42, 43], induce direct-to-indirect band gap transition [44, 45], and change the performance of optical devices [46, 47]. However, the large effective masses and exciton binding energies (compared to III-V semiconductor nanostructures) as well as the strong dependence of the MLs response on their surroundings are some of the main challenges to achieve on-demand exciton manipulation in TMD MLs [13, 18].

1.2 Surface Acoustic Waves

Over the past decades, technological development and innovation were based on the control of elementary excitations in solid state media such as electrons, photons, spins and phonons [48]. On the other hand, phononic devices are very interesting due to the possibility of using phonons to carry energy and information, besides interacting with electrons and photons, in a very broad range of technological applications ranging from nanoelectronics to quantum technologies and even medical therapy [49].

Elastic waves propagate in solid media at relatively low velocities as compared to those of electromagnetic waves. Typical elastic wave velocities in solids range approximately from 1 to 10^3 m/s, being approximately 10^5 times slower than characteristic velocities for electromagnetic waves. Such a huge difference results in a much smaller wavelength for a given frequency. Therefore, elastic wave resonators are typically 10^5 times smaller than an electromagnetic counterpart and are able to fit into small chip for signal processing [48].

SAWs are elastic waves which propagate in solids with well-defined direction and velocity, being mainly confined around the surface [50]. In piezoelectric materials, the SAW propagates accompanied by a piezoelectric potential that interacts with charge carriers and modifies their diffusion and recombination dynamics. Thus, it is possible to modulate the physical properties of semiconductor nanostructures located on or near the surface using SAWs, and the integratability of SAW devices with planar systems holds promising perspectives for novel applications in photonics, optomechanics, and quantum information science [48, 51].

The dynamic mechanical deformation and piezoelectric potential of SAWs have been successfully employed to achieve acoustically-induced carrier transport. The works of Rocke [52, 53] in the late 90's led to several advances in the context of acoustic modulation and transport of elementary excitations in inorganic semiconductor media, such as spin packets [54, 55], excitons [56] and charge carriers [57]. SAWs have been also used to modulate the optical emission of single nanostructures [58–61], and to manipulate plasmon [62] and polariton [63] dynamics.

In general, quasi two-dimensional (2D) systems exhibit excellent coupling with SAWs due to their large relative surface area and reduced thickness [48]. Furthermore, in the presence of quantum confinement in the out-of-plane direction, SAWs become an efficient tool in the context of transport, as charge carriers can move in the surface plane. Moreover, the SAW beams can be routed directly to the sample over macroscopic distances with high accuracy and low loss [48, 51], which eliminates the need to establish direct electric contact with the sample. For this reason, most of the achievements of the SAW-driven modulation of semiconductor systems have been accomplished in micro and nano structures based in flat systems, such as quantum wells. SAWs have also been interfaced with 2D materials, especially graphene [64], but also BP [65, 66] and TMD MLs [36, 67–69]. The employment of SAWs to manipulate the optical properties of few-layered TMDs is a field of high scientific and technological interest due to the wide variety of applications in devices and basic research of the tunable electronic and optical properties of the TMDs.

1.3 Acoustic Modulation of TMDs

In TMD MLs, the first reported acoustic modulation experiments have been performed exclusively with MoS₂ at room temperature. Rezk and coworkers [70] applied SAWs on few-layered MoS₂ samples (2 to 4 layers) placed on LiNbO₃ substrates and observed a small suppression of the photoluminescence (PL) emission intensity at a relatively slow dynamics. The same group [67] presented a study of MoS₂ MLs placed over non-piezoelectric Sapphire, where the dielectric screening is reduced. The experiments relied solely on the ML piezoelectricity induced by the SAW mechanical deformation to change the carrier dynamics. A PL quenching followed by an energy blueshift of the excitonic emission band (comprised by neutral and negatively charged exciton emissions) with increasing acoustic power has been observed. The blueshift of the the broad excitonic emission band towards the neutral exciton transition has been attributed to a more efficient quenching of the trion PL as compared to neutral exciton due to the one order of magnitude larger

binding energy of the latter. Based on these results, Huang and coworkers [71] conducted a theoretical investigation of the progression of the charge carrier, exciton and trion populations on a MoS₂ ML under the influence of SAWs. Preciado and coworkers [36] fabricated and characterized a hybrid MoS₂/LiNbO₃ electro-acoustic device. They employed SAWs to manipulate and probe the transport properties of the device by means of photoconductivity measurements.

More recently, a work presented by Datta and coworkers [68] shows the investigation the Stark effect and exciton dissociation induced by SAWs in WSe₂ MLs placed over LiNbO₃ substrates at room temperature, which allowed the authors to determine the in-plane polarizability of neutral exciton in such conditions. The same group published a work during the process of finalizing this thesis, in which they demonstrate the SAW-driven exciton transport h-BN encapsulated WSe₂ MLs placed on LiNbO₃ substrate.

1.4 This Thesis

Chapter 2 provides a discussion of the fundamental physics of TMD MLs. We discuss general consequences of the dimensionality reduction (from bulk to ML) on the crystal and band structures. The exciton dynamics in MLs is presented in terms of the most relevant experimental and theoretical findings of the literature and we emphasize on the role of the dielectric screening on the main properties of the excitonic complexes. In this picture, we describe a classical model for the electron-hole interaction that extends beyond the widely employed Rytova-Keldysh formalism and contemplates the high dielectric screening provided by the LiNbO₃ substrate.

Chapter 3 brings the general description and the mathematical formalism of SAW propagation, especially on Y-128° LiNbO₃ surfaces. We also discuss the overall SAW-induced modulation mechanisms of the emission properties of semiconducting systems as a combination of the bandgap modulation associated with the mechanical deformation and a in-plane Stark effect induced by the piezoelectric field. The

fundamental exciton dissociation mechanism and the acoustically-induced carrier transport are also discussed. Under the light of exciton and SAW Physics in TMD systems, we conclude the chapter reviewing the most important literature results and achievements on the subject.

Chapter 4 presents the experimental methodology. We present the SAW generation mechanism, the description of the fabrication and characterization of SAW-generating devices. We show details of the devices used on the optical experiments as well as devices that we fabricated using optical photolithography. We also provide details of the sample fabrication and the experimental setup employed in the the modulation experiments.

Chapter 5 brings the details of the computational calculations of the SAW fields on the samples. We employ Finite Elements Method (FEM) calculations in order to obtain the SAW modes and the amplitude of both strain and piezoelectric potential on the samples from the input Radio-Frequency (RF) power applied on the device, which is a controllable parameter of our experiments. We show that the results of the simulation exhibit excellent agreement with the experimental RF reflection coefficient.

Chapter 6 brings the compilation of the experimental results of the optical spectroscopy experiments carried out on MoS₂ and MoSe₂ MLs in the presence of continuous propagating SAW beams. We discuss the main observed properties of the SAW-induced photoluminescence (PL) quenching and the observed temporal dynamics relying on the interplay between the excitonic radiative recombination and the SAW-induced dissociation. We also discuss the excitonic Stark effect and obtain the first measurement of the in-plane polarizabilities of neutral and negatively charged excitonic complexes for a non-encapsulated MoSe₂ sample. Our results agree with theoretical calculations for MoSe₂ and experimental results obtained for WSe₂ MLs.

Chapter 7 is a summary of the results and achievements of the work and a final discussion with the future perspectives.

CHAPTER 2

Two-Dimensional Transition Metal Dichalcogenides

This chapter is dedicated to the discussion of the physics of the semiconductor 2D TMDs from group VI. We begin by highlighting the main characteristics of the ML system and compare it to the bulk case in terms of crystal and electronic structures. Furthermore we discuss the band structure of the ML and the presence of bright and dark exciton features as well as the valley-selective selection rules for the optical transitions. The optical response and nonequilibrium dynamics of TMD ML systems is dominated by excitonic complexes [16]. Under certain conditions of dielectric environment the transition from bulk to ML leads to an enhanced electron-hole interaction, which provides a high excitonic binding energy that reaches up to hundreds meV, being more than one order of magnitude larger than in III-V heterostructures [72–75]. As a consequence of such a robust excitonic interaction, a rich many-body physics arises in TMD MLs. In this chapter, we bring an extensive description of three different models to describe the exciton interactions in TMD MLs and compare the validity of each one. We focus the discussion in the dielectric screening problem, which is not often considered but is essential to understand our experimental findings.

2.1 Crystal structure

TMDs are a class of more than 40 different materials [5, 7] which exhibits as main characteristics (i) a layered structure and (ii) a general chemical composition

on the form MX_2 , where M is a transition metal and X represents a chalcogen species. Figure 2.1 shows a periodic table of elements in which transition metals from the groups 4 to 7 are highlighted alongside with the chalcogens (shown in orange). Groups 9 and 10 are partially highlighted because only some of the dichalcogenides form layered structures [7].

MX_2 M = Transition metal X = Chalcogen																	
H																	He
Li	Be											B	C	N	O	F	Ne
Na	Mg	3	4	5	6	7	8	9	10	11	12	Al	Si	P	S	Cl	Ar
K	Ca	Sc	Ti	V	Cr	Mn	Fe	Co	Ni	Cu	Zn	Ga	Ge	As	Se	Br	Kr
Rb	Sr	Y	Zr	Nb	Mo	Tc	Ru	Rh	Pd	Ag	Cd	In	Sn	Sb	Te	I	Xe
Cs	Ba	La-Lu	Hf	Ta	W	Re	Os	Ir	Pt	Au	Hg	Tl	Pb	Bi	Po	At	Rn
Fr	Ra	Ac-Lr	Rf	Db	Sg	Bh	Hs	Mt	Ds	Rg	Cn	Uut	Fl	Uup	Lv	Uus	Uuo

Figure 2.1: Highlighted elements that form about 40 different known layered TMD compounds. Transition metals from groups 4 to 7 tend to form thermodynamically stable layered TMD. Extracted from [7]

In the bulk form, TMDs are comprised of stacked MX_2 MLs held together by van der Waals interaction. Each ML, on the other hand, is formed by an atomic layer of M atoms sandwiched between two layers of X atoms with a covalent M-X bonding, which is much stronger than the inter-layer van der Waals force. Figure 2.2.a shows an illustration of a multi-layered TMD system where M and X atoms are represented by red and black spheres, respectively. The weak interlayer coupling allows the manufacturing of few-layered systems with typical lateral extension of tens of micrometers using top-down routes like micro-mechanical cleavage (commonly referred as dry exfoliation, or just exfoliation) and liquid exfoliation. Layered systems, including MLs, also might be obtained using bottom-up routes such as molecular beam epitaxy (MBE), chemical vapour deposition (CVD), metal-organic chemical vapour deposition (MO-CVD), Van der Waals epitaxy, electrodeposition, and wet chemical processes [3, 5, 15, 76].

The typical crystal structure of TMDs are the trigonal prismatic (2H) or the octahedral (1T and 1T') atom coordination [6, 76], which correspond to different

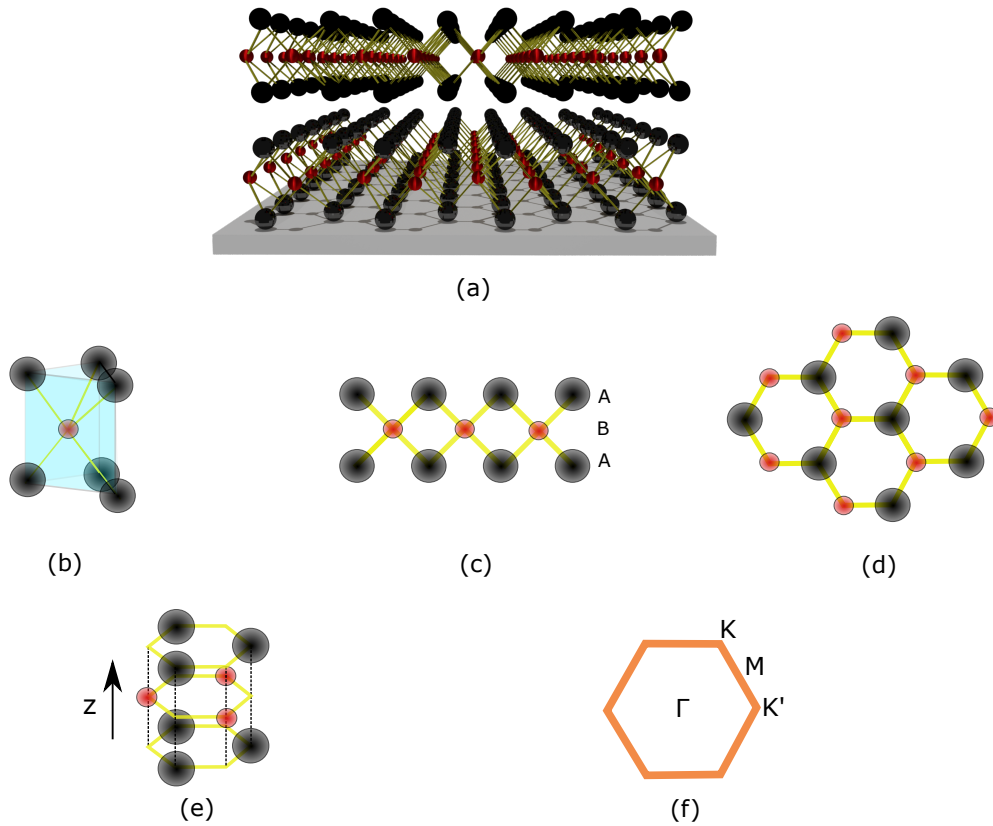


Figure 2.2: (a) Schematic representation of a typical MX_2 structure, with the chalcogen atoms (X) in black and the metal atoms (M) in red. The gray surface represents the substrate. Two MLs are represented to illustrate the stacking. The addition of more MLs forms the bulk. (b) Trigonal prismatic (2H) coordination. (c) Side view of lattice structure of 2D TMD in the 2H coordination. (d) Top view of the honeycomb lattice of 2D TMD in the trigonal prismatic coordination. (e) Atomic structure of a single layer of a TMD exhibiting the lack of spatial inversion symmetry. (f) First Brillouin zone of the TMD showing the main symmetry points Γ , M, K and K' .

stacking configurations of the atomic sheets within a single ML. In the 2H phase, chalcogen atoms from different layers are aligned in the direction perpendicular to the ML plane and occupy the same position A while the metal atom from the central sheet are in a different position B as represented in Figure 2.2.a. As a consequence, the atomic layers are stacked in an A-B-A order, as shown in Figure 2.2.c and the ML exhibits a honeycomb lattice as shown in Figure 2.2(d). On the other hand, in the octahedral phases, chalcogen atoms from different layers do not share the same position anymore, resulting in a A-B-C stack order (A and C

refer to the positions of chalcogen atoms of different layers). Particularly TMDs from the group VI (based on Mo and W) usually exhibit the 2H phase as the thermodynamically stable phase (except from WTe_2) although the 1T may also be obtained as a metastable phase [76].

When in ML form, the spatial inversion symmetry is broken [10] in the 2H structural phase, as shown in Figure 2.2(e). In other words, given the position \vec{r} of a single atom in the ML honeycomb lattice, the position $-\vec{r}$ does not always represent an equivalent position in the crystal structure. As a consequence, the TMD ML lattice lacks an inversion center and thus exhibits special properties such as piezoelectricity [67, 77, 78]. Systems with an even number of layers, on the other hand, exhibit spatial inversion symmetry and hence do not hold such properties [67].

The first Brillouin zone of the hexagonal lattice of the TMD ML in the 2H phase is also hexagonal as shown in Figure 2.2(f). Due to the lack of inversion symmetry, points K and K' are no longer equivalent despite being degenerated in energy and connected via time reversal symmetry. As a consequence, different optical selection rules arise for the optical transition involving those points.

2.2 Band structure

The various different combinations of transition metals and chalcogens give rise to many different stable TMD systems with very different characteristics. In terms of electronic properties, the TMD systems can be semiconductors, semimetals, true metals, and superconductors [15]. We are interested in TMDs from the group VI which are semiconductor systems [3, 5, 6, 15, 30] whose research interest usually concentrates upon the electronic and catalytic properties. Properties such as tunable bandgap and relatively high carrier mobility are responsible for the application in electronics, optoelectronics, and catalysts. Furthermore, these materials comprise an ideal platform to study solid-state physics due to robust excitonic effects, spin-orbit coupling, and many-body interactions [15]. The properties of the other TMD groups are discussed in detail in references [6], [15] and [76].

Figure 2.3 shows the progression of the band structure of semiconductor MoS₂ obtained via Density Functional Theory calculations [9] as a function of the number of layers. In the bulk form, MoS₂ exhibits an indirect optical transition between the Γ point of the valence band (VB) (Γ^V) and a point halfway Γ and K points on the conduction band (CB) (referred as Λ^C). As the sample is thinned down from bulk to ML, a progression from the indirect-gap transition to a direct-gap transition at the K (K^V and K^C) point is observed [8].

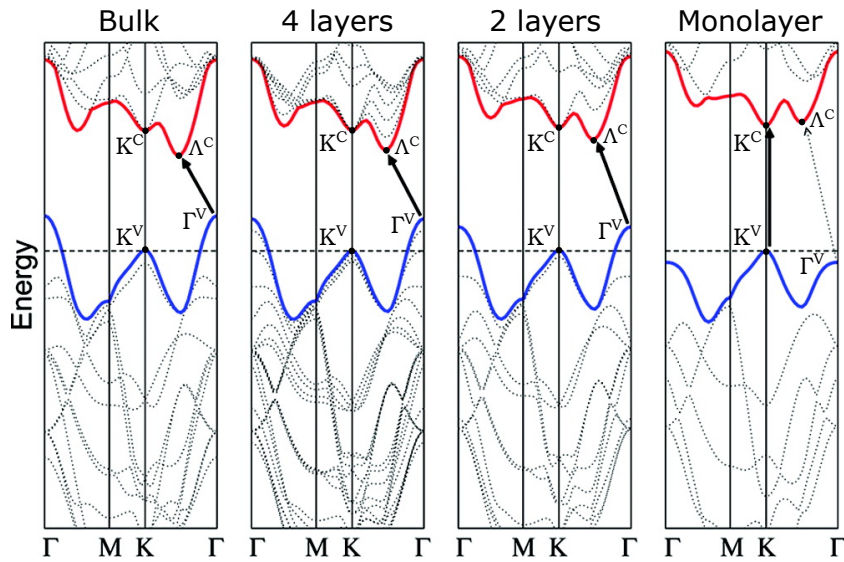


Figure 2.3: Evolution of the electronic band structure of semiconductor MoS₂ as the sample is thinned from bulk to ML, calculated using Density Functional Theory. As the number of layers is decreased, the indirect energy gap increases between points Γ^V and Λ^C . For the the ML limit, a direct energy gap is observed at the K point. Extracted and adapted from [9].

The change from an indirect bandgap semiconductor, in the case of two or more layers, to a direct bandgap in the case of the ML is understood in terms of the electronic states which compose both valence and conduction band edges [11, 79, 80]. The electronic states at the center of the Brillouin Zone (Γ point) are mainly composed of p_z and d_{z^2} orbitals from the chalcogen and metal atoms respectively, exhibiting a substantial projection out of the atomic plane and are related to the interlayer interaction. As a consequence, a substantial spatial overlap between the electronic orbitals from adjacent MLs (i.e. in the out-of-plane direction) which

increases the oscillator strength of the $\Gamma^V - \Lambda^C$ optical transition and establishes an indirect bandgap on the bulk case. The electronic states around the corners of the Brillouin Zone (K and K' points), on the other hand, are mainly confined to the atomic planes due to a strong contribution of $d_{x^2-y^2} + id_{xy}$ orbitals of the transition metal to the VB and a combination of p_{z^2} and $p_x \pm ip_y$ respectively from the metal and the chalcogen to the CB. At the K point, an energy minimum is observed in the CB and a maximum in the VB. The removal of layers from the bulk diminishes the out-of-plane direction orbital overlap, which increases the indirect bandgap between Γ^V and Λ^C while the direct energy gap at the K point is nearly unaffected, as shown in Figure 2.3. In the the ML, the band extrema are located at the K and K' points of the Brillouin Zone, allowing a crossover to a direct optical transition in the visible and near infra-red spectral regions. The shift of the VB minima from the Γ to K point as a consequence of a suppression of inter-layer interaction has also been experimentally investigated via angular-resolved photoelectron spectroscopy (ARPES) [81]. The direct band gap and the strong excitonic effects (discussed below) allow efficient light emission even at room temperature, in contrast to bulk and few-layered systems [8, 9].

Besides the presence of a direct bandgap transition with high emission efficiency, the combination of crystal symmetry and electronic orbital configuration give raise to spin and valley-selective phenomena, as well as spin-valley coupling. Figure 2.4 shows a general representation of the band structure of a MoX_2 TMD ML at the K and K' valleys of the hexagonal Brillouin Zone, which is also represented. The term valley is used to designate the symmetry points of the Brillouin Zone, such as K, Γ and M and labels the \vec{k} momentum index [5]. The direct bandgap with an amplitude of E_{GAP} is represented at the K and K' points of the Brillouin zone. Both conduction and valence bands exhibit two splitted sub-bands with opposite spin orientations due to a strong spin-orbit coupling, as discussed below. The spin up and down sub-bands are represented in blue and red, respectively. E_{GAP} is defined as the energy separation between the uppermost VB and lowermost CB states.

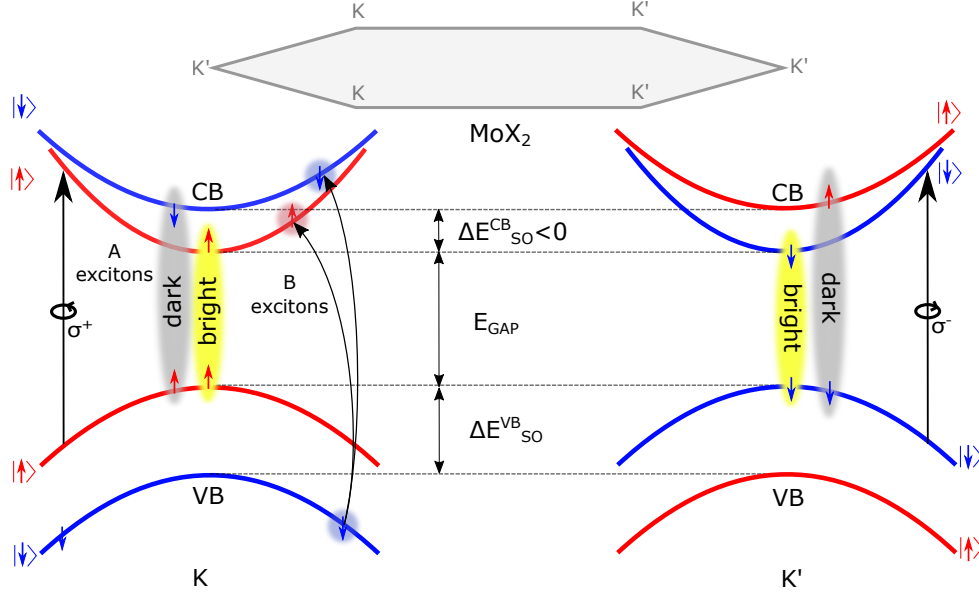


Figure 2.4: General electronic band structure of the MoX_2 TMD ML systems. Non-equivalent K (left) and K' (right) valleys of the Brillouin zone (represented on the top) are locked to opposite spin states due to time-reversal symmetry. The subsequent optical selection rules for the A excitons allow selective excitation of K (K') valley through σ^+ (σ^-) excitation and the ground state is optically active (bright) for MoX_2 . The B excitons are also represented for the K valley.

Due to the lack of a crystal inversion symmetry center, the spin states at K and K' valleys of the TMD ML are connected via $E^\uparrow(k) \neq E^\uparrow(-k)$ (relative to the Γ point of the Brillouin Zone), where $E^\uparrow(k)$ and $E^\downarrow(k)$ are the energy dispersion of spin up and spin down states, respectively. On the other hand, time inversion symmetry imposes that $E^\uparrow(k) = E^\downarrow(-k)$ and, as a consequence, $E^\uparrow(k) \neq E^\downarrow(k)$ so that the spin degeneracies of valence and conduction bands are broken at the K points [79]. Besides the lack of inversion symmetry, the spin-orbit coupling (SO) is stronger in TMD MLs than in other 2D systems, such as graphene, due to the presence of heavy elements and the prominent contribution of d orbitals to the electronic states. Such a high SO interaction increases the energy splitting between the opposite spin states [5, 79]. In the VB, a spin-splitting ΔE_{SO}^{VB} of hundreds of meV is established while a lower spin-splitting ΔE_{SO}^{CB} of tenths of meV is observed on the CB due to p orbital compensation, as represented in Figure 2.4.

As a consequence of the large SO-induced spin-splitting in the VB there are two sub-bands which are very well separated referred as A and B bands [8] as represented on the K valley in Figure 2.4. When excitons associated to the A and B bands are formed at the K (K') points, they are referred to as A and B intralayer excitons, respectively. The spin-splitting on the CB, although smaller, is responsible for the presence of an optically inactive spin-forbidden (dark) and an optically active spin-allowed (bright) A exciton configurations as represented respectively by the gray and yellow balloons in Figure 2.4. Dark and bright B excitons also arise from the spin-splitting of the VB, but are not represented in Figure 2.4. Also, ΔE_{SO}^{CB} has opposite signs for Mo and W based TMDs [80], which implies in a bright ground state for Mo-based systems and a dark ground state for the W-based systems [5]. Table 2.1 [17] shows the discussed parameters of the main TMDs of the group VI when in the ML form.

Table 2.1: Values of E_{GAP} , ΔE_{SO}^{CB} , ΔE_{SO}^{VB} and the neutral exciton binding energy $E_B^{X^0}$ of the main TMDs of the group VI in the ML form. Values were extracted from Ref. [17].

Property	Symbol	MoS ₂	MoSe ₂	WS ₂	WSe ₂
Electronic bandgap	E_{GAP} (eV)	2.5	2.2	2.7	2.1
CB SO energy splitting	ΔE_{SO}^{CB} (meV)	-3	-21	29	36
VB SO energy splitting	ΔE_{SO}^{VB} (meV)	160	180	380	430
Neutral exciton binding energy ¹	$E_B^{X^0}$ (meV)	600	600	700	500

The adjacent corners of the Brillouin Zone (K and K') are degenerated in the absence of a external magnetic field [5]. On the other hand, the spin states at the valleys K and K' are connected via time reversal symmetry, thus exhibiting opposite orientations as shown in Figure 2.4. This fact implicates in a coupling of spin and valley degrees of freedom, giving raise to valley-selective chiral selection rules for the optical interband transition where the K (K') valley is excited through

¹Under weak dielectric screening conditions, which is mainly achieved in substrates with low dielectric constant as SiO₂.

σ^+ (σ^-) circularly polarized light [11], as indicated in Figure 2.4. The optically-generated electron-hole pairs are valley and spin polarized and the exciton emission is copolarized with the laser. Since the intervalley scattering ($K \rightarrow K'$) can be energetically unfavorable [82] and spin-flip can be suppressed [79].

The spin polarization can be evaluated in polarization-resolved photoluminescence (PL) experiments by means of the degree of polarization ρ^{POL} :

$$\rho^{POL} = \frac{I(\sigma^+) - I(\sigma^-)}{I(\sigma^+) + I(\sigma^-)}, \quad (2.1)$$

where $I(\sigma^+)$ ($I(\sigma^-)$) is the measured intensity of the σ^+ (σ^-) component of the PL. In TMD MLs ρ^{POL} can reach high values as 90% [83] and even 100% [10] under resonant excitation. In this picture, the generation, detection, and manipulation of spin-valley polarized states puts the TMD ML systems as a robust platform for investigation in the context of valleytronics and spin dynamics [10, 11, 82, 84–86].

2.3 Exciton dynamics

The photoexcitation of a valence electron to the CB leaves an unoccupied state in the VB. The system composed of an excited electron and the vacancy can be described as a negatively charged conduction electron interacting with a positively charged valence hole in a two-particle picture. This electron-hole pair behaves similarly to a hydrogen atom and is called exciton. Excitons (X^0) are electrically neutral entities, but can eventually capture an additional electron or hole to become a negatively charged exciton (X^-) or a positively charge one (X^+), both usually referred to as trions. The X^- and the X^0 are illustrated in Figure 2.5.a. In general, such excitonic complexes are strongly bonded due to the quantum confinement and an unscreened Coulomb potential associated to the surrounding media. [72].

Figure 2.5.b depicts the energy diagram of the X^0 and X^- states within the material bandgap. In the ground state ($n=1$), X^0 can decay and emit a photon with energy E_{X^0} , which is commonly observed in PL experiments. The exciton binding

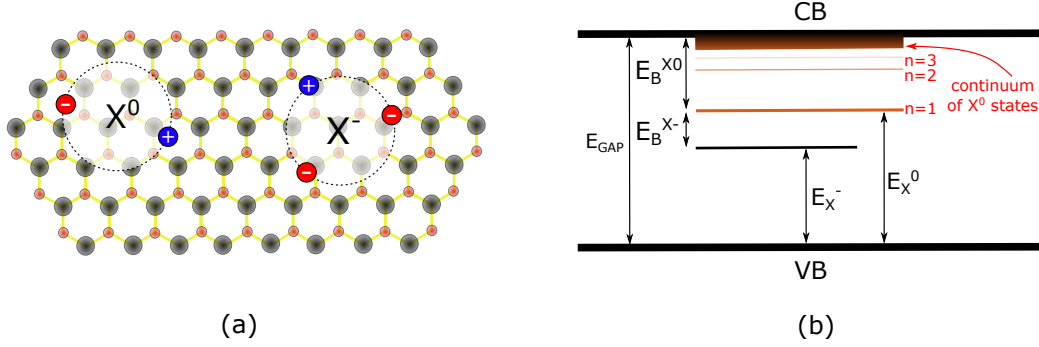


Figure 2.5: (a) Representation of the X^0 and the X^- quasi-particles on the TMD structure. Red and blue circles represent the electrons and holes, respectively. (b) Energy diagram showing the X^0 ground ($n=1$) and excited ($n=2, 3\dots$ and the continuum) states and the X^- ground state. The X^0 binding energy $E_B^{X^0}$ is the difference between E_{GAP} and the exciton energy E_{X^0} . The trion energy level lies below the X^0 ground state with an energy separation of $E_B^{X^-}$, the trion binding energy. The excited states of the X^- are not represented. E_{X^0} and E_{X^-} are commonly observed in PL experiments.

energy $E_B^{X^0}$ is the amount of energy needed to dissociate the electron-hole pair and determines the exciton energy E_{X^0} as $E_{X^0} = E_{GAP} - E_B^{X^0}$.

The trion complexes also exhibit a binding energy $E_B^{X^-}$, which is related to the energy needed to dissociate the quasi-particle into a neutral exciton and a free carrier (the trion binding energy is sometimes referred to as the trion dissociation energy). The X^- ground state can emit a photon with energy E_{X^-} , which can also be observed in PL experiments. As an approximation, the emission energies of X^- and X^0 are separated by $E_B^{X^-}$ so that $E_{X^-} + E_B^{X^-} = E_{X^0}$.

In the next sections, we present three different approaches for the description of the excitonic interaction in TMD MLs and discuss the fundamental physics of each one as well as the validity of each model.

2.3.1 Hydrogen model approximation

Three-dimensional exciton

Figure 2.6.a represents the side view of a three-dimensional Wannier exciton in a bulk TMD system. In such case, the free 3D exciton is bonded via Coulomb

interaction and it can be treated in a similar way to a hydrogen atom, thus exhibiting a binding energy given by [87]:

$$E_B^{3D}(n) = -\frac{\mu R_H}{m_0 \varepsilon^2 n^2} = -\frac{R_X}{n^2}, \quad (2.2)$$

where $\mu = \frac{m_e + m_h}{m_e m_h}$ is the exciton reduced mass, m_e and m_h are the electron and hole effective masses, respectively, given in terms of the electron rest mass m_0 . The constant $R_H = -13.6\text{eV}$ is the hydrogen Rydberg constant, ε is the dielectric constant of the material and n is the principal quantum number which labels the excitonic state. The constant $R_X = (\mu/m_0 \varepsilon^2) R_H$ is the exciton Rydberg constant.

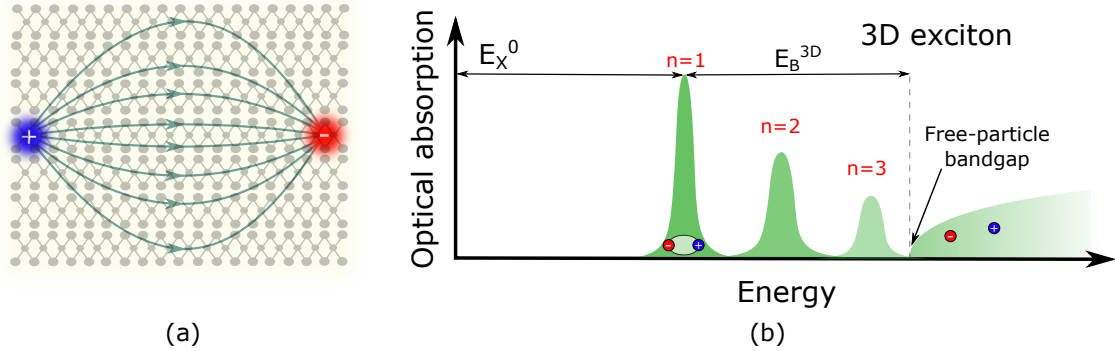


Figure 2.6: (a) Real-space representation of a 3D exciton in a bulk system, where field lines are screened inside the material. (b) Typical absorption spectrum of a 3D system, with the $1/n^2$ hydrogenic series of the exciton states.

As shown in Figure 2.6.a the 3D exciton field lines can extend over several layers of the bulk TMD and are fully immersed within the material media. The interaction potential depends on the dielectric constant of the material as depicted in Equation 2.2. As a consequence, the exciton energy levels scale with R_X in contrast to a free hydrogen atom in vacuum. E_B^{3D} goes down to tenths of meV for most III-V and II-VI semiconductors such as GaAs (4.2 meV), GaN (23 meV) and ZnSe (20 meV) [87]. These values are comparable to $k_B T$ at room temperature ($\sim 25\text{meV}$) [87]. As a consequence, the excitonic effects are generally investigated at cryogenic temperatures where the exciton complexes remain stable.

Figure 2.6.b shows a schematic of the optical absorption spectrum of a 3D neutral exciton with the ground state ($n=1$), and the excited states below the free-

particle bandgap as well as the representation of E_{X^0} and $E_B^{X^0}$. Above the free-particle bandgap, the free charge carriers obey a $E^{1/2}$ dispersion as a consequence of the density of states in the absence of confinement [87]. The X^0 states follow the Rydberg series based on the $1/n^2$ progression which is the hydrogen-like progression of the Wannier-Mott excitons [72,87]. The effective exciton radius is given by:

$$a_X^{3D} = \frac{n^2 m_0 \varepsilon}{\mu} a_H, \quad (2.3)$$

where $a_H = 5.19 \times 10^{-11} \text{m}$ [87] is the Bohr radius of the hydrogen atom. As a_X^{3D} increases with n , the overlap between electron and hole wave functions is decreased and the main consequence is the reduction of the intensity of the optical transitions (absorption or emission) between energy levels. This effect can be understood in terms of the matrix elements of each individual transitions and is called oscillator strength (f_n). The oscillator strength of 3D free Wannier excitons exhibits a dependence $f_n \propto n^{-3}$ on the principal quantum number [88]. Figure 2.6.b also illustrates this behavior with the decreasing trend on the optical absorption intensity below the free-particle bandgap.

Two-dimensional exciton

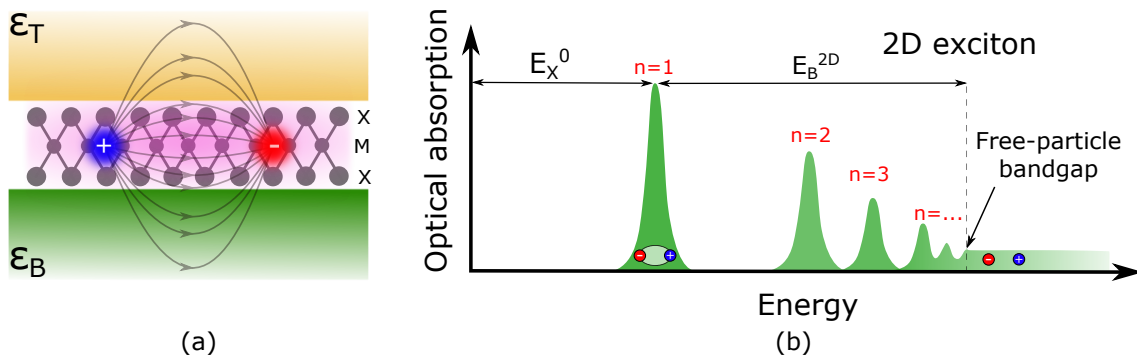


Figure 2.7: (a) Side view of a TMD ML with the representation of a 2D exciton. The ML is sandwiched between two materials with dielectric constants ε_B (bottom) and ε_T (top) which are permeated by the electric field of the X^0 . (b) Representation of a typical absorption spectrum of a 2D system with excitonic interaction.

Figure 2.7.a shows a representation of the cross section of a system composed

by a TMD ML sandwiched by a substrate (green) and a top material (yellow). In ideal quasi-2D systems, such as quantum wells and TMD MLs, the reduction of dimensionality confines the electron-hole pair motion into the 2D plane. However, the electrostatic interaction is not fully confined and part of the field lines leak outside of the 2D system permeating the adjacent material media. In this situation, the Coulomb potential is usually approximated by [72]:

$$V_{e-h}^{2D}(r) = -\frac{e^2}{4\pi\bar{\epsilon}r}, \quad (2.4)$$

where $\bar{\epsilon} = (\epsilon_B + \epsilon_T)/2$ is the average dielectric constant of the surrounding media. Although simplified, the use of $\bar{\epsilon}$ is widely employed in the description of the 2D excitons in several different TMD models [5, 72, 89]. The binding energy of a 2D exciton predicted by the 2D hydrogen approximation is consequently given by [72]:

$$E_B^{2D}(n) = \frac{\mu R_H}{m_0\bar{\epsilon}^2(n - \frac{1}{2})^2}, \quad (2.5)$$

which follows a $1/(n - \frac{1}{2})^2$ hydrogenic series instead of the $1/n^2$ progression of the 3D exciton [88, 90, 91]. The hydrogen approximation yields $E_B^{2D} = 4E_B^{3D}$ for the neutral exciton ground state ($n=1$). Therefore, with an increase in the binding energy (and electron-hole wave function overlap) in comparison to the 3D case. A more efficient light emission is, therefore, expected for 2D systems.

Figure 2.7.b illustrates the optical absorption spectrum of the 2D exciton as predicted by the 2D hydrogen approximation where the X^0 states are indicated below the free-particle bandgap as well as the X^0 binding and transition energies. Now the free charge carriers (above the bandgap) are subjected to a quantized step function dispersion associated to the 2D density of states [87]. The effects of quantization also extends for the oscillator strength of the n -th state as $f_n \propto (n - 1/2)^{-3}$ [5, 88], which is depicted by the decrease trend in intensity of the optical absorption strength.

Reflection spectroscopy experiments on WS_2 MLs [72] have shown a deviation from the excitonic series predicted by equation 2.5, which is mainly attributed to the non-homogeneous screening of the electric field. The $1/r$ dependence of the

interaction potential is shown to stand for large inter-particle distances when most of the field lines run outside of the ML. However, for short inter-particle distances, most of the field lines lie within the ML so that the dielectric screening is strongly reduced. This explains why the experimental results show a considerable deviation from the hydrogen approximation for the ground ($n=1$) and the first excited state ($n=2$) energies while the higher order states follow the 2D Hydrogen-like model.

2.3.2 Rytova-Keldysh model

A classical approach for the problem of a point charge within a thin film was proposed in the works of Rytova [92] and Keldysh [93] and led to the so-called Rytova-Keldysh (RK) form of the screened potential. The electron-hole electrostatic interaction predicted by the Rytova-Keldysh model applied to a single TMD ML with thickness d and dielectric constant ε_{TMD} sandwiched between semi-infinite bottom and top materials with dielectric constants ε_B and ε_T respectively is given by [5, 72, 94]:

$$V_{e-h}^{RK}(r) = \frac{e^2}{2\pi\varepsilon_0(\varepsilon_B + \varepsilon_T)r_0} \left\{ H_0\left(\frac{r}{r_0}\right) - Y_0\left(\frac{r}{r_0}\right) \right\}, \quad (2.6)$$

where $r_0 = \varepsilon_{TMD} \frac{d}{(\varepsilon_B + \varepsilon_T)}$ is screening length, which is related to the polarizability of the ML, H_0 and Y_0 are the zero order Struve and Neumann functions [95], respectively and $\varepsilon_0 = 8.854 \times 10^{-12}$ F/m [87] is the electric permittivity of the free space.

While applied to the problem of excitons in TMD MLs, the RK model provides the series of the excitonic resonances by means of numerical, variational, or analytical solutions of the exciton wave equation with the potential $V_{e-h}^{RK}(r)$, via Wannier-Mott theory. The achieved results exhibit excellent agreement with most of the experiments [5], including the binding energies of $n=1$ and $n=2$ states which could not be well described by the 2D Hydrogen model [72, 96]. It also agrees with more sophisticated *ab initio* calculations which go beyond the Mott-Wannier model, such as the many-body physics formalism of the Bethe-Salpeter equation [97, 98]. As

a consequence, we have to remember that the RK model is the most employed description for the exciton physics of TMD MLs.

Nevertheless, $V_{e-h}^{RK}(r)$ is obtained under the assumptions of (i) weak dielectric screening, i.e. a low dielectric constants of bottom and top media in comparison to the thin film (TMD), and (ii) much smaller film (TMD) thickness in comparison to the exciton radius (a_X^{2D}), such that:

$$\begin{cases} \text{(I)} & \varepsilon_B, \varepsilon_T \ll \varepsilon_{TMD} \\ \text{(II)} & d \ll a_X^{2D}. \end{cases} \quad (2.7)$$

In most experimental situations reported in the literature, the approximations given by Equations 2.7 are valid, as confirmed by the agreement between the predictions of the RK model and the measured values of $E_B^{X^0}$ [5]. In fact, the most common configuration of the experiments consists of a TMD ML placed on the top of substrates such as SiO_2 or h-BN that exhibit dielectric constants of approximately $4\varepsilon_0$ [94, 99] while the top material is usually air or vacuum ($\varepsilon_T \approx 1\varepsilon_0$). Considering that the dielectric constant of the group VI TMDs is of the order of $15\varepsilon_0$ [94], the condition of weak dielectric screening is obeyed and the RK model stands in such cases.

However, the RK model does not recover the experimental results obtained in the strong dielectric screening regime [94, 100]. In this situation, where the dielectric constants of the surrounding materials are comparable to or exceed ε_{TMD} , the RK potential is expected to underestimate $E_B^{X^0}$ [94]. The RK model predicts it to be smaller than the measured $E_B^{X^-}$ [69, 100], as shown in the results of this thesis. The last statement is not possible since the addition of a charge carrier (negative or positive) to the neutral exciton, creating a trion, is expected to partially screen the electron-hole interaction potential due to an extra repulsive interaction between particles with equal electric charges.

2.3.3 Full-interaction potential

The theoretical investigation of the effective electron-hole interaction potential in systems with reduced dimensionality (as in the case of a TMD ML) is divided into classical and quantum approaches [94]. The classical solutions such as the ones found by Rytova [92] and Keldysh [93] are mainly based on the solution of the Poisson equation for an arbitrary number of stacked dielectric slabs. On the hand the quantum approach, such as the quantum electrostatic heterostructure (QEH) model [101], is based on first-principles and uses *ab initio* calculations of an effective dispersion of the dielectric constant.

A recent approach has been proposed by Cavalcante and coworkers [94] to investigate the role of the dielectric screening in the electron-hole interaction in van der Waals heterostructures by means of classical eletrodynamics. The method known as electrostatic transfer matrix (ETM) is based on the numerical solution of the Poisson equation for N dielectric slabs stacked along the z direction, each one with dielectric constant ε_n . Taking the c-th slab as the origin, the electric potential at the n-th slab $\phi_{n,c}$ satisfies the Poisson equation as:

$$\varepsilon_n^{\parallel} \nabla_{r,\theta}^2 \phi_{n,c} + \varepsilon_n^{\perp} \frac{\partial^2 \phi_{n,c}}{\partial z^2} = q \delta_{n,c} \delta(r), \quad (2.8)$$

where $\varepsilon_n^{\parallel}$ and ε_n^{\perp} are the in-plane and the out-of-plane components of the dielectric function of the n-th layer, $\nabla_{r,\theta}^2$ is the Laplacian operator in polar coordinates, and q is the electric charge of the particle at the c-th slab. The solutions for $\phi_{n,c}$ are in the form [94]:

$$\phi_{n,c}(r, z) = \frac{e}{4\pi\varepsilon_0\varepsilon_c} \int_0^{\infty} J_0(kr) \{A_n(k)e^{kz} + B_n(k)e^{-kz} + e^{k|z|} \delta_{n,c}\} dk, \quad (2.9)$$

where $J_0(kr)$ the zero order Bessel function and the constants, A_n and B_n , are determined by the boundary conditions of the problem. Since $V_{e-h}^{n,c} = e\phi_{n,c}$, the electrostatic potential at the n-th slab due to the charge at the c-th slab is written

as:

$$V_{e-h}^{n,c}(r) = \frac{e^2}{4\pi\epsilon_0} \int_0^\infty \frac{J_0(kr)}{\epsilon_{eff}(k)} dk, \quad (2.10)$$

where:

$$\epsilon_{eff}(k) = \frac{\epsilon_c}{A_n(k)e^{kz} + B_n(k)e^{-kz} + e^{k|z|}}, \quad (2.11)$$

gives the momentum dispersion of the effective dielectric constant. By imposing the continuity of $\phi_{e-h}^{n,c}(r, z)$ and $(\partial/\partial z)\phi_{e-h}^{n,c}(r, z)$ at the interfaces of adjacent slabs, one is led to a matrix equation whose solution determines the constants A_n and B_n and finally the dispersion of $\epsilon_{eff}(k)$, which is the main input for Equation 2.10.

Equations 2.11 and 2.10 are derived from a generalized treatment of a situation of an arbitrary number of N slabs. In particular, the $N=3$ case can be used to describe a system comprised of bottom + ML + top material, which we label as slabs 1, 2, and 3, respectively. In this situation, the ETM method returns an effective dielectric function given by [94]:

$$\epsilon_{eff}(k) = \frac{\epsilon_1 + \epsilon_3 + (1 + \frac{\epsilon_1\epsilon_3}{\epsilon_2})\epsilon_2 \tanh(kd)}{(1 + \frac{\epsilon_1\epsilon_3}{\epsilon_2}) + (1 - \frac{\epsilon_1\epsilon_3}{\epsilon_2}) \operatorname{sech}(kd) + \tanh(kd)}, \quad (2.12)$$

which is used in the Mott-Wannier theory via Equation 2.10, yielding the series of the exciton states and energies.

The general dielectric function $\epsilon_{eff}(k)$ given by Equation 2.12 is exact, i.e. does not require any approximation. However, in the limit of small thickness ($kd \rightarrow 0$) and weak dielectric screening ($\epsilon_{1,3}/\epsilon_2 \rightarrow 0$) which are the approximations used to derive the RK model (Equation 2.7), $\epsilon_{eff}(k)$ reduces to [94]:

$$\epsilon^{R-K}(k) = \frac{\epsilon_1 + \epsilon_3}{2} \left(1 + \frac{d\epsilon_2}{\epsilon_1 + \epsilon_3} k\right), \quad (2.13)$$

which, in turn, recovers $V_{e-h}^{RK}(r)$ from Equation 2.6 when applied to Equation 2.10 with the correspondence of $\epsilon_1 \rightarrow \epsilon_B$, $\epsilon_2 \rightarrow \epsilon_{TMD}$, and $\epsilon_3 \rightarrow \epsilon_T$ and considering the limit of $kd \rightarrow 0$, as follows:

$$V_{e-h}^{RK}(r) = \frac{e^2}{4\pi\epsilon_0} \int_0^\infty \frac{J_0(kr)}{\frac{\epsilon_B + \epsilon_T}{2} \left(1 + \frac{d\epsilon_{TMD}}{\epsilon_B + \epsilon_T} k\right)} dk \quad (2.14)$$

$$\equiv \frac{e^2}{2\pi\epsilon_0(\epsilon_B + \epsilon_T)r_0} \left\{ H_0\left(\frac{r}{r_0}\right) - Y_0\left(\frac{r}{r_0}\right) \right\}, \quad (2.15)$$

thus the RK model can be understood as a low k limit of the general problem. For this reason, we refer to the interaction potential obtained from Equation 2.12 as the full interaction potential.

The results obtained with the ETM method exhibit an excellent agreement with results achieved using the QEH model for the case of direct excitons, especially for the X^0 ground state [94] despite the contrast of complexity and computational cost between these two approaches. This makes the ETM particularly interesting for the calculation of $E_B^{X^0}$ in the case of a single TMD ML, particularly at the strong dielectric regime.

Figure 2.8 shows $E_B^{X^0}$ as a function of the substrate dielectric constant ϵ_B given in terms of ϵ_0 for the case of a MoSe₂ ML (used in our experiments), considering the top material as air ($\epsilon_T = 1$). $E_B^{X^0}$ is calculated using the three discussed models: (i) 2D Hydrogen model (red) given by Equation 2.5; (ii) the RK potential (blue), given by Equation 2.6 and (iii) the full interaction potential (green) [94] given by Equation 2.10 with the effective dielectric constant given by Equation 2.12. The calculations were carried out by Prof. Andrey Chaves (Departamento de Física - Universidade Federal do Ceará).

Figure 2.8 shows that the widely employed RK model and the full potential converge to a similar behavior in the limit of small values of ϵ_B , which is reasonable since the RK model is the limit of weak dielectric screening of the full potential. As an example of the weak dielectric screening, the orange vertical dotted line indicates the h-BN substrate where the RK and full potential models predict binding energies of the same order and compatible with the values found in Table 2.1. For low dielectric constants, the 2D Hydrogen models predicts much larger binding energies. On the other hand, the 2D Hydrogen and the RK models agree at high ϵ_B because a

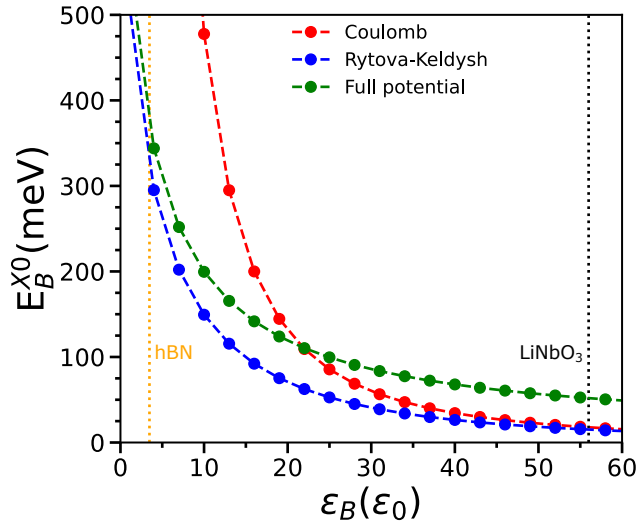


Figure 2.8: Neutral exciton binding energy (E_B^{X0}) as a function of the substrate dielectric constant ϵ_B calculated using the 2D Hydrogen model (red), the Rytova-Keldysh approximation (blue), and the full interaction potential [94] (green). The dielectric constants of LiNbO₃ (≈ 56) and h-BN (≈ 4) are indicated by the vertical lines. The calculations were carried out by Andrey Chaves (Departamento de Física - Universidade Federal do Ceará).

extremely strong dielectric screening is predicted. However, both Hydrogen and RK models underestimate E_B^{X0} when compared to the full potential in the high dielectric constant limit. The black vertical dotted line indicates the dielectric constant of LiNbO₃ (≈ 56 [50]) which was used in our experiments (presented in Chapter 6) and is a representative substrate of a situation of strong dielectric screening [68, 100]. In this situation the full potential predicts $E_B^{X0} = 52\text{meV}$ which is larger than the values predicted by the other models. Therefore, the different models predict different exciton properties because of their distinct dependence on the dielectric environment, affecting parameters like binding energy, free-particle bandgap and oscillator strength. The choice of substrate as well as encapsulation with h-BN show the impact of the dielectric environment on the excitonic effects of such systems [5, 16, 18, 102, 103]. In this way, it is very important to assess each experimental condition in order to evaluate the validity of each theoretical model.

Finally, the electron-hole interaction potential also affects the repulsive interaction between equal electric charges, which gives rise to a self energy contribution

to the overall excitonic states thus increasing the free-particle bandgap [5]. However, the self energy is usually similar to the binding energy and both contributions cancel each other out. Therefore, the exciton and trion energies (E_{X^0} and E_{X^-} of the Figure 2.5) remain nearly unaffected due to bandgap renormalization with only small blueshifts being detected at high dielectric constants [18, 36, 69, 100].

2.3.4 Trion binding energy

The negatively charged exciton binding energy is reported to exhibit a very weak dependence on the dielectric environment [103]. Table 2.2 shows measured and calculated values of $E_B^{X^-}$ for MoSe₂ MLs in different environments, namely: SiO₂ substrate; suspended in air; encapsulated in h-BN; and LiNbO₃ substrate. All the calculated values were extracted from the Ref. [103]. The values reflect no explicit dependence of $E_B^{X^-}$ with the dielectric environment.

Table 2.2: Measured and calculated values of $E_B^{X^-}$ for MoSe₂ ML. The calculated values were extracted from Ref. [103].

Substrate	$E_B^{X^-}$ (mev)	
	Measured	Calculated
SiO ₂	30 [104], 31 [105]	36.5
Suspended in air	-	42.2
h-BN encapsulated	26 [106], 30 [107]	26.2
LiNbO ₃	35 [69, 100]	-

A phenomenological model [103] has been proposed by Van Tuan and coworkers to explain the weak dependence of the trion binding energy on the dielectric constants of the materials above and below the ML. This phenomenological model is based on the RK model for the exciton.

The model considers the TMD ML system as a stack of three polarizable atomic sheets with different electric susceptibilities (χ_1 for the chalcogen atomic sheets and χ_2 for the central transition metal sheet) which constitutes a non-uniform screening profile, as shown in Figure 2.9. The X^0 and X^- quasi-particles are represented together with the field lines between the charge carriers. According to the calculations

of the authors [103], the chalcogen sheets confine the X^- field lines inside the ML, reducing the trion binding energy dependence on the bottom and top materials. On the other hand, the electric field of X^0 penetrates in the surrounding materials more efficiently thus making $E_B^{X^0}$ more sensitive to the dielectric environment.

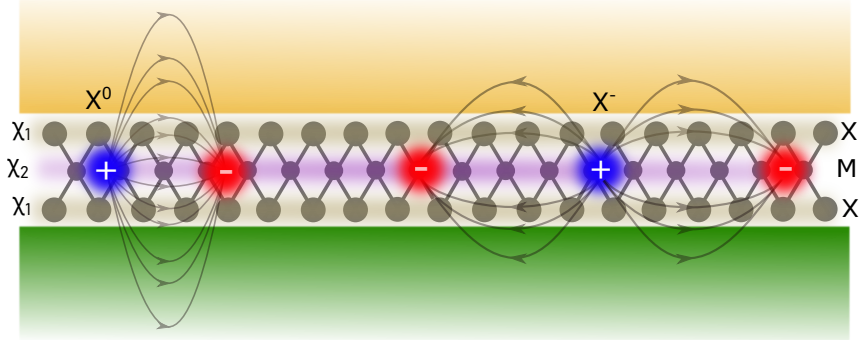


Figure 2.9: Side view of a TMD ML with the representation of a 2D exciton. The dielectric environment is not uniform within the ML, since each atomic sheet exhibits a different electric susceptibilities χ_1 and χ_2 . The screening from the chalcogen sheets helps to confine the field lines of the trion within the ML, reducing the dependence on the surrounding materials. On the other hand, the neutral exciton field lines leak outside the ML and a more pronounced dependence is observed on the top and bottom materials.

Physically, the model relies on a trion-lattice coupling induced by the extra electrical charge which leads to a large polaron (charge-phonon coupling) radius that results in a increase of the trion effective mass and consequently the trion binding energy as well. The neutral exciton, on the other hand presents a lower coupling to the lattice due to the zero total electric charge.

2.3.5 Exciton radiative lifetime

In general, the dynamics of excitonic complexes is governed by the processes of generation, relaxation and decay as illustrated in Figure 2.10. Under non-resonant excitation, the exciton owns a finite center-of-mass momentum K_{exc} [5, 105] and undergoes a phonon-assisted thermalization process (cyan arrows) in order to relax to the ground state (with a small K_{exc}), eventually decaying radiatively (purple arrow) with the emission of a photon with energy E_{X^0} . Besides the radiative decay, excitons are also subject to decay through non-radiative recombination channels,

which are attributed to the presence of impurities, point defects, Auger-type exciton-exciton annihilation [5]. Also, at finite temperatures, optically active excitons can be re-scattered (cyan arrows) away from the light cone, broadening the distribution around K_{exc} , which increases the radiative lifetime. The optical activity of excitons is subjected to energy and momentum conservation in such a way that excitons are only able to couple directly to light, i.e. be created or decay radiatively, when K_{exc} is smaller than the in-plane component of the light wave-vector k_0 [5], which arises even under normal incidence due to the use of the objective lens. This condition is represented in Figure 2.10 by the orange shaded cone, also known as the light cone, which is a region of the k -space defined by $K_{exc} < ck_0$, being c the speed of light.

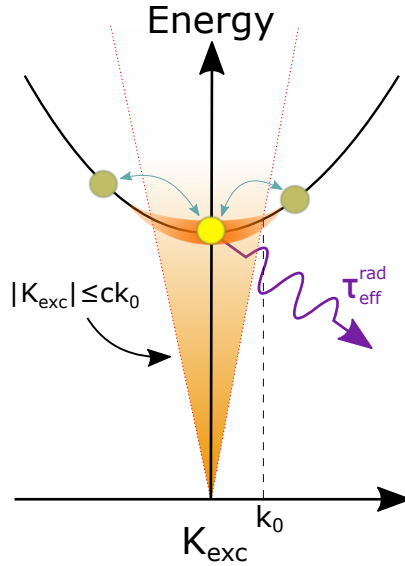


Figure 2.10: Exciton dynamics in a single-particle picture. Excitons are formed with a finite center-of-mass momentum K_{exc} . Through phonon scattering, excitons relax (cyan arrows) into the light cone, which is marked by the free-space photon dispersion ck_0 , and decay radiatively (purple arrow) with a lifetime τ_{eff}^{rad} . However, at finite temperatures, optically active excitons can be re-scattered (cyan arrows) away from the light cone, causing the thermal population to extend beyond the light cone edge k_0 and increasing the radiative lifetime as a consequence. Adapted from [5]

The radiative decay rate Γ_{rad}^0 is generally related to the probability of finding both electron and hole within the same unit cell as [5]:

$$\Gamma_{rad}^0 \sim \langle \varphi_0^e | \varphi_0^h \rangle^2 \propto 1/(a_X^{2D})^2, \quad (2.16)$$

where φ_0^e and φ_0^h are the electron and hole envelope functions, respectively, and a_X^{2D} is again the exciton radius. The radiative decay rate and the radiative lifetime τ_{rad}^0 are connected as follows [5]:

$$\tau_{rad}^0 = 1/(2\Gamma_{rad}^0). \quad (2.17)$$

Under weak dielectric screening conditions, a relatively small exciton radius ($\approx 1\text{nm}$ [108]) is expected, which yields $\hbar\Gamma_{rad}^0 \gtrsim 1\text{meV}$ and hence a radiative lifetime of $\tau_{rad}^0 \lesssim 1\text{ps}$ [5]. Such prediction exhibits good agreement with the radiative lifetimes obtained via low-temperature time-resolved PL spectroscopy as shown in Table 2.3. Also, the X^- radiative lifetime is measured as $\approx 15\text{ps}$ at low temperature for MoSe_2 and WSe_2 MLs [105, 109, 110] which is expected to be larger than the neutral exciton due to the reduced binding energy.

Table 2.3: Measured and calculated values of τ_{rad}^0 for the neutral exciton of the MoSe_2 ML. The calculated values were extracted from Ref. [111].

Material	τ_{rad}^0 (ps)	
	Measured	Calculated
MoS_2	5 [112]	3.7
MoSe_2	1.8 [105]	5.0
WS_2	0.64 [113]	2.3
WSe_2	2.0 [105]	3.8

Figure 2.11 shows the MoSe_2 ML neutral exciton radius (a_X^{2D}) as a function of the substrate dielectric constant (ϵ_B) calculated using Coulomb (red dots), RK (blue dots) and full potential (green dots) models for the electron-hole interaction, and considering $\epsilon_T = 1$. The calculations were also carried out by Prof. Andrey Chaves (Departamento de Física - Universidade Federal do Ceará).

Figure 2.11 shows that, under weak dielectric screening, RK and the full potential estimate a_X^{2D} to be on the same order of magnitude ($\sim 1\text{nm}$), which yields similar radiative lifetimes of approximately 1 ps, according to Equations 2.16 and 2.17. This result agrees with the experimental observations achieved using substrates with low dielectric constant or encapsulated with h-BN ($\epsilon_B \approx 4\epsilon_0$), whose dielectric constant

is represented by the orange dashed vertical line. Yet on the weak dielectric screening, the Coulomb model predicts a $\sim 10\times$ smaller exciton radius, which would lead to a radiative lifetime on the order of fs, which is way smaller than the reported values. On the other hand, both Coulomb and RK models predict a relatively large a_X^{2D} as ε_B increases and the dielectric screening is enhanced, reaching up to almost 3nm at $\varepsilon_B \approx 56\varepsilon_0$, which is the LiNbO₃ dielectric constant and is represented by the black dashed vertical line. Equations 2.16 and 2.17 estate that such an increase ($\approx 3\times$) in a_X^{2D} would lead to would lead to a corresponding growth of $\approx 10\times$ of the radiative lifetime, reaching up to the same order of magnitude of the trion radiative lifetime [105]. However, the full potential predicts only a small increase of a_X^{2D} at the strong dielectric screening regime, which would lead to a minor increase on τ_{rad}^0 . Nevertheless, since the full potential model is more appropriate to describe the exciton interaction on the strong dielectric screening regime, as discussed in section 2.3.1, it is reasonable to expect small variations on τ_{rad}^0 .

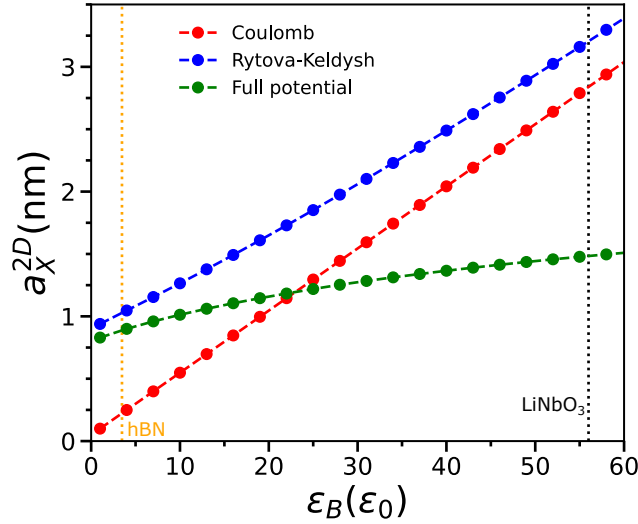


Figure 2.11: Neutral exciton radius (a_X^{2D}) as a function of the substrate dielectric constant ε_B calculated using the 2D Hydrogen model (red), the Rytova-Keldysh approximation (blue), and the full interaction potential [94] (green). The dielectric constants of LiNbO₃ (≈ 56) and h-BN (≈ 4) are indicated by the vertical lines. The calculations of a_X^{2D} were carried out by Andrey Chaves (Departamento de Física - Universidade Federal do Ceará).

Recent reports [68, 69], including the results of this thesis (as discussed in

Chapter 6), suggest that τ_{rad}^0 is much less affected by the substrate dielectric constant than $E_B^{X^0}$. In section 6.5, we show that, under strong dielectric screening, the field-induced exciton dissociation rates are compatible with an exciton radiative lifetime of a few ps instead of tenths of ps, which indicates a small variation of the exciton radius as ε_B increases.

CHAPTER 3

Surface Acoustic Waves

This chapter is dedicated to the description of propagating SAWs on piezoelectric solids. We begin by bringing the theory of elasticity and piezoelectricity to derive the general wave equation for a piezoelectric solid medium and discuss the particular solutions for the Rayleigh waves. Furthermore, we give special attention to Rayleigh modes on LiNbO₃ substrates.

After the general description we deal with the SAW-induced acoustic modulation of low-dimensional semiconductor systems focusing on the bandgap modulation, exciton dissociation and acoustic transport. We conclude with a discussion about acoustic modulation experiments on TMD systems.

3.1 Wave propagation in piezoelectric solids

3.1.1 Strain

A solid is put under stress under the application of forces [114]. An acoustic wave is a moving disturbance within the solid medium which causes a generic infinitesimal volume to exhibit a displacement $\vec{u}(\vec{r})$ from the equilibrium position \vec{r}_0 given by:

$$\vec{u}(\vec{r}) = \vec{r} - \vec{r}_0. \quad (3.1)$$

Particularly, a plane wave disturbance is written as [114]:

$$\vec{u}(\vec{r}, t) = (u_x \hat{x} + u_y \hat{y} + u_z \hat{z}) e^{i(\vec{k}\vec{r} - \omega t)}, \quad (3.2)$$

where u_j ($i = x, y, z$) are the spatial amplitudes in a 3D cartesian coordinate system, \vec{k} is the wave vector and ω is the angular frequency of the wave.

Unidimensional case

We begin by considering a situation in which an extensible string with negligible mass and length L is fixed on a rigid wall by one end and is pulled by a force \vec{F} on the other end. Figure 3.1 shows the unstressed string (at the top) with total length L and two points A and B located at the coordinates x and $x + \Delta x$, respectively. At the bottom, the string is extended due to the force \vec{F} so that it has now a total length $L + \Delta L$. The points A and B are displaced to points A' and B' with coordinates x' and $x' + \Delta x'$, respectively. According to Equation 3.1 the displacement of points A and B are given by:

$$\begin{aligned} u(x) &= x' - x, \\ u(x + \Delta x) &= (x' + \Delta x') - (x + \Delta x). \end{aligned} \quad (3.3)$$

From the last we have:

$$u(x + \Delta x) = (x' - x) + (\Delta x' - \Delta x) = u(x) + \Delta u(x), \quad (3.4)$$

which states that the segment AB is deformed if $\Delta u(x) \neq 0$. In this case, the relative deformation writes as:

$$\frac{\Delta L}{L} = \frac{u(x + \Delta x) - u(x)}{\Delta x}, \quad (3.5)$$

which defines the strain at the limit of an infinitesimal Δx as:

$$S = \lim_{\Delta x \rightarrow 0} \frac{u(x + \Delta x) - u(x)}{\Delta x} = \frac{du(x)}{dx}. \quad (3.6)$$

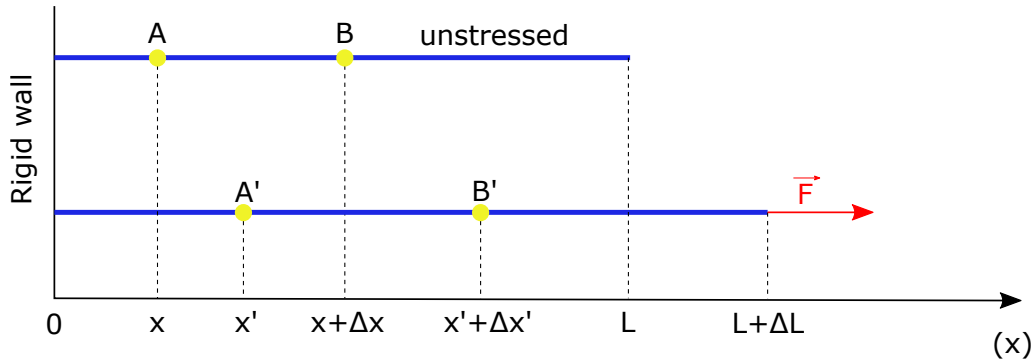


Figure 3.1: Illustration of an extensible string that is fixed to a rigid wall on the left and is being pulled to the right. The string undergoes elastic deformation, increasing its length (L). At the top, the string is unstressed and the points A and B, which are located in x and $x + \Delta x$, respectively. At the bottom, the string is stressed by the application of an external force \vec{F} , which causes the points A and B to be displaced to points A' and B' located in x' and $x' + \Delta x'$, respectively. The total length increases from L to $L + \Delta L$. Adapted from [115].

The strain is a non-dimensional physical quantity which relates to deformations in solid media.

Threedimensional case

In a 3D medium, the application of a force leads to displacement in all directions with the presence of mixed terms, i.e. a deformation caused in a given direction is responsible for deformations in the other directions. In this way, S is represented by a rank-2 tensor [50] as:

$$\hat{S}_{ij} = \frac{\partial u_i}{\partial x_j}, \quad (3.7)$$

where $i, j = 1, 2, 3$ where we refer to the indexes x, y , and z as $x \rightarrow x_1, y \rightarrow x_2$, and $z \rightarrow x_3$.

Different from the 1D case, the condition of $\partial u_i / \partial x_j \neq 0$ is not enough to determine the presence of a deformation, since Equation 3.7 also accounts for rotations of the solid, which must be removed from the definition of the strain field. This is

achieved by choosing a symmetric definition of the strain [114]:

$$\hat{S}_{ij} = \frac{1}{2} \left\{ \frac{\partial u_i}{\partial x_j} + \frac{\partial u_j}{\partial x_i} \right\}, \quad (3.8)$$

which implies $\hat{S}_{ij} = \hat{S}_{ji}$ and thus the strain tensor has only 6 independent elements in a three-dimensional system.

As discussed in the unidimensional case, the definition of strain relates to the local deformation per unit of (non-deformed) length. In the general three-dimensional case, one of the strain components is associated to the local volume changes (δV) per unit of unstrained volume (V) as defined by the ratio $\delta V/V$. Here we refer to an arbitrary volume V without loss of generality as a region of the media whose dimensions exceeds the interatomic distances but are negligible when compared to the elastic characteristics of the systems such as the wavelength or the total extension.

3.1.2 Stress

Mechanical forces act within a deformed solid and tend to restore the structure to the rest position in order to achieve mechanical equilibrium and energy minimization [50]. Such forces are the manifestation of the interaction of neighboring elements of the solid and are transmitted progressively through the material by interatomic forces. The internal forces are described by means of the stress tensor T_{ij} .

Consider a region of volume V within a strained solid media enclosed by a surface A and a unit normal vector to any surface element dA as $\hat{l} = (l_1, l_2, l_3)$. The mechanical traction (\vec{T}), which is the measure of force per unit of area exerted by the volume V through the surface A points into $-\hat{l}$, although they are not necessarily parallel due the possibility of shear forces being transmitted through the surface. \vec{T} is given as [50]:

$$\vec{T}(\hat{l}) = \lim_{\Delta A \rightarrow 0} \frac{\Delta \vec{F}}{\Delta A} = \frac{d\vec{F}}{dA}. \quad (3.9)$$

The mechanical stress can be defined by imposing the condition of mechanical

equilibrium for the volume V , where the resultant force \vec{F} is the sum of the mechanical tractions (\vec{T}) on its surface and the internal forces per unit of volume f_i , so that the i component of \vec{F} is given by:

$$F_i = \int_A T_i(\hat{l}) d\vec{A} + \int_V f_i dV = 0, \quad (3.10)$$

being T_i the i -th component of the traction.

According to the divergence theorem [50, 115]:

$$\int_A T_i(\hat{l}) d\vec{A} = \int_A T_{ij} l_j dA = \int_V \left(\frac{\partial T_{ij}}{\partial x_j} \right) dV, \quad (3.11)$$

so that:

$$f_i = - \sum_{j=1}^3 \frac{\partial T_{ij}}{\partial x_j}. \quad (3.12)$$

As a consequence of 3.10 and 3.11, we have:

$$T_i(\hat{l}) = \sum_{j=1}^3 T_{ij} l_j, \quad (3.13)$$

where T_{ij} is called stress and represents the i -th force component per unit of area on the x_j direction. Equivalently:

$$T_{ij} = \lim_{\Delta A_j \rightarrow 0} \frac{\Delta F_i}{\Delta A_j} = \frac{dF_i}{dA_j}. \quad (3.14)$$

3.1.3 Generalized Hooke's law

The theory of elasticity states that a solid is elastic if it completely restores the original state after being deformed by a force, and linear if the strain is linearly proportional to small stresses [116]. In this case, the elastic behavior can be described by the linear element of a Taylor expansion of $T_{ij}(\hat{S}_{kl})$ around $\hat{S}_{kl} = 0$:

$$T_{ij}(\hat{S}_{kl}) \approx T_{ij}(0) + \sum_{k,l} \hat{S}_{kl} \left(\frac{\partial T_{ij}}{\partial \hat{S}_{kl}} \right) \Big|_{\hat{S}_{kl}=0} + \mathcal{O}(2). \quad (3.15)$$

Since $T_{ij}(0) = 0$, we have:

$$T_{ij} = \sum_{kl} c_{ijkl} \hat{S}_{kl}, \quad (3.16)$$

which is the generalized form of Hooke's law (also referred to as the elastic constitutive relation [114]) in three dimensions, and

$$c_{ijkl} = \left(\frac{\partial T_{ij}}{\partial \hat{S}_{kl}} \right) \Big|_{\hat{S}_{kl}=0}, \quad (3.17)$$

is the stiffness tensor, a rank-4 tensor with 81 elements. The elements of c_{ijkl} (the elastic stiffness constants) act as microscopic spring constants on the description of the resulting strain of a given applied stress and are expressed in units of N/m^2 . Moreover it fully describes the elastic behavior of a solid in the limit of small deformations [114].

3.1.4 Matrix notation

The strain and stress tensors are symmetric [50, 114, 116]. As a consequence, the elastic constants defined by the stiffness tensor in equation 3.16 are invariant under transformations $(ij) \rightarrow (ji)$ and $(kl) \rightarrow (lk)$ so that the number of independent terms is reduced from 81 to 36. In fact, each set (ij) or (kl) in fact can only represent 6 independent elements, which are enumerated as follows:

$$\begin{aligned} (xx) &\leftrightarrow 1, & (yy) &\leftrightarrow 2, & (zz) &\leftrightarrow 3, \\ (yz) = (zy) &\leftrightarrow 4, & (zx) = (xz) &\leftrightarrow 5, & (xy) = (yx) &\leftrightarrow 6. \end{aligned} \quad (3.18)$$

In other words, the stiffness tensor can be written as a square 6×6 array as $c_{\alpha\beta} = c_{ijkl}$, where $\alpha \leftrightarrow (ij)$ and $\beta \leftrightarrow (kl)$ in the so-called matrix [50] or engineering [117] notation, which also extends for stress and strain tensors. Furthermore, with general thermodynamics arguments [50], the Maxwell's relation states that $c_{\alpha\beta}$ is symmetric hence the number of independent elements is further reduced to 21. The individual crystal symmetry is responsible for a further limitation of the number of independent

elements for a given material.

3.1.5 Equation of motion in non-piezoelectric solids

Consider the classic spring-mass problem in one dimension in which a point mass m is attached to the tip of a spring with spring constant k_s and negligible mass. When a force \vec{F}_1 is applied to the mass and extends the spring by a given length u_i on the positive \hat{x}_i direction, a restoring force $\vec{F}_R = -k_s u_i \hat{x}_i$ arises in order to oppose the deformation and restore the equilibrium state. When \vec{F}_1 is released, the motion is driven by the restoring force and Newton's second law writes as:

$$m \frac{d^2 u_i}{dt^2} = -k_s u_i, \quad (3.19)$$

which is the equation of motion of a unidimensional spring-mass oscillator in the absence of damping.

Similarly to the 1D spring-mass problem one can write the equation of motion for a 3D solid using the definition of the restoring forces f_i given by Equation 3.12 which leads to:

$$m \frac{d^2 u_i}{dt^2} = \sum_{j=1}^3 \int_V f_i dV = \sum_{j=1}^3 \int_V \frac{\partial T_{ij}}{\partial x_j} dV. \quad (3.20)$$

In the limit of $V \rightarrow 0$ the term $\partial T_{ij}/\partial x_j$ can be taken as a constant so:

$$\begin{aligned} m \frac{d^2 u_i}{dt^2} &= \sum_{j=1}^3 \frac{\partial T_{ij}}{\partial x_j} \int_V dV = \sum_{j=1}^3 \frac{\partial T_{ij}}{\partial x_j} V \\ \implies \rho \frac{d^2 u_i}{dt^2} &= \sum_{j=1}^3 \frac{\partial T_{ij}}{\partial x_j}, \end{aligned} \quad (3.21)$$

where $\rho = m/V$ is the mass density of the material. Moreover, if we recall the Hooke's law from Equation 3.16 we have:

$$\rho \frac{d^2 u_i}{dt^2} = \sum_{j=1}^3 \frac{\partial}{\partial x_j} c_{ijkl} \hat{S}_{kl}, \quad (3.22)$$

where we use the definition of strain from Equation 3.8 to arrive at:

$$\rho \frac{d^2 u_i}{dt^2} = \sum_{j,k,l=1}^3 \frac{\partial}{\partial x_j} \left[\frac{c_{ijkl}}{2} \left(\frac{\partial u_k}{\partial x_l} + \frac{\partial u_l}{\partial x_k} \right) \right]. \quad (3.23)$$

Finally, we resort to symmetry arguments on strain and stress tensors which make c_{ijkl} invariant under transformations of the first or the second pair of indexes [50] in order to obtain:

$$\rho \frac{d^2 u_i}{dt^2} = \sum_{j,k,l=1}^3 c_{ijkl} \frac{\partial^2 u_l}{\partial x_j \partial x_k}. \quad (3.24)$$

Equation 3.24 represents the wave equation within solid media in three dimensions and fully describes the propagation modes of elastic waves in homogeneous and non-piezoelectric solids. Each material and set of boundary conditions define the particular solutions for the wave equation that can arise. Figure 3.2 shows three examples of elastic modes that constitute solutions of Equation 3.24 for specific boundary conditions. The grids represent perfect cubic lattices, which are used for the representation without loss of generality. Figures 3.2.a and 3.2.b show illustrations of bulk compressive (longitudinal) and transverse (shear) waves, respectively. These modes are obtained for unbound solids and achieve propagation velocities of the order of 4000 – 12000m/s for the compressive and 2000 – 6000m/s for longitudinal and transverse modes, respectively [114]. Figure 3.2.c shows the Rayleigh mode, which raises for semi-infinite solids and whose particle motion extends below the surface to a depth of about one wavelength (λ_{SAW}) [114]. The description of other SAW modes, such as Love and Bleustein-Gulyaev can be found in references [50] and [117].

3.1.6 Piezoelectricity

Up to this point we have dealt with non-piezoelectric solids. However the coupling between the mechanical variables (strain and stress) and the electrical variables (electric field and electric displacement) in piezoelectric crystals creates mechanisms for generation and detection of acoustic waves [114]. Moreover we are especially

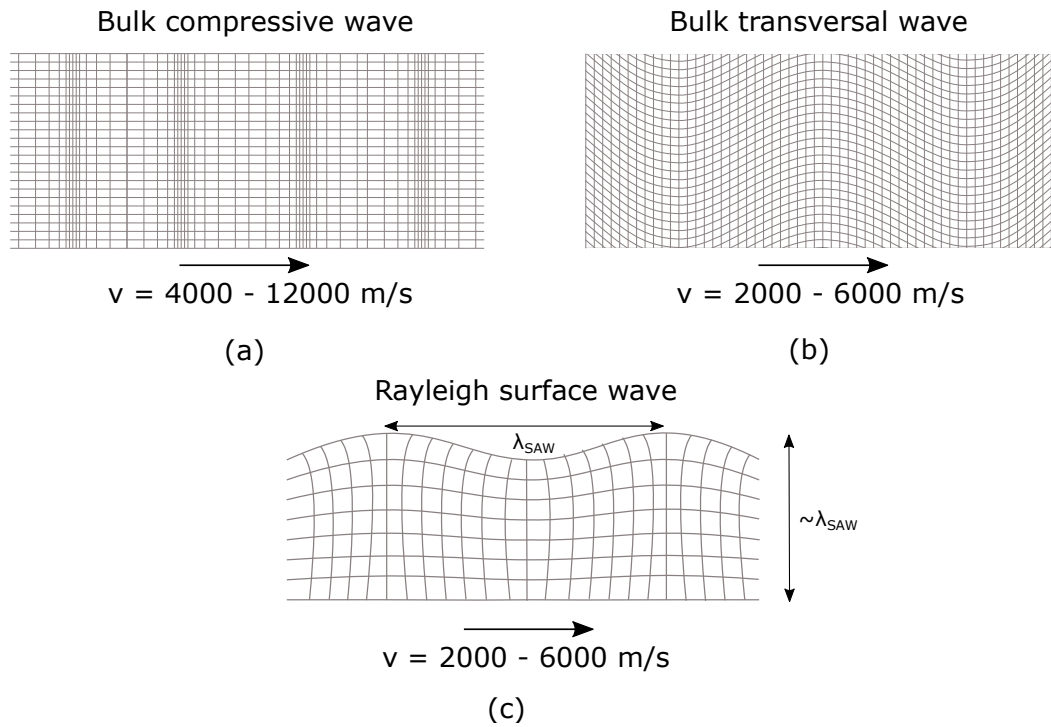


Figure 3.2: Representation of different elastic modes in solids. (a) Bulk longitudinal (compressive) wave. (b) Bulk transverse (shear) wave. (c) Rayleigh wave. Adapted from [114].

interested in the SAW modes in piezoelectric solids and in the acoustically-driven modulation in condensed matter, which rely on the superposition of mechanical and piezoelectric fields [48, 51], as will be discussed next sections.

A material is said to be piezoelectric when it exhibits the capability to develop a finite electric charge unbalance in the presence of a mechanical stress. This property arises in non-centrosymmetric crystalline solids, i.e. solids whose crystalline unit cell lacks an inversion center [50, 114, 116]. Figure 3.3 illustrates a crystal being submitted to compressive and tensile stresses and the accumulation of charges in both cases. The crystal is represented as a hexagonal structure for simplicity without loss of generality.

Figure 3.3.a shows the crystal in the absence of mechanical stresses. In this case the rest positions of the atoms guarantee the charge balance. Under stress, the atoms leave their equilibrium position giving rise to a charge unbalance that polarizes the

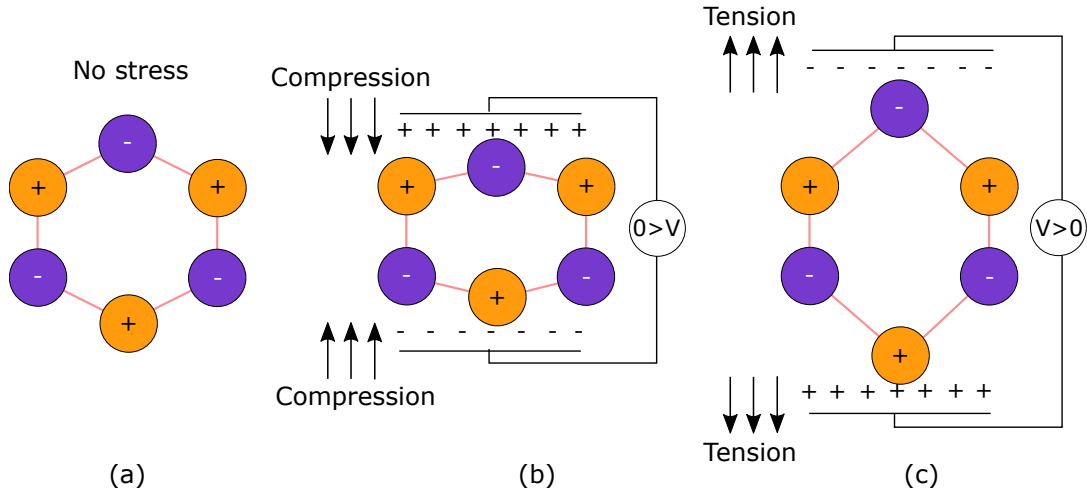


Figure 3.3: Representation of the piezoelectric effect. In the absence of a net stress (a) the piezoelectric crystal is charge-balanced and no electric field is induced. However the application of compressive (b) and tensile (c) stresses lead to opposite charge unbalances.

crystal. The induced polarization has opposite signs for compression and tension, as illustrated in Figures 3.3.b and 3.3.c, respectively. If it were possible to connect a voltmeter to the stressed crystal one would read a negative value ($V < 0$) in the situation of a compression and a positive one ($V > 0$) in the situation of a tension.

The coupling of mechanical and electric variables in a piezoelectric solid gives rise to a set of piezoelectric constitutive relations between T_{ij} , \hat{S}_{kl} , the electric field E_l , and the electric charge displacement D_k as follows [50, 114]:

$$\begin{aligned} T_{ij} &= \sum_{k,l} c_{ijkl} \hat{S}_{kl} - \sum_l e_{ijl} E_l \\ D_k &= \sum_{i,j} e_{kij} \hat{S}_{ij} + \sum_l \varepsilon_{kl} E_l, \end{aligned} \quad (3.25)$$

where e_{ijl} and ε_{kl} are the piezoelectric and static dielectric tensors, respectively. The piezoelectric tensor (also known as coupling matrix) inherits the symmetric characteristics of stress and strain thus $e_{lij} = e_{lji}$ and it exhibits only 18 independent terms (instead of 27). Moreover it can also be written in the matrix notation as $e_{lij} = e_{l\alpha}$. Finally, the material elastic properties are included in the problem via the stiffness tensor in Equations 3.25.

3.1.7 Wave equation for piezoelectric solids

Now that we have the piezoelectric constitutive relations given by Equations 3.25 we can rewrite Equation 3.21 in order to obtain the wave equation for a piezoelectric homogeneous solid as follows:

$$\rho \frac{d^2 u_i}{dt^2} = \sum_{j=1}^3 \frac{\partial T_{ij}}{\partial x_j} = \sum_{j=1}^3 \left\{ \sum_{kl} \frac{\partial (c_{ijkl} \hat{S}_{kl})}{\partial x_j} - \sum_l \frac{\partial e_{ijl} E_l}{\partial x_j} \right\}. \quad (3.26)$$

Once again we assume that we are working in an infinitesimal volume domain in which the properties of the material given by c_{ijkl} , e_{ijl} , and ε_{kl} are constants, so:

$$\rho \frac{d^2 u_i}{dt^2} = \sum_{j=1}^3 \left\{ \sum_{kl} c_{ijkl} \frac{\partial \hat{S}_{kl}}{\partial x_j} - \sum_l e_{ijl} \frac{\partial E_l}{\partial x_j} \right\}. \quad (3.27)$$

Here we introduce the piezoelectric potential ϕ as:

$$E_l = -\frac{\partial \phi}{\partial x_l}, \quad (3.28)$$

which leads to the wave equation:

$$\rho \frac{d^2 u_i}{dt^2} = \sum_{jkl} c_{ijkl} \frac{\partial u_l}{\partial x_j \partial x_l} + \sum_{jl} e_{ijl} \frac{\partial^2 \phi}{\partial x_j \partial x_l}, \quad (3.29)$$

where we also used Equation 3.8.

Equation 3.29 is the wave equation for piezoelectric solids. The term with the piezoelectric potential may be taken as a source term which is responsible for the generation of an elastic wave upon the application of a time-dependent electric potential [114]. Furthermore, the wave displacements are responsible for the generation of an electric potential that follows the wave.

3.2 The Rayleigh mode in piezoelectric solids

Surface modes constitute a special class of solutions of Equation 3.29 comprised by low-frequency acoustic phonons strongly localized at the surface of the media

and whose wave-vector (k_{SAW}) usually exhibits a linear energy dispersion [50, 114, 116, 117]. Also, SAW modes are generally slower than bulk modes, so the surface acts as a waveguide allowing for high acoustic energy densities to arise in these regions [115, 118].

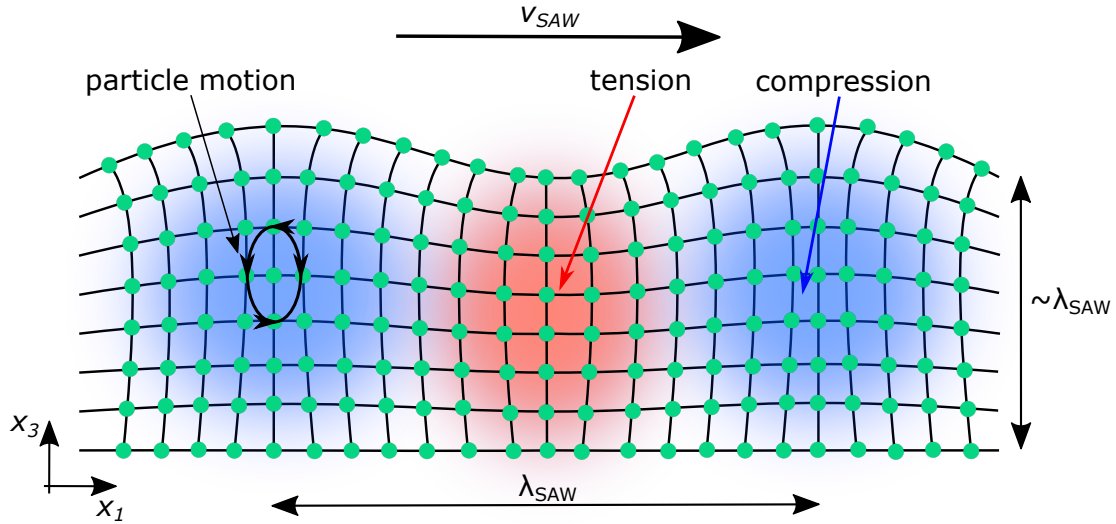


Figure 3.4: Strain profile of a propagating Rayleigh wave with wavelength λ_{SAW} and velocity v_{SAW} in the x_1 direction. The regions of compression and tension are indicated in blue and red, respectively. The particle exhibits an elliptic motion due to the superposition of transverse and longitudinal modes.

A particular SAW mode, known as Rayleigh wave [119], consists of a superposition of a longitudinal and transverse acoustic modes [118] propagating in half-spaces [116]. Figure 3.4 illustrates a Rayleigh mode with wavelength λ_{SAW} propagating along the x_1 direction with velocity v_{SAW} . We consider a medium with infinite extension in the x_1Ox_2 plane with a boundary at $x_3 = 0$ in such a way that the solid occupies the space $x_3 < 0$ and the space $x_3 > 0$ is free (vacuum or air) [116, 118]. The grid represents the crystalline structure and the green circles are the atoms. Due to the superposition of transverse and longitudinal mode the particle motion follows an elliptic motion.

In order to describe the general solution for the Rayleigh mode in piezoelectric homogeneous solids obtained from Equation 3.29 it is necessary to impose boundary

conditions regarding mechanical and electrical variables as follows [50, 114–118, 120]:

$$T_{ij}(x_3 = 0) = 0; \quad (3.30a)$$

$$|\vec{u}| \rightarrow 0 \text{ as } u_3 \rightarrow 0; \quad (3.30b)$$

$$E_t(x_3 > 0) = E_t(x_3 < 0); \quad (3.30c)$$

$$D_n(x_3 > 0) - D_n(x_3 < 0) = \sigma. \quad (3.30d)$$

The first two equations state boundary conditions for the mechanical variables. First the surface must be stress-free (Equation 3.30a) since no mechanical forces act across $x_3 = 0$. Equation 3.30b imposes that the displacement vector \vec{u} decays with the depth of the substrate which is a necessary condition for any surface mode. The last two equations express the continuity of the tangential component of the electric field (E_t) and the normal component of the electric displacement (D_n) across the surface. Equation 3.30c guarantees the continuity of the piezoelectric potential ϕ_{SAW} across the surface as well. The boundary condition of D_n accounts for the surface charge density (σ), if any (in the case of metalized surfaces). Surface current density also shall be taken into account when necessary [50].

When applied to Equation 3.29 the boundary conditions from Equations 3.30a-d lead us to a set of equations that brings up the presence of the mixed terms of displacement in directions \hat{x}_1 and \hat{x}_3 which evidences the coupling of normal modes (longitudinal and transverse). It is important to note that the boundary conditions also hold for layered structures, but the normal stress components need to be continuous at the interface between layers [50].

The solutions of the wave equations for the Rayleigh mode are of the form [121]:

$$u_j(x_1, x_3, t) = U_j \exp \{i(k_{SAW}x_1 - \omega t + \varphi_j)\} e^{-\alpha_j x_3}; \quad (3.31a)$$

$$\phi_{SAW}(x_1, x_3, t) = \phi_0 \exp \{i(k_{SAW}x_1 - \omega t)\} e^{-\alpha_j x_3}, \quad (3.31b)$$

where k_{SAW} is the SAW wave vector, and ω is the angular frequency. U_j (with $j = 1, 3$.) and ϕ_0 are the displacement and piezoelectric potential amplitudes, respectively, α_j is the acoustic damping parameter and φ_j is a relative phase. Both Equations 3.31b-b exhibit a propagating and a decay term indicating that the wave is mainly concentrated around the surface and the amplitude decays exponentially along the depth of the material. Moreover the amplitudes vary at different rates in directions so that u_1 and u_3 are said to be in phase quadrature [50, 116] i.e.:

$$\varphi_1 - \varphi_3 = \pm \frac{\pi}{2}; \quad (3.32)$$

At the surface, the particle motion is retrograde but it becomes prograde at a depth of $\sim 0.2\lambda_{SAW}$ because the longitudinal component changes sign. Finally, since the amplitudes U_j are typically different for each direction, the motion describes an ellipse [50].

3.2.1 Rayleigh waves in LiNbO₃

Lithium niobate (LiNbO₃) is a piezoelectric material with a trigonal crystal structure from the point group 3m [50] that exhibits high piezoelectric and dielectric constants besides interesting applications in photonics [122]. LiNbO₃ has been employed as one of the main platforms for technology development and scientific research in the context of SAWs [50, 116, 122].

In order to explore the symmetry properties and anisotropy effects of the LiNbO₃ crystal, different crystallographic surface cuts are used. In particular, 128Y° LiNbO₃ - which is a cut whose surface is rotated by 128° from the y crystallographic direction of the LiNbO₃ crystal around the z crystallographic axis - exhibits one of the highest SAW propagation velocities (v_{SAW}) and electromechanical coupling coefficients (k^2) for the propagation of a Rayleigh mode in the x crystallographic direction, for this reason this cut is also known as 128Y°-X LiNbO₃. The electromechanical coupling coefficient is a measurement of the efficiency of converting an electric signal into an acoustic wave, and is reported as $k^2 \approx 5.4\%$ [50, 116] for

128°Y-X LiNbO₃. Other cut directions, such as 64°Y-X, and 41°Y-X can generate pseudo-SAW (PSAW) modes, also known as leaky SAW, that are solutions for the wave equation with high transverse (shear) phase velocity which leads to excitation of bulk modes [50]. Yet another cut is the Y-Z LiNbO₃ which is a y surface that allows for the generation of Rayleigh waves in the z direction [50, 116]. The LiNbO₃ cuts exhibit higher velocities and coupling coefficients than most piezoelectric materials that have been used in SAW technology such as Quartz and LiTaO₃ [120]. Table 3.1 shows the parameters of v_{SAW} and k^2 for the cited materials.

Table 3.1: Characteristics of piezoelectric materials related to generation and propagation of SAWs and PSAWs. Adapted from Refs. [50, 116].

Material	Type	v_{SAW} (m/s)	k^2 (%)	Ref.
128°Y-X LiNbO ₃	SAW	3959	5.4	[50]
64°Y-X LiNbO ₃	PSAW	4695	11.6	[50]
41°Y-X LiNbO ₃	PSAW	4480	21	[50]
Y-Z LiNbO ₃	SAW	3488	4.8	[116]
Quartz ¹	SAW	3150	0.12	[50]
36°Y-X LiTaO ₃	PSAW	4240	4.7	[50]
X-122°X LiTaO ₃ ²	SAW	3300	0.85	[50]

We are particularly interested in the description of the Rayleigh modes in 128°Y LiNbO₃ substrates. The stiffness ($c_{\alpha\beta}$), piezoelectric ($e_{i\alpha}$), and dielectric (ε_{ij}) tensors (in matrix notation) are given by [123]:

$$[c_{\alpha\beta}](\text{LiNbO}_3) = \begin{bmatrix} 20.30 & 7.00 & 5.80 & 1.30 & 0.0 & 0.0 \\ 7.00 & 19.40 & 9.10 & 0.90 & 0.0 & 0.0 \\ 5.80 & 7.50 & 24.5 & 0.86 & 0.0 & 0.0 \\ 1.3 & -0.90 & 0.86 & 7.58 & 0.0 & 0.0 \\ 0.0 & 0.0 & 0.0 & 0.0 & 5.69 & -0.50 \\ 0.0 & 0.0 & 0.0 & 0.0 & -0.5 & 7.81 \end{bmatrix} \times 10^{10} N/m^2, \quad (3.33)$$

¹Quartz cut in the y+36° direction and wave propagation in the x direction.

²LiTaO₃ cut in the x direction and wave propagation in the y+122° direction.

$$[e_{i\alpha}](\text{LiNbO}_3) = \begin{bmatrix} 0.0 & -1.85 & 1.692 \\ 0.0 & 4.44 & -2.672 \\ 0.0 & -1.544 & 2.322 \\ 0.0 & 0.091 & 0.604 \\ 4.455 & 0.0 & 0.0 \\ 0.297 & 0.0 & 0.0 \end{bmatrix} C/m^2, \quad (3.34)$$

and

$$[\varepsilon_{ij}](\text{LiNbO}_3) = \begin{bmatrix} 44 & 0.0 & 0.0 \\ 0.0 & 38.75 & -7.27 \\ 0.0 & -7.27 & 34.65 \end{bmatrix} \times 10^{-11} F/m, \quad (3.35)$$

respectively. These constants enter in Equations 3.31b (a-b) and determine the Rayleigh modes in 128°Y LiNbO₃ substrates as will be shown in chapter 5.

We are also interested on the propagation of SAWs on MoS₂ and MoSe₂ MLs. For this, computational calculations were carried in order to obtain the SAW modes and the field amplitudes at the ML, and are discussed in Chapter 5. The TMD MLs are considered to be 0.6 nm thick [124] in the calculations. The MoSe₂ and MoS₂ ML were assumed to be isotropic with a Young's modulus of 224 GPa and 246 GPa, respectively [125]. The piezoelectric constants for the ML materials were adopted from density functional theory simulations [126], which have been shown to agree with experimental values [124]. The piezoelectric ($e_{i\alpha}$) and dielectric (ε_{ij}) tensors (in matrix notation) are therefore given by:

$$[e_{i\alpha}](\text{MoSe}_2) = \begin{bmatrix} 0.65 & -0.65 & 0.0 & 0.0 & 0.0 & 0.0 \\ 0.0 & 0.0 & 0.0 & 0.0 & 0.0 & -0.65 \\ 0.0 & 0.0 & 0.0 & 0.0 & 0.0 & 0.0 \end{bmatrix} C/m^2, \quad (3.36)$$

$$[\varepsilon_{ij}](\text{MoSe}_2) = \begin{bmatrix} 15.71 & 0.0 & 0.0 \\ 0.0 & 15.71 & 0.0 \\ 0.0 & 0.0 & 3.78 \end{bmatrix} \times 10^{-11} F/m, \quad (3.37)$$

$$[e_{i\alpha}](\text{MoS}_2) = \begin{bmatrix} 0.60 & -0.60 & 0.0 & 0.0 & 0.0 & 0.0 \\ 0.0 & 0.0 & 0.0 & 0.0 & 0.0 & -0.60 \\ 0.0 & 0.0 & 0.0 & 0.0 & 0.0 & 0.0 \end{bmatrix} C/m^2, \quad (3.38)$$

and

$$[\varepsilon_{ij}](\text{MoS}_2) = \begin{bmatrix} 13.00 & 0.0 & 0.0 \\ 0.0 & 13.00 & 0.0 \\ 0.0 & 0.0 & 3.27 \end{bmatrix} \times 10^{-11} F/m, \quad (3.39)$$

respectively.

3.3 Acoustic modulation

After the general description of SAWs in the previous sections, we describe the physical mechanisms of SAW-driven modulation of the optical and emission properties of semiconductor systems that lie on the surface of a piezoelectric material.

3.3.1 Exciton dynamics modulation

The SAWs treated here are mechanical deformations that travel on the surface of a solid with well defined direction and velocity and periodically modify the band structure of the underlying medium by means of the strain and the piezoelectric potential [118]. The strain field carried by the SAW is responsible for the modulation of the electronic bandgap based on the displacement of the atomic position within the crystal structure which causes local variations of volume and symmetry. In general E_{GAP} is decreased in the regions where the crystal is under tension and increased where the crystal is compressed. Taking into account the hydrostatic deformation ($\delta V/V$), as defined in Section 3.1.1 and the hydrostatic bandgap deformation potential (a_0), the main contribution to the amplitude of the bandgap modulation induced by the strain field is given as [127, 128]:

$$\Delta E_{strain} = a_0 \frac{\delta V}{V}. \quad (3.40)$$

The piezoelectric potential ϕ_{SAW} plays an important role in the acoustic modulation dynamics and is usually the most effective mechanism for the manipulation of charge carriers, besides promoting the dissociation of excitons. In general the SAW piezoelectric field, as defined in Equation 3.28 induces an excitonic Stark effect and a subsequent energy modulation ΔE_{Stark} given by [129]:

$$\Delta E_{Stark} = \frac{1}{2}\alpha_X E_{SAW}^2, \quad (3.41)$$

where α is the exciton polarizability and E_{SAW} is the SAW piezoelectric field. However, the Rayleigh mode carries two piezoelectric fields: E_1 and E_3 , which can induce an in-plane and an out-of-plane Stark effect, respectively.

The net effect of the SAW on the emission energy can be understood as a combination of the piezoelectric field (ΔE_{Stark}) and strain (ΔE_{strain}) modulation amplitudes to the excitonic properties and bandgap modulation, respectively [127, 129] as:

$$\Delta E = \Delta E_{Stark} + \Delta E_{strain} = \frac{1}{2}\alpha E_{SAW}^2 + a_0 \frac{\delta V}{V}. \quad (3.42)$$

3.3.2 Acoustic transport and exciton dissociation

Figure 3.5 illustrates the different carrier spacial separation which are induced by the SAW strain and piezoelectric fields. The strain field is responsible for a type-I spacial modulation, as depicted in Figure 3.5.a, in which VB maximum is spatially aligned with the CB minimum (around $k=0$) in the regions where the SAW stress is compressive. On the other hand, the piezoelectric field induces a type-II modulation, as illustrated in Figure 3.5.b, in which VB and CB extrema are shifted by $\lambda_{SAW}/2$. Due to small values of strain and the larger values of piezoelectric fields, the distribution of charge carriers along the SAW wavelength is usually determined by the piezoelectric field [52]. Moreover, depending on the crystal structure, there can be a spatial phase shift between the strain and the piezoelectric modulations which tends to privilege recombination in specific locations along the modulation direction [117].

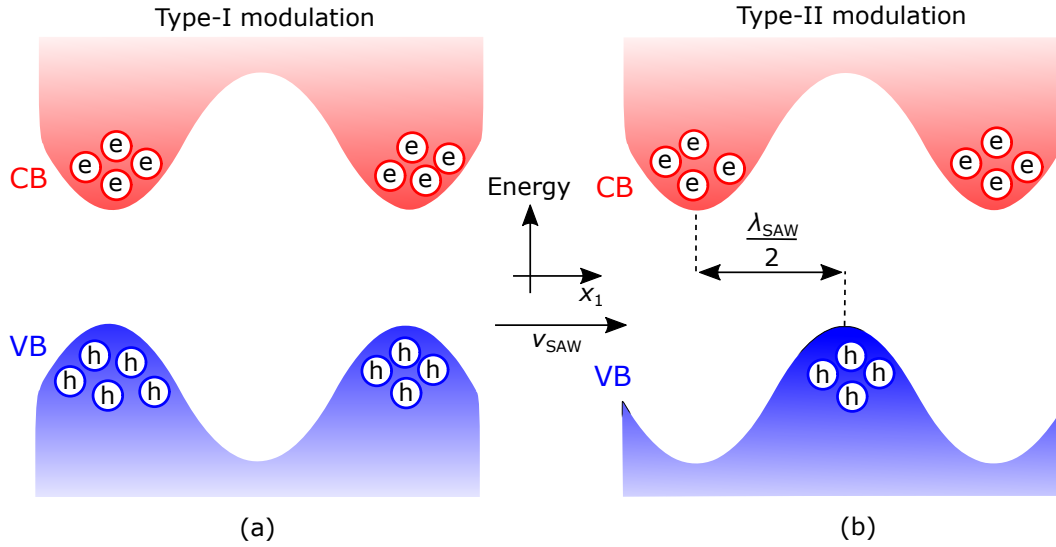


Figure 3.5: Type-I (a) and type-II SAW-induced carrier spatial separation along the propagating direction (x_1). In the type-I spatial modulation, the mechanical displacement traps the charge carriers in the same position. On the other hand, in the type-II spatial modulation electrons and holes are trapped with a separation of $\lambda_{SAW}/2$ due to the piezoelectric potential.

The modulated piezoelectric potential acts as a lateral superlattice that, when strong enough, is able to ionize excitonic complexes and separate the free charge carriers [52, 130]. The trapped carriers are then drifted by the in-plane component of the SAW piezoelectric field. The spatial separation reduces the overlap between the electron and hole wavefunctions, thus increasing the carrier lifetimes, which causes a suppression of the PL intensity at the excitation point and allows the coherent lateral transport of the charge carriers over macroscopic distances, as demonstrated in III-V materials [51, 52]. Along the transport, the charge carriers are able to recombine when the piezoelectric field is screened due to potential fluctuations, point defects or even metallic structures, which leads to remote recombination and subsequent PL emission [52, 53].

The field-induced exciton dissociation in quasi 2D systems has been investigated by means of the solution of exciton of Wannier equation in the presence of an out-of-plane static electric field in III-V quantum wells [130, 131]. This approach is valid for the SAW-driven phenomena if it is assumed that (i) ϕ_{SAW} acts as a weak

perturbation, i.e. has a small amplitude and does not give rise to localized energy levels within the band structure; and (ii) the wave period is longer than the exciton radiative lifetime. In this situation, E_1 dissociates excitons in such systems at a rate τ_{dis}^{-1} given by [130, 131]:

$$\tau_{dis}^{-1} = \frac{8E_B}{\hbar\sqrt{\pi}} \left(\frac{E_B}{2e\hbar E_1} \sqrt{2\mu E_B} \right)^{1/2} \exp \left\{ -\frac{4E_B}{3e\hbar E_1} \sqrt{2\mu E_B} \right\}, \quad (3.43)$$

where E_B is the exciton binding energy and μ is the exciton reduced mass.

3.4 SAWs in 2D TMDs

Preciado and coworkers [36] investigated the transport properties of MoS₂ MLs by means of room-temperature photoconductance spectroscopy experiments. The authors fabricated and characterized a hybrid CVD-grown MoS₂ and 128°Y LiNbO₃ electro-acoustic device in which they employed SAWs to investigate photoconductance properties in electrical contact free device. Using the SAW as a probe, the authors observed two time scales on the decay of the photoconductivity: (i) a fast component in the scale of ms; and a (ii) long decay component in the scale of minutes. The long decay is attributed to persistent photoconductivity, which was later attributed to potential fluctuations along the SAW-driven carrier transport [132, 133].

In the context of optical properties, we point the five principal works that investigate the manipulation of the TMD ML PL emission using propagating SAWs. Rezk and coworkers [70] used SAWs to modulate the room temperature PL emission of few-layered MoS₂ systems (2 - 4 layers) stacked on a LiNbO₃ substrate and observed a suppression of the PL intensity driven by the SAW, in a similar way to III-V semiconductor nanostructures [52, 53]. Moreover, they observed a relation between the PL intensity and the SAW power, indicating that the control of the acoustic beam could also be used for excitonic manipulation. Shortly after the first work, the same group [67] showed the reversible tuning of the PL of single-layered (ML) and odd-layered MoS₂ by exploring the piezoelectricity of the MLs. The samples were CVD-grown on sapphire substrate which, in turn, is placed on top of a

LiNbO₃ substrate in such a way that the SAW is generated on LiNbO₃, propagates through the sapphire and reaches the MoS₂. A 20 μ m thick conductive film between the LiNbO₃ and sapphire suppresses ϕ_{SAW} so that the MoS₂ MLs are only subjected to the strain field and the experiments relies solely on the TMD piezoelectricity. A PL quenching followed by an energy blueshift of the entire excitonic emission band ($X^0 + X^-$ emission lines) has been observed with increasing acoustic power. The blueshift of the excitonic band has been attributed to preferential dissociation of X^- quasi-particles into X^0 . A PL quenching has been also observed for a MoS₂ trilayer while no effects are observed in even-layered samples (2 and 4 layers were tested), thus indicating that the piezoelectric field plays the major role on the PL quenching. The authors also observed the first visual evidence of SAW-induced carrier transport within TMD MLs by imaging the PL emission. These experiments were carried out within the weak dielectric screening regime ($\epsilon(\text{Al}_2\text{O}_3) \sim 10\epsilon_0$ [134]), which diminishes the effects of the SAW fields due to the high binding energy.

Based on the experimental results of the SAW-driven PL modulation in MoS₂ MLs, Huang and coworkers [71] conducted a theoretical investigation of the progression of charge carrier, X^0 and X^- populations on a MoS₂ ML during dynamic photo-generation process under the influence of a SAW by means of a drift-diffusion model. The authors observed a decrease on X^0 and X^- concentrations over time, followed by an increase of carrier population when the SAW beam is present. These observations were attributed to the type-II carrier separation induced by the SAW piezoelectric potential which causes (i) the dissociation of excitonic complexes; and (ii) an increase of carrier lifetimes.

Datta and coworkers [68] investigated the effects of SAWs in exfoliated WSe₂ MLs placed on LiNbO₃ substrates at room temperature. Due the strong dielectric screening provided by the LiNbO₃ substrate, the authors observed a suppression of the PL intensity followed by an energy redshift of the $X^0 + X^-$ emission band. The PL quenching is attributed to the intense SAW-induced exciton dissociation owing to the weakened electron-hole interaction under strong dielectric screening. The redshift on the other hand is attributed to the acoustically-induced Stark effect

due to the intense SAW piezoelectric potential achieved in the highly piezoelectric LiNbO₃ substrate. Furthermore the authors obtained the in-plane X⁰ polarizability of the WSe₂ ML as $8.43 \pm 0.18 \times 10^{-6}$ Dm/V (≈ 87.7 meV/(kV/cm)²).

More recently, Datta and coworkers [135] demonstrated the SAW-driven exciton transport in encapsulated WSe₂ MLs at room temperature also on a LiNbO₃ substrate. For this, the authors screen the piezoelectric field of a propagating SAW beam (at 745MHz) by means of a high concentration of photogenerated charge carriers. As a consequence, the dynamic strain of the SAW promotes a type-I band modulation, which preserves the exciton stability and the non-coherent transport through micrometric distances at a velocity of approximately 600m/s, and results in an exciton mobility of 900 cm²/(eVs).

As a final remark, we point that all SAW-modulated optical spectroscopy experiments on TMD MLs were conducted at room temperature. The experiments on MoS₂ were performed in non-piezoelectric substrates, while the ones on WSe₂ were performed directly on LiNbO₃, as in our experiments which are described in the next chapters.

CHAPTER 4

Experimental methods

4.1 SAW generation and detection

4.1.1 Interdigital transducers for SAW generation

The SAWs are generated via inverse piezoelectric effect. For this, an electric signal is applied to metallic interdigital transducers (IDTs) deposited on the sample surface. An IDT consists of a metal-finger grating with a repetition period equal to the SAW wavelength (λ_{SAW}). The application of a radio frequency (RF) voltage with frequency $f_{SAW} = \lambda_{SAW} \cdot v_{SAW}$ (being f_{SAW} the SAW resonance frequency) leads to the excitation of a propagating SAW mode.

The most common design is the bidirectional single-finger IDT, as shown in Figure 4.1.a. Another very common configuration of a bidirectional IDT is the double-finger IDT, as shown in Figure 4.1.b, which is designed to reduce internal reflections. In both devices, two equal SAW beams are launched to each side when the RF input is turned on. In the design we used in our devices, the SAW wavelength is defined by L_f , the finger width, as $\lambda_{SAW} = 4L_f$ (for single-finger IDTs and $\lambda_{SAW} = 8L_f$ for double-finger IDTs). The aperture W_A defines the IDT output port width.

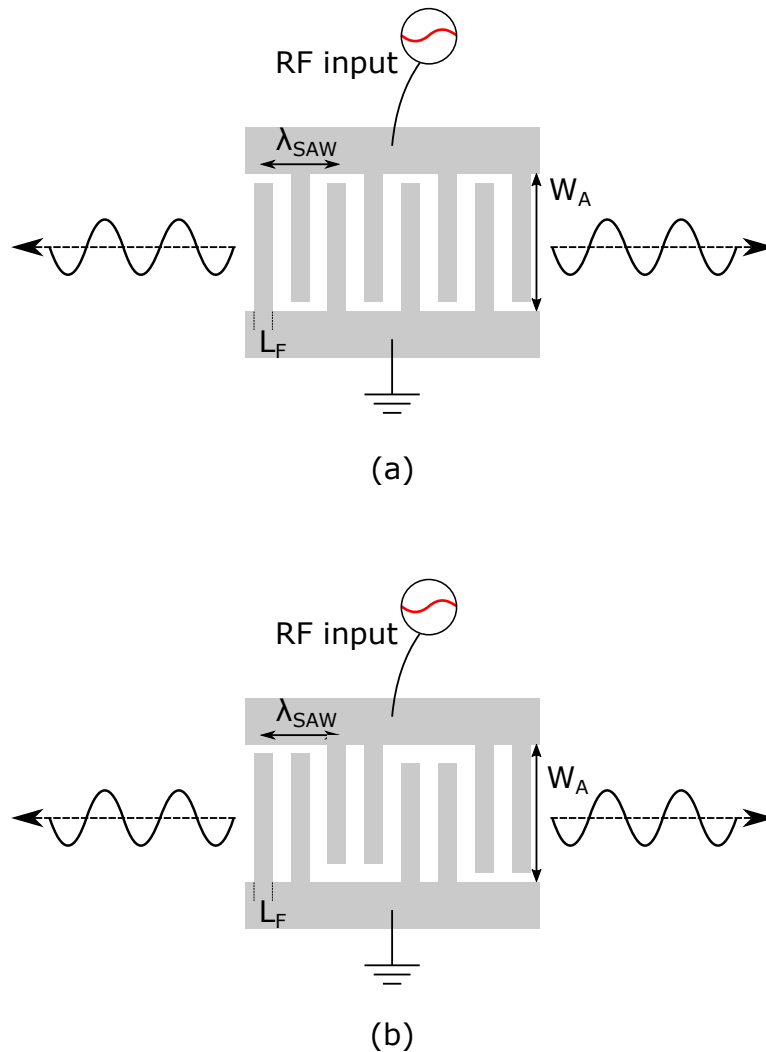


Figure 4.1: Illustration of a bidirectional (a) single-finger and (b) double-finger IDTs. The RF input launches SAW beams on both sides of the transducer. Finger width (L_f), aperture (W_A), and SAW wavelength λ_{SAW} are indicated.

4.1.2 Fabrication

Figure 4.2 shows the illustration of the stages of the photolithography and lift-off techniques which were employed in our fabrication process. Without loss of generality, we describe here the use of positive photoresist. The process begins with the coating of the substrate surface with a photoresist layer using spin-coating. After the coating and thermal treatment of the photoresist, the mask is aligned on the top of the photoresist surface with the aid of a mask aligner for the exposure stage.

The empty (clear) areas of the mask allow the exposure of well-defined regions of the photoresist, which become sensitized. The sensitized regions of the photoresist are then removed at the development stage leaving only the unexposed photoresist (which has the same pattern of the mask) on the surface with an undercut profile, as shown in Figure 4.2. In the metalization stage, a thin metal layer is deposited (usually by e-beam evaporation or sputtering) on the entire surface covering both substrate and photoresist. Finally, the remaining photoresist is removed and carries away the metal that is not in contact with the substrate (due to the lateral profile of the photoresist) leaving the patterned metal device on the surface.

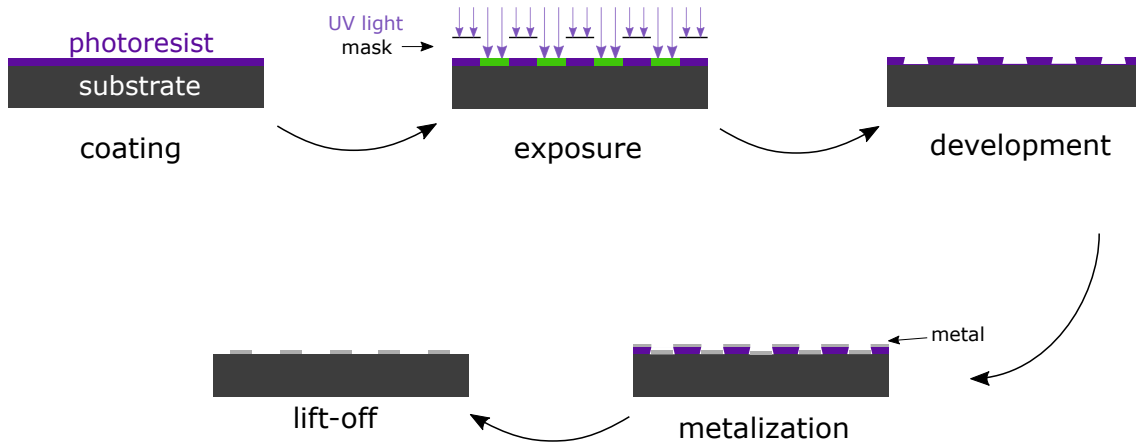


Figure 4.2: Schematic illustration of the stages of the photolithography fabrication.

The photolithography fabrication is limited to a linewidth of ~ 0.8 μm due to interference of diffraction effects [120]. However, such linewidth is enough to fabricate devices with an operational frequency up to 1 GHz on most piezoelectric materials due to the high SAW velocity.

The photolithography process involves the simultaneous fabrication of a large number of devices, depending on the size of the mask. The devices are typically organized in the form of delay lines, which is a pair of devices separated by a well-defined distance. This configuration is important for the characterization of the individual devices besides being a platform for SAW-based filters [116, 120].

We have processed IDTs on $Y-128^\circ$ LiNbO_3 substrates by photolithography at the Centro de Componentes Semicondutores (CCS*Nano* - UNICAMP). We used a positive photoresist (AZ 5206) and a Karl Suss mask-aligner (Karl Suss MJB3 with

a $\lambda = 400\text{nm}$ lamp). The used mask was manufactured at Centro de Tecnologia Integrada Renato Archer (CTI - Campinas - SP) and was designed to fabricate 48 devices simultaneously in the configurations of single and double-finger to generate SAWs with wavelengths of $8\ \mu\text{m}$ and $16\ \mu\text{m}$, respectively. In the mask, L_f is defined as $2\ \mu\text{m}$. The devices are designed with an aperture W_A of $400\ \mu\text{m}$, and a number of 80 periods. The photolithography process was carried on pre-cleaned LiNbO_3 (acetone and isopropanol at 160°C during 4min each). The process was conducted as follows: we applied the HDMS adhesion promoter with the aid of spinner at 5000RPM during 30s, in sequence we applied the photoresist at 5000RPM during 30s. The sample was then submitted to a pre-bake at 90°C during 1min, followed by a UV flood exposure during 0,5s with the mask-aligner. The sample was then submitted to a second bake at 110°C during 45s. After the second bake, We aligned the mask and submitted the sample to a exposure of 10s. Finally, we conducted the development with the MIF300 developer for 10s. Before the metalization, we cleaned the processed surface with O_2 plasma with a power of 100W, pressure of 200mTorr and O_2 flux of 50sccm (standart cubic centimeter per minute), during 4min. We then metalized the surface with 10nm of Ti and 60nm of Al in an e-beam evaporator. Metalization and lift-off were carried in the Laboratório de Pesquisas em Dispositivos (LPD) of the Departamento de Física Aplicada at IFGW-UNICAMP.

We started the fabrication by adapting the parameters used on Si substrates to LiNbO_3 . During this step we tested the influences of the lithography parameters (application of photoresist, exposure to UV light and development time) and different processes for cleaning the substrates and, in the end, we achieved a recipe that results in functional devices despite some difficulties in the lift-off process, which resulted in some devices short-circuiting and fractures in the structures, compromising their functioning.

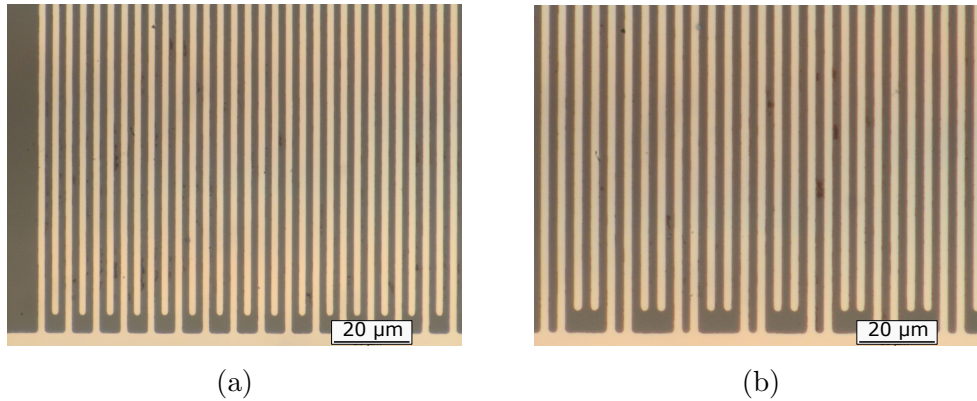


Figure 4.3: Micrographs of a single-finger (a) and a double-finger (b) IDT fabricated on Y-128° LiNbO₃ substrate.

Figure 4.3 shows optical microscopy images of a resulting single-finger (4.3.a) and a double-finger (4.3.b) IDTs, illustrating part of the resulting devices that are functional. This process, although functional, is not fully optimized. The manufacturing homogeneity can still be improved as our process results in an efficiency of approximately 50% of functional devices. The characterization of the functional devices will be discussed in next sessions.

4.1.3 Electrical characterization - Scattering parameters

In general, the characterization of SAW devices is made by means of RF electrical reflection and transmission spectroscopy. From these measurements it is possible to extract the reflection and transmission coefficients - the scattering parameters - of each device. In the IDT case, a simple treatment [120,136] allows the obtaining of the output power (P_{SAW}) of the generated SAW and the electromechanical coupling constant (k^2) from the measurement of the scattering parameters.

The RF measurements were performed with the aid of a probe-station, which allows the realization of electrical contact of the devices with a vector network analyzer through contact probes. The network analyzer is an instrument that allows the simultaneous application and reading of amplitude and phase of the reflected and transmitted signal through the device. We use the experimental setup shown in Figure 4.4. In this configuration, each port of the network analyzer is connected

to one IDT.

The RF reflection measurement consists of applying and measuring the signal in the same port. Reading the reflected signal gives the reflection coefficient, which is represented as S_{jj} since the signal is applied and measured at the port j ($j = 1, 2$). The RF transmission measurement on the other hand consists of applying a signal through a port j and reading it through the other port (i), as shown in Figure 4.4, resulting in the transmission coefficient, which is represented as S_{ij} ($j \neq i$). When the signal is applied to IDT A through port 1, it generates SAW beams in both directions. The beam on the right propagates until IDT B, where it will excite an electrical signal that will be measured at port 2 of the network analyzer. In addition, another SAW beam is induced to the right of IDT B due the fact that a bidirectional IDT is a three-port device [120].

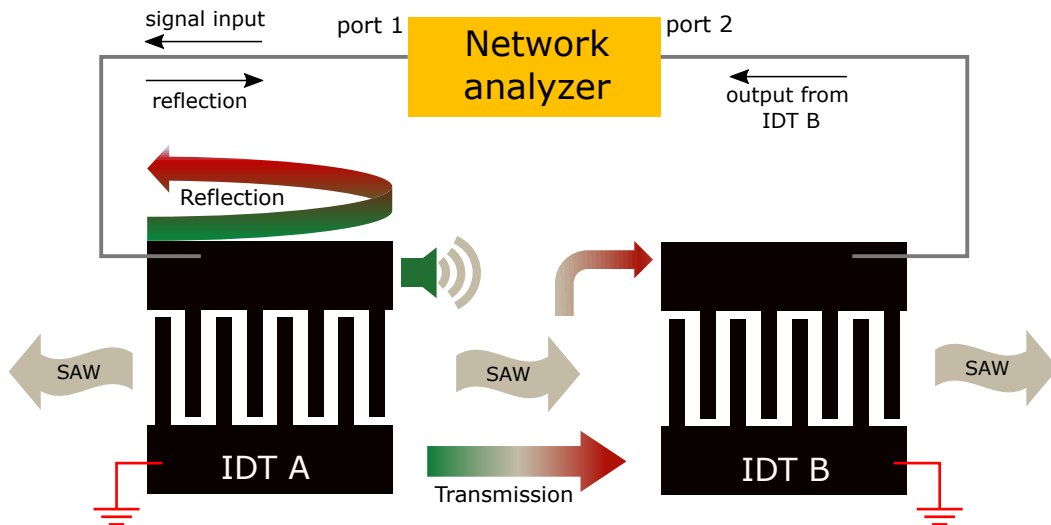


Figure 4.4: Representation of RF electrical reflection and transmission measurements. The electrical input signal is applied (green) through port 1 on IDT A. Part of the signal is reflected (red) and read at port 1. Part of the signal is converted into SAW (beige arrows and green speaker), which propagates through the substrate until it reaches IDT B and induces an electrical signal (output from IDT B) that can be read at port 2.

Figure 4.5 shows the reflection (orange) and transmission (green) coefficient spectra of IDTs A(4.5.a) and B(4.5.b) of a single finger delay line and IDTs A and B of a double-finger delay line in 4.5.c and 4.5.d, respectively.

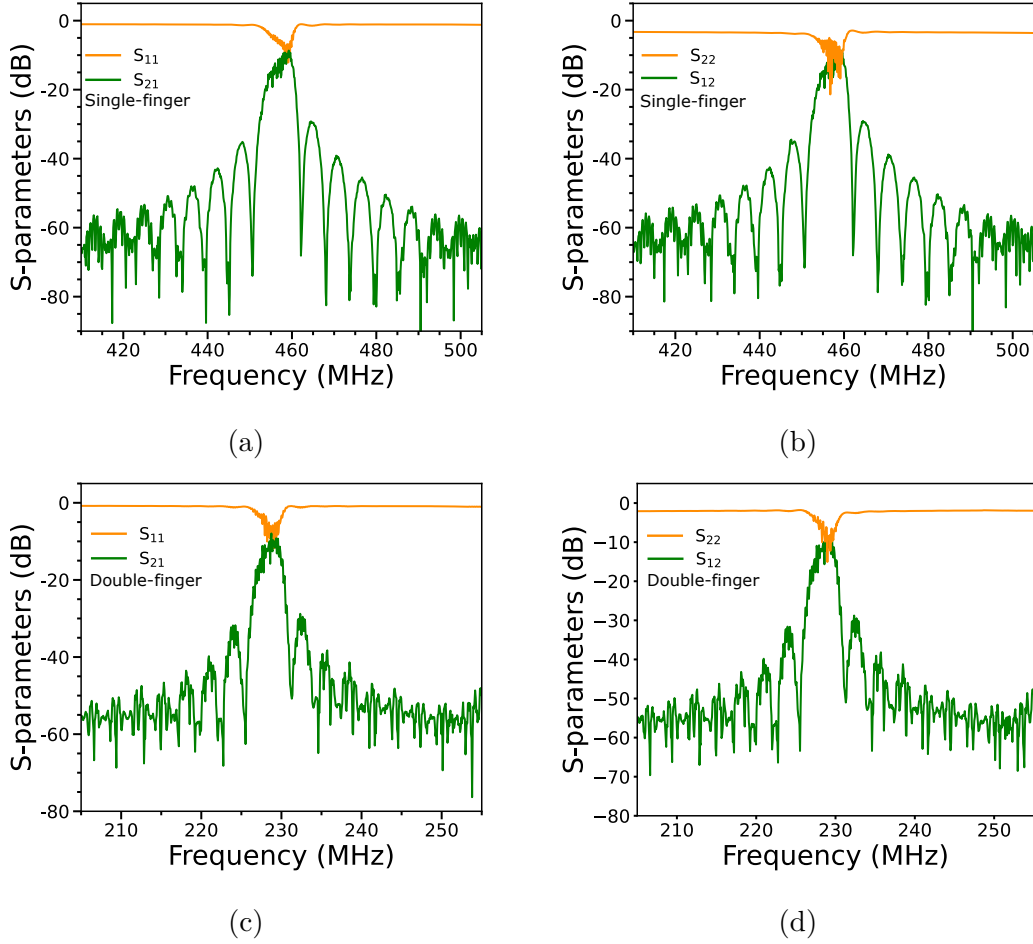


Figure 4.5: Measured Rf reflection (orange) and transmission (green) coefficient spectra of a single-finger delay line in (a) and (b) and a double-finger delay line in (c) and (d), respectively.

The S_{ii} spectra is expected to exhibit a dip centered at the device resonant frequency, indicating that the electrical signal has been converted to SAW. The depth of dip measures the output power of the SAW. By denoting the values of the reflection coefficient at the resonance frequency as S_{jj}^{res} and outside of the resonance as S_{jj}^{out} , the output power P_{SAW} is obtained in terms of an input RF power P_0 as:

$$\frac{P_{SAW}}{P_0} = \frac{1}{2} \left\{ 10^{\frac{S_{jj}^{out}}{10}} - 10^{\frac{S_{jj}^{res}}{10}} \right\}, \quad (4.1)$$

where the factor 1/2 is due to the fact the IDT launches two symmetric beams.

On the other hand the S_{ij} spectrum has a maximum centered on the resonance frequency and an oscillatory behavior around it, with lower values which tends to a

base value far from the resonance frequency. Denoting the values of the transmission coefficient at the resonance frequency as S_{ij}^{res} and away from the resonance as S_{ij}^{out} , the power of the output from IDT B (P_{ind}) will be obtained in terms of the power of P_{SAW} :

$$\frac{P_{ind}}{P_{SAW}} = \frac{1}{2} \left\{ 10^{\frac{S_{ij}^{out}}{10}} - 10^{\frac{S_{ij}^{res}}{10}} \right\}. \quad (4.2)$$

Once again, the 1/2 factor is due to the fact that the input signal is divided equally between the electrical signal and another beam of SAW, generated on the right side of IDT B.

The resonance frequencies of our devices are centered at 456 MHz and 228 MHz for the single-finger and double-finger, respectively. The spectra from Figure 4.5 were used to calculate P_{SAW} and P_{ind} with equations 4.1 and 4.2, respectively. The obtained values are shown in Table 4.1. The data indicates that the devices are capable of generating SAW with an output power of 25% of the input RF power. This power is divided equally between the two SAW beams emitted by the IDT so each SAW beam carries about 12.5% of the input power.

4.1.4 Extraction of acoustic parameters

Figure 4.6 illustrates the equivalent circuit of an IDT [120, 136]. The total impedance of this circuit is given by:

$$Z = R_P + Z_A, \quad (4.3)$$

where R_P is a parasite resistance and Z_A is the acoustic impedance.

The circuit consists of a capacitive term C_T , associated to the geometry of the devices, and two acoustic terms: an acoustic conductance $G_A(\omega)$, related to the electro-acoustic conversion and an acoustic susceptance $B_A(\omega)$, related to losses. In this picture, ω is the angular frequency, which is connected to the RF signal frequency (f) by the relation $\omega = 2\pi f$. The acoustic admittance of this circuit, defined as $Y_A(\omega) = \frac{1}{Z_A(\omega)}$, will be given by:

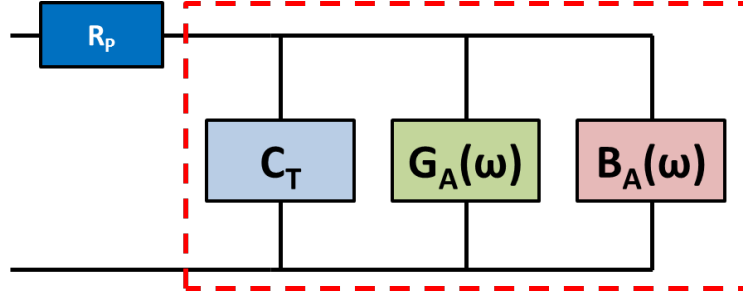


Figure 4.6: Bidirectional IDT equivalent circuit. Adapted from [120].

$$Y_A(\omega) = G_A(\omega) + i \{ \omega C_T + B_A(\omega) \}. \quad (4.4)$$

It is possible to associate the equivalent circuit parameters to the devices RF reflection measurements by converting the reflection coefficient to a total output impedance as [136]:

$$Z = Z_0 \left\{ \frac{1 + S_{jj}}{1 - S_{jj}} \right\}, \quad (4.5)$$

where Z_0 is the characteristic impedance of the transmission line which, in the case of our measurement, is 50Ω .

With the total impedance we can, using the equation 4.3, find the value of the parasitic resistance, which appears as an offset in the $\text{Re}(Z)$ spectrum. Subtracting this value, we have the spectrum of Z_A and therefore $Y_A(\omega)$. $\text{Re}(Y_A(\omega))$ gives us $G_A(\omega)$.

The frequency dispersion of the acoustic conductance of a given device is a function of its geometrical parameters (W_A , N_P and L_f) and the piezoelectric properties of the material. Moreover, it represents the balance between the mechanical energy generated and the dissipated electrical energy [120]. Assuming that the generated SAW beams propagate in an infinite medium [137], an impulse response model [120] states the form of $G_A(f)$ in the vicinity of the resonance frequency f_0 as [116, 120, 136, 137]:

$$G_A(f) = G_0 \left\{ \frac{\text{sen}(\chi(f))}{\chi(f)} \right\}^2, \quad (4.6)$$

with:

$$\begin{cases} \chi(f) = N\pi \left\{ \frac{f - f_0}{f_0} \right\}, \\ G_0 = 8k^2 f_0 N_P W_A C_T, \end{cases} \quad (4.7)$$

where G_0 is the acoustic conductance at the resonant frequency, N is the number of periods of the device, C_T is the total capacitance and k^2 is the electro-acoustic coupling coefficient. The value of G_0 is determined by a fitting of equation 4.6.

$\text{Im}(Y_A(\omega))$ is given by:

$$\text{Im}(Y_A(\omega)) = \omega C_T + B_A(\omega), \quad (4.8)$$

which allows the determination of C_T with a linear fitting.

We applied the described modeling to extract the electrical and acoustic quantities of our devices. Figure 4.7 illustrates the experimental curves of the acoustic conductance of a single-finger and a double finger IDTs (the same as 4.5.a and 4.5.b, respectively), given in terms of the input RF frequency, and the non-linear fitting with the proposed model. With this treatment we extract the values of parasite resistance (R_P), the total capacitance (C_T), resonance acoustic conductance (G_0). These values are presented in Table 4.1.

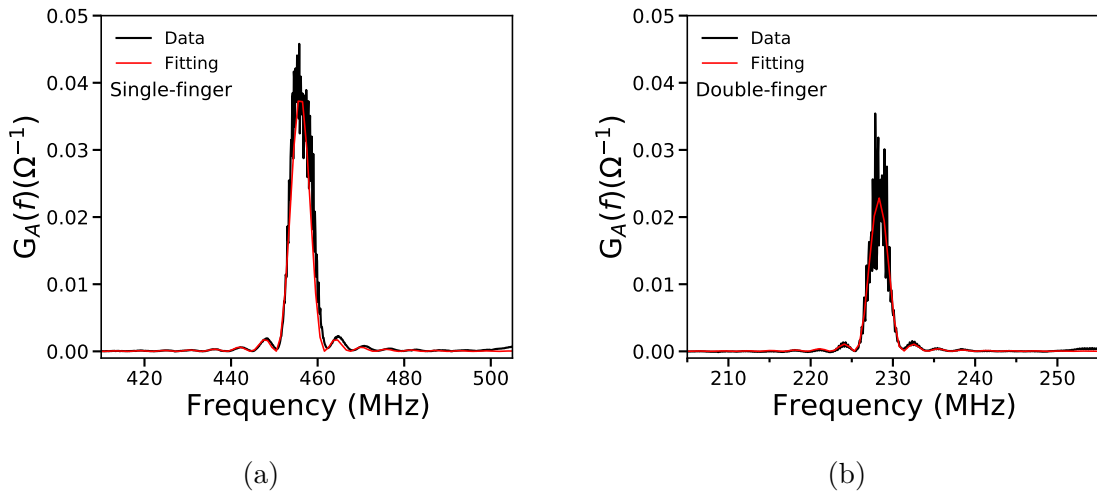


Figure 4.7: Acoustic conductance spectra (black) of single-finger (a) and double-finger (b) IDTs. The red curve is the fitting with the proposed model. The curves are obtained from the experimental data shown in Figure 4.5.

Table 4.1: Electric and acoustic parameters of the IDTs extracted from the electric characterization measurements.

		$\frac{P_{SAW}}{P_0}$	$\frac{P_{ind}}{P_0}$	$R_P(\Omega)$	$C_T(pF)$	$G_0(\Omega^{-1})$
Single Finger	SF1	0,29	0,10	3,76	15,60	0,04
	SF2	0,18	0,08	11,80	15,07	0,04
Double Finger	DF1	0,33	0,07	3,65	21,30	0,02
	DF2	0,24	0,06	6,82	19,30	0,02

The obtained values of the C_T and G_0 are in comparable to values reported in literature for similar devices [120]. It is also worth mentioning that the proposed model to adjust the acoustic conductance does not take into account internal reflections in the devices, which is valid only for the double-finger IDT where internal reflections are suppressed. Moreover, the used model considers an infinite array of point sources, which is different from our finite device. However, we point that our experimental data is fairly fitted by the model given by Equation 4.6, although the electro-acoustic conversion is not ideal due to losses.

4.1.5 Unidirectional transducers

When under a RF input, bidirectional IDTs launch two equal SAW beams, each one carrying half of the generated acoustic power (P_{SAW}). Moreover, even with the use of double-finger IDTs, the effects of triple-transit are present. This fact in itself represents a disadvantage of bidirectional IDTs, since it entails a minimum inherent loss of 6dB [138] of generated energy. Unidirectional transducers (UDTs) can partially solve this problem by launching SAW beams with very different amplitudes to each side [116, 120, 138]. A device with high directionality can be understood as a two-port device: one acoustic and one electric, which reduces the multiple transit effects and the power losses. Moreover, SAW beams with higher acoustic power and, consequently, higher amplitudes of strain and piezoelectric field are usually obtained with UDTs.

Over time, there were several attempts to achieve unidirectionality, including the use of reflectors on one side of the device to favour the other beam and the use of phase-shifted voltages into splitted elements [120]. A wide variety of devices were constructed with these ideas, what eventually led to the construction of the floating-electrode unidirectional transducers (FEUDTs). Such devices are constructed with the presence of floating fingers —i.e. electrodes which are disconnected from the busbars, that act as reflectors within the device period. The floating fingers are usually placed at a distance below $\lambda_{SAW}/4$ from the active fingers, thus breaking the symmetry of the system unit cell. Since the floating fingers exhibit a larger acoustic impedance than the free space [138], the SAW emission in one direction is favoured over the other. Moreover, such devices operate in a single phase [120, 138], being also referred to as single-phase unidirectional transducers (SPUDTs). They can reach up to 99.4 % of directionality [139], as recently reported for UDTs operating at a frequency of 2.3 GHz and a temperature of 10 mK.

Figure 4.8 illustrates the FEUDT device which we used in our experiments. The devices were fabricated in the Paul-Drude-Institute für Festkörperelektronik (Berlin-GE) and kindly provided by Paulo V. Santos. The finger widths of 12 μm and 6 μm together with a finger spacing of 1 μm result in a wavelength of 35 μm . We used devices with aperture values of $W_A = 212 \mu\text{m}$ and $W_A = 424 \mu\text{m}$. The period is framed within the red rectangle. Such configuration results in a directionality of $\approx 97\%$, as obtained from interferometry measurements performed in Berlin (not included in this thesis). The delay lines were lithographically defined along the in-plane X direction of black Y-128° LiNbO₃ substrates. All FEUDTs were fabricated with $N_p = 20$ finger pairs. The devices have two lower acoustic resonances at approximately 112 and 222 MHz. In the experiments presented in this thesis, the MoSe₂ ML was probed with a SAW at 222 MHz and the MoS₂ ML at 112 MHz.

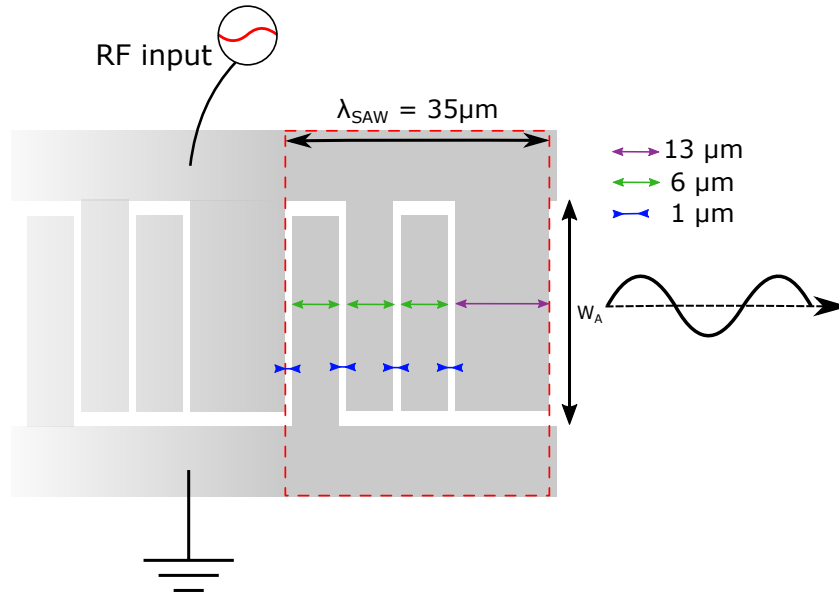


Figure 4.8: Illustration of the FEUDT transducer that was used in the modulation experiments. The RF input excites a single SAW beam to the right of the device (in the case of the illustration). Values of finger widths are indicated. The finger spacing is $1 \mu\text{m}$ so $\lambda_{SAW} = 35 \mu\text{m}$. We used devices with aperture values of $212 \mu\text{m}$ and $424 \mu\text{m}$.

4.2 Acoustic modulation experiments

4.2.1 Optical spectroscopy setup

The optical spectroscopy setup was planned, assembled, and tested during the experiments reported in this thesis. An illustration of the setup is shown in Figure 4.9. It has two solid state lasers ($\lambda = 532\text{nm}$ and $\lambda = 457\text{nm}$) that can be selected using a flip mirror. The light beam passes a linear polarizer and a beam splitter directs it to a quarter waveplate, where it becomes circularly polarized. The beam is focused at the sample inside the cryostat using an objective lens whose focus (z axis) is controlled by a piezoelectric actuator. The emitted PL is collected using the same objective lens and passes the quarter waveplate again, becoming linearly polarized. After passing the beam splitter, the beam encounters a polarization beam displacer, which spatially separates the orthogonal linear components of the light into the beams PL_S (s component) and PL_P (p component). Both beams

are directed to the monochromator (HoribaTM iHR 550, with diffraction gratings of 600 grooves/mm and 1200 grooves/mm) and are detected in different areas of the detector (HoribaTM Symphony-II CCD camera), allowing for the simultaneous acquisition of both orthogonal linear components, which diminishes the instrumental uncertainties besides making the process more efficient and accurate. The setup is also equipped with a RF generator (Rohde & SchwarzTM SMB100A microwave signal generator) and a vector network analyzer (Rohde & SchwarzTM ZVL13 vector network analyzer), which are used to generate SAWs and characterize SAW-generating devices inside the cryostat, respectively even at low temperature. Finally, the cryostat (4-325K cold finger CryovacTM Konti cryostat) has a piezoelectric stage system (MechonicsTM CU30CL) for sample positioning which allows the automatic control of the position of the sample and the obtaining of PL hyperspectral maps. The control of the setup is made with the use of LabViewTM programs that integrate all the equipment for the measurements. A computer is used for both control and data acquisition. Figure 4.9 was constructed using the ComponentLibrary by Alexander Franzen.

4.2.2 Optical spectroscopy measurements

Figure 4.10 illustrates the ML sample and the SAW-generating device inside the cryostat. It is a representation of the inside of the cryostat, thus it is part of the experimental setup shown in Figure 4.9. The TMD MLs are placed on the Y-128° LiNbO₃ substrate in front of a FEUDT device, which launches a propagating acoustic beam along the x direction when under an electrical RF input. An objective lens (as shown in Figure 4.9) focuses an continuous wave (CW) laser beam (in blue) on the ML, which allows for both optical excitation and acquisition of the PL emitted by the sample.

Laser power, SAW power, and temperature are controllable variables in our experiments. The laser power is controlled with the aid of neutral density optical filters, which reduce the intensity of the beam and allow for fine tuning the incident power on the sample. The control of the acoustic power, is directly made with the RF

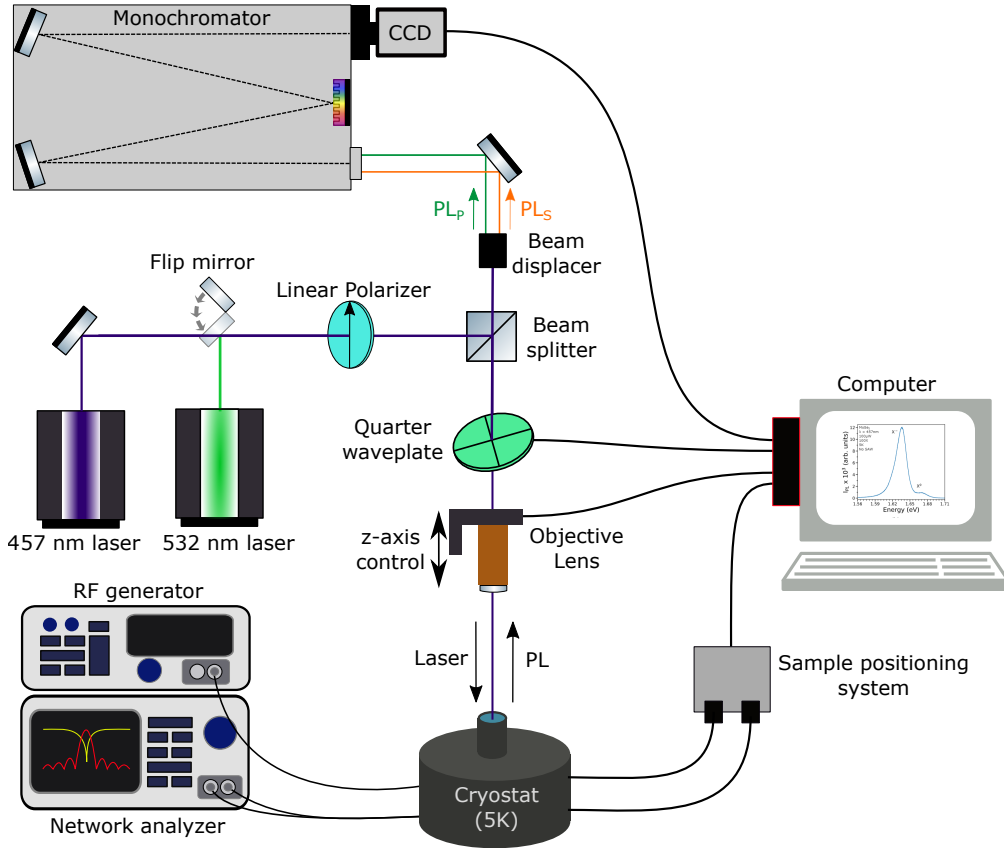


Figure 4.9: Experimental setup for μ PL spectroscopy measurements. Linearly polarized laser ($\lambda = 457\text{nm}$ or $\lambda = 532\text{nm}$), selected using a flip mirror, becomes circularly polarized after passing a quarter waveplate; an objective focuses the beam on the sample inside the cold finger cryostat; the emitted PL is collected by the same objective. Before entering the monochromator, the p (PL_P) and s (PL_S) components are separated by a polarization displacement prism and simultaneously detected in different areas of a CCD camera. SAW is generated on the sample using a RF generator. Network analyzer is used to characterize the SAW generating devices. The cryostat also has a positioning system which is used to move the sample and allows the PL mapping. The setup is controlled by a computer. Representation of the setup was constructed using the ComponentLibrary by Alexander Franzen.

generator, allowing for the control of the amplitudes of the strain and piezoelectric fields carried by the SAW. As discussed in Chapter 3, different amplitudes of the fields are expected to lead to different amplitudes of the energy modulation and higher is the exciton dissociation rate to be observed. The acoustic power is the

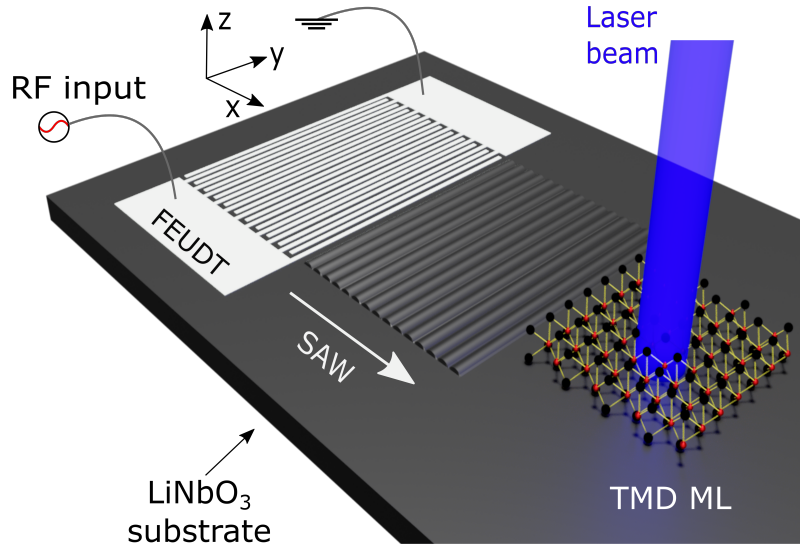


Figure 4.10: Device illustration: the SAW beam is launched along the x direction by a FEUDT towards the TMD ML, where PL is excited by a focused laser beam and collected by an optical objective (not shown).

main parameter of our experiments, and the relation between the RF input power and the resulting amplitude of the SAW fields is established in Chapter 5. Finally, temperature can be controlled inside the cryostat by means of control of the He flux.

We conducted μ PL experiments on MoS_2 and MoSe_2 MLs under the application of propagating SAW beams, as shown in Figure 4.10. The experiments were performed in three different series: (i) PL measurements with fixed laser power and temperature, but with increasing SAW power; (ii) fixed SAW power and temperature, but increasing the excitation power; and (iii) fixed laser and SAW power with different temperatures. We also monitored our acoustic modulation experiments as a function of time, where the PL spectra were collected at a rate of 10s, while the SAW beam is turned on and off at given moments. This allowed us to observe the SAW-driven dynamics of the PL signal as well as the system recovering from the incidence of the acoustic beam.

As a final remark, despite the fact that Figure 4.9 shows the optical polarization apparatus (linear polarizer, quarter waveplate and beam displacer), all the experiments presented in this thesis were carried without polarization resolution.

4.2.3 The samples

The TMD MLs were obtained by dry micromechanical exfoliation from bulk 2H crystals from HQ graphene onto Nitto-tape [2]. A second exfoliation was performed on a polydimethylsiloxane (PDMS) stamp placed on a glass slide. Bright field and fluorescence images were carried out using an Olympus BX51 fluorescence microscope at ambient conditions to identify the MLs. Using a micromanipulator, MoSe₂ and MoS₂ flakes were transferred and placed close to the output port of FEUDTs with apertures of 212 μm and 424 μm , respectively, onto the LiNbO₃ substrates, being positioned in the middle of the SAW path as shown in Figure 4.11. The ML samples were prepared in the Departamento de Física - Universidade Federal de Minas Gerais (Belo Horizonte - BR) by Dr. Bárbara L. T. Rosa.

Figure 4.11.a and 4.11.b show micrographs (5X magnification) of the exfoliated MoS₂ and MoSe₂ MLs, respectively, and the SAW generating device used with each one. Due to the low magnification, the ML is not visible but the approximate positions are indicated by the black arrows.

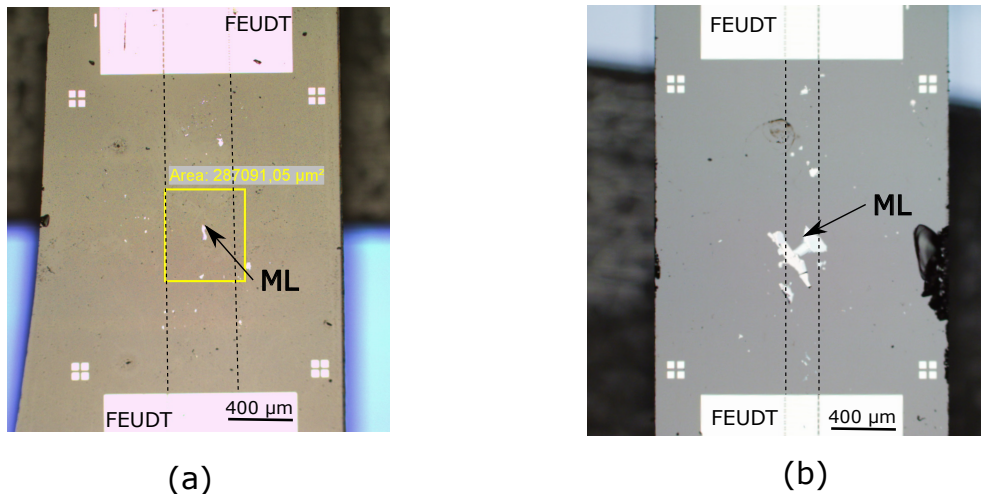


Figure 4.11: Optical micrographs of the MoS₂ (a) and MoSe₂ (b) MLs, respectively, and the SAW generating device used with each one, taken with 5X magnification. The approximate position of the MLs are indicated by the black arrows. (c) Representation of a ML positioned in front of the FEUDT output indicating that it lies on the acoustic path.

CHAPTER 5

Computational methods

The SAW piezoelectric and strain fields experienced by the MLs were calculated using the finite element method (FEM) using the COMSOL Multiphysics platform. By taking into account the FEUDT design and the LiNbO_3 substrate mechanical and piezoelectric constants, we were able to simulate the radio frequency scattering (S_{11}) parameter measurements of our devices. From the nominal power applied to each FEUDT in the experiments, we calculate the amplitude of the SAW strain and piezoelectric field at the surface where the MLs sit. The latter allowed us to compare the experiments performed on the MoSe_2 and MoS_2 MLs placed on different FEUDT devices.

5.1 Simulation model

Figure 5.1 shows an illustration of the model used for the calculations. Figure 5.1.a shows a 3D representation of the system where a FEUDT device is used to generate SAWs in the \hat{x}_1 direction on a $Y\text{-}128^\circ$ LiNbO_3 substrate. An RF electrical input V_{RF} (highlighted in red) is applied to one side of the device, while the other side is grounded (highlighted in blue). The FEUDT device also exhibits floating electrodes within each period, as defined in section 4.1.5 (highlighted in green). It shows a 2D cut (highlighted in yellow) representing a unit cell of the device which is employed to construct the 2D model.

Figure 5.1.b shows the 2D model developed for the calculations, where we

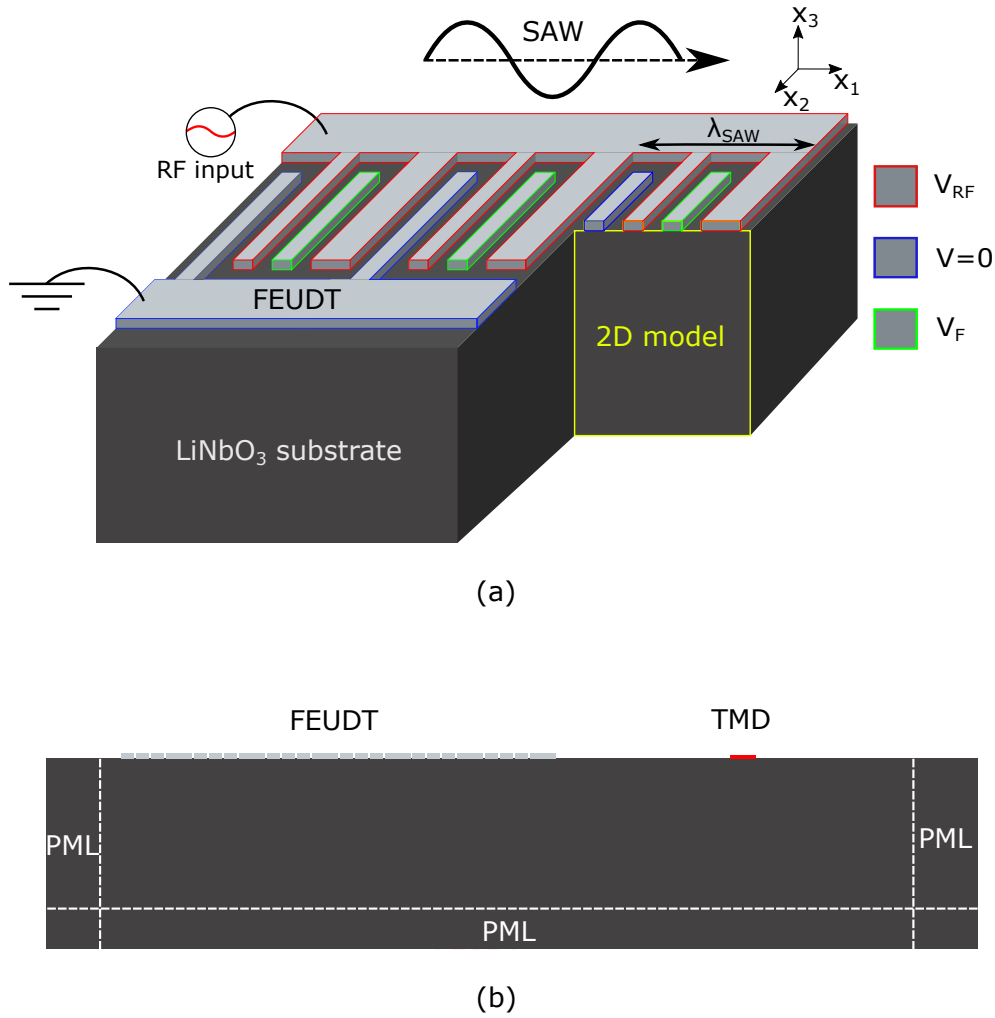


Figure 5.1: Representation of the model used for the numerical calculations. (a) Three-dimensional representation of the SAW-generating FEUDT device on the LiNbO_3 substrate with a cut of the 2D model. The electric potential is highlighted in each finger of the device where the RF potential (V_{RF}), ground and floating potential ($V=0$) are represented in red, blue and green respectively. The 2D cut shows a single period of the model employed on the calculations. (b) Representation of the complete 2D model with the device fingers and the TMD ML (in red). The electric boundary conditions are the same of (a) but we point the presence of the PML. Elements are not in scale.

include the FEUDT device and the TMD ML. In particular, the simulations of SAW generation can be fully described in two-dimensional models without loss of generality, which justifies our 2D model presented in Figure 5.1. This method has been successfully employed in SAW generation simulations [123, 140–142]. We added

Perfectly Matched Layers (PML) [143] at the bottom and the sides of the model. The PML inserts a complex component to the displacement vector causing it to be damped alongside with the piezoelectric potential. The bottom PML ensures that the amplitude will be suppressed as the depth increases and thus the solution will be mainly confined around the surface. On the other hand, the PML on the sides ensures that we will be dealing with waves that propagate infinitely and therefore will not be reflected in the region of interest in the model. Moreover, the model is asymmetric so that the TMD ML is far away from the right side PML.

The boundary conditions presented in section 3.2 with Equations 3.30a-d are present. The mechanical variables are included on the model by imposing the condition of zero stress on the surface and zero displacement on the bottom and the sides. The condition of zero stress applies for the top of the FEUDT fingers, the top of the ML, and the free surface.

The FEM calculations are performed through the discretization of the problem into smaller blocks (the finite elements), which are submitted to the boundary conditions. In this way, the discretization into a detailed grid results in a better convergence and more accurate results. Figure 5.2 shows the discretization of our model. In our case, the discretization of the LiNbO_3 substrate was constructed by a mesh of triangular elements while the discretization of the FEUDT fingers, the ML, and the PML were made with a mesh of mapped rectangular elements which connected to the triangular elements of the substrate. In order to guarantee convergence of the model, the element sizes are set to be smaller than $\lambda_{SAW}/8$.

The model takes into account the device design: number of periods $N_P = 20$, SAW wavelenght $\lambda_{SAW} = 35\mu m$, device aperture W_A ($424\mu m$ MoS_2 and $212\mu m$ for MoSe_2), and the eletromechanical coupling constants of the substrate [50, 116, 123] to simulate the RF response of the device by means of the S_{11} parameter. The aperture of the devices is not shown in the bidimensional model, but is inserted in the simulations via an out-of-plane distance. In order to obtain the S_{11} parameter, the simulated impedance (Z) is with the characteristic impedance (Z_0) of the transmission line (50Ω in our case) as follows [136]:

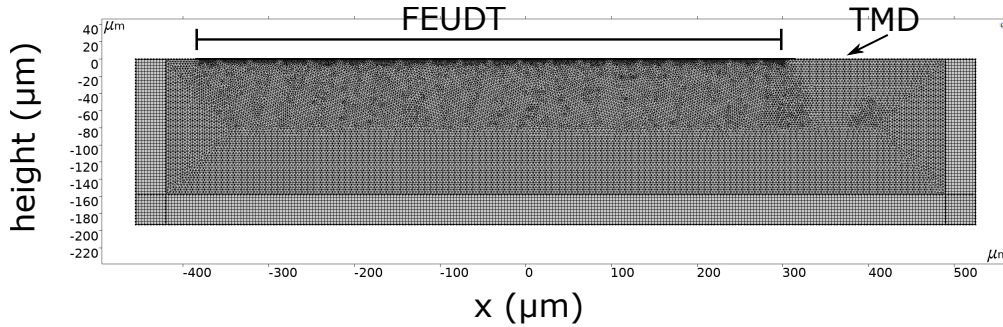


Figure 5.2: Discretization of the 2D model showing the mesh of the substrate, FEUDT fingers and the PML. The TML ML is not visible due to the small thickness.

$$S_{11} = \frac{Z - Z_0}{Z + Z_0}; \quad (5.1)$$

which is the same formulation given in Chapter 4.

5.2 SAW strain field and piezoelectric potential

Figure 5.3 shows the calculated (orange) and experimental (blue) reflection coefficient S_{11} spectra of the FEUDT device of aperture $W_A = 212\mu m$, which was used with the MoSe_2 ML. The spectra reveals three resonances: the fundamental mode at $\approx 110\text{MHz}$ and first and second overtones at 225MHz and 330MHz , respectively. Moreover, measurement and simulations are in very good agreement. The small differences between the measured and calculated resonance frequencies are due to slight differences between the real and simulation-adopted elastic parameters. Moreover, the measurement is affected by a non-perfect calibration (due to the large frequency range), which is the reason for the drift of the S_{11} plateau to lower values as the frequency increases. The amplitude of the resonances dips exhibit a good agreement in measured and simulated spectra. The amplitude is a measurement of the effective launched acoustic power, which allows us to calculate the SAW piezoelectric field and strain, as discussed in Chapter 4.

Figure 5.4.a shows the 2D images of the total SAW particle displacement am-

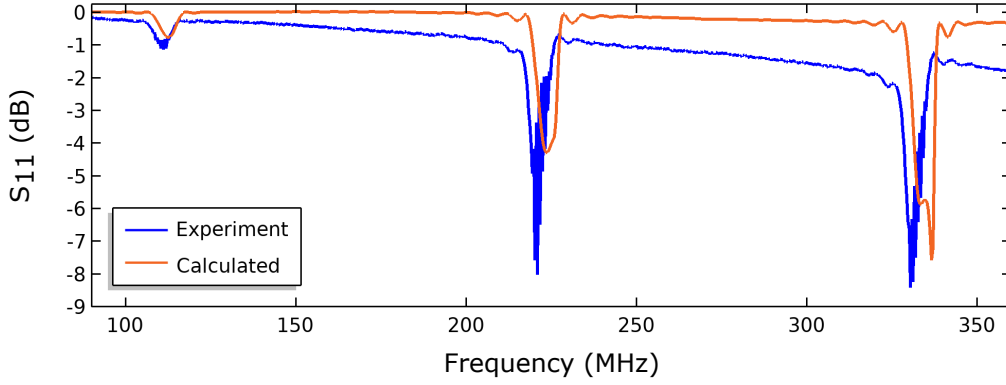


Figure 5.3: Measured (blue solid line) and calculated (orange solid line) S_{11} parameter for the three lower acoustic resonances of the FEUDT device.

plitude ($|\vec{u}| = \sqrt{u_1^2 + u_3^2}$, being u_1 and u_3 the components of the displacement vector along directions x_1 and x_3 , respectively). Figure 5.4.b shows the SAW piezoelectric potential ϕ_{SAW} at the 225MHz resonance frequency simulated for the FEUDT which is used with the MoSe₂ sample. At first, we observe the unidirectional characteristics of the device by noticing that the amplitude of both $|\vec{u}|$ and ϕ_{SAW} are larger on the right side of the FEUDT region, indicating that the acoustic beam is preferentially launched in this direction. The unidirectionality of the FEUDT devices is extremely important in order to achieve larger acoustic powers in comparison to conventional IDTs. The directionality of the device can be calculated using the values of the displacement amplitude on the right side, $a_{forward}$, and on the left side $a_{backward}$. The SAW power is proportional to the square of the amplitude, thus we define the directionality as:

$$D = \frac{a_{forward}^2}{a_{forward}^2 + a_{backward}^2}. \quad (5.2)$$

The simulation results in directionality values of 62.8, 91.3, and 97.8% for the three resonance frequencies, respectively, for the device shown in Figure 5.4. Interferometry experiments, performed in Berlin (not included in this thesis), measure both $a_{forward}$ and $a_{backward}$ amplitudes, allowing the experimental determination of the directionality using equation 5.2. The experimental directionality is measured as 97% at the 330MHz resonance of a similar FEUDT device, in excellent agreement

with the simulation.

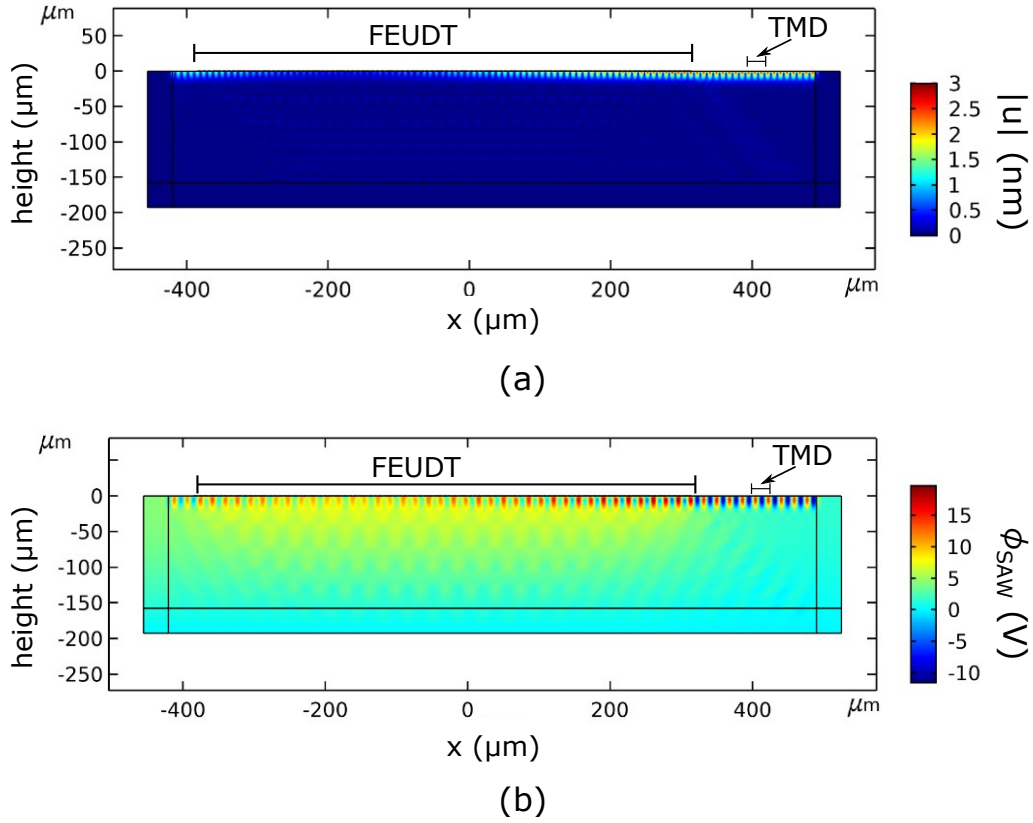


Figure 5.4: Two-dimensional plots of (a) the total particle displacement; and (b) the piezoelectric potential of the SAW simulated for the FEUDT resonance at 225 MHz.

Figures 5.5a and 5.5b show the calculated piezoelectric field components (E_1 and E_3) and the hydrostatic strain ($\frac{\delta V}{V}$), respectively, at the LiNbO_3 substrate and at the 0.6nm MoSe_2 ML around the first FEUDT overtone (225MHz). Figure 5.5a shows E_1 calculated on the LiNbO_3 surface and at the ML in green and blue circles, respectively, while Figure 5.5b shows the hydrostatic strain calculated on the LiNbO_3 and at the ML in red and orange circles, respectively. Both strain and electric fields were calculated with a nominal +26dBm input RF power which is the highest used in the experiments with the MoSe_2 ML sample.

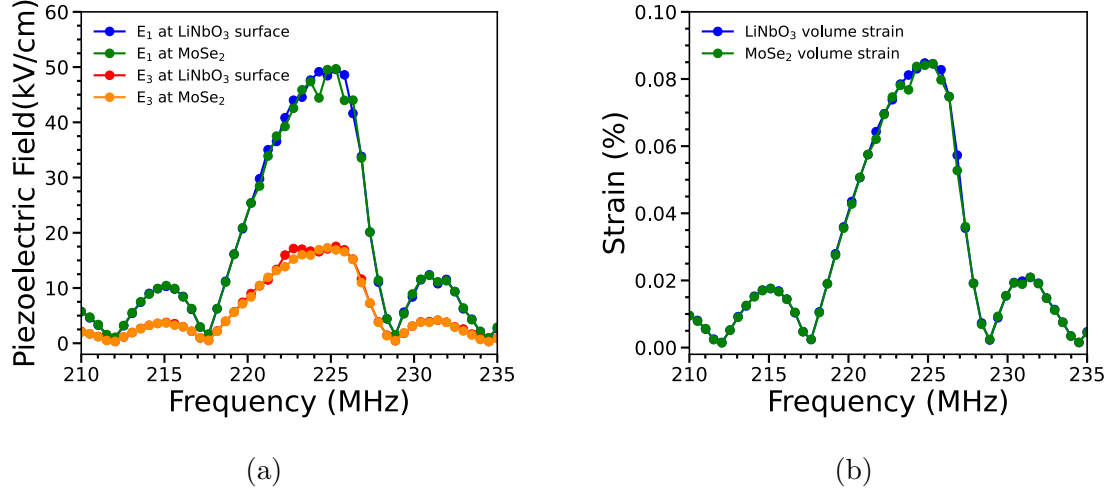


Figure 5.5: Piezoelectric field and hydrostatic strain frequency sweep. (a) Piezoelectric field: in-plane piezoelectric field (E_1) calculated on the LiNbO₃ surface (blue) and at the MoSe₂ ML (green). The out-of-plane piezoelectric field component (E_3) is also calculated on the LiNbO₃ surface (red) and at the MoSe₂ ML (orange). (b) Hydrostatic strain component ($\frac{\delta V}{V}$) at the LiNbO₃ substrate without the ML (blue circles) and at the MoSe₂ ML (green circles).

Figure 5.5a indicates that both E_1 and E_3 are maintained within the ML. Furthermore, at the resonance, the E_1 component is approximately 3 times larger than E_3 . Figure 5.5b shows that the strain field is expected to be entirely transferred from the substrate to the ML as long as the sample follows the oscillatory motion of the substrate. The strain reaches 0.08% at the resonance frequency. Moreover, Figures 5.5a and 5.5b also show small numerical artefacts around the resonance frequency in the calculation of the amplitudes of the strain and E_1 in the ML region. These artefacts are not present in the bare LiNbO₃ surface calculations. They are possibly related to the very small thickness of the as compared to size of the whole model.

Table 5.1 summarizes the amplitude of the E_1 calculated on the TMD ML for the corresponding nominal input RF power (P_{RF}) values, at the 225MHz resonance. For the MoSe₂ sample, we used P_{RF} from +18 dBm to +26dBm at 222MHz (experimental resonance), achieving fields up to 50 kV/cm. On the other hand, we used P_{RF} from +18 dBm to +30dBm at 112MHz for the MoS₂ sample, but achieved lower fields. Moreover, the devices used for each ML are very similar, but the FEUDT

Table 5.1: Calculated amplitude of the SAW in-plane piezoelectric field (E_1) at the sample for each nominal RF input power (P_{RF}) used on the experiments.

P_{RF} (dBm)	E_1 (kV/cm)	
	MoSe ₂	MoS ₂
18	19.5	5.3
20	24	6.7
22	31	8.4
24	39	10.5
26	50	13.3
28	-	16.7
30	-	21.1

used with the MoSe₂ sample has a smaller aperture (212 μm against 424 μm of the one used with the MoS₂ ML), thus exhibits a higher output power for a same applied RF input.

CHAPTER 6

SAW-driven carrier dynamics in MoX₂ monolayers

This chapter brings the experimental results of the SAW experiments carried out on MoS₂ and MoSe₂ MLs on piezoelectric LiNbO₃ substrates. Initially, we show the characterization of the MLs in the absence of a SAW by means of the PL emission. We show, in the sequence, that the SAW piezoelectric field efficiently quenches the PL emission at the laser generation spot due to exciton dissociation and subsequently transports carriers along the SAW propagation path. We also observe a slow dynamics of the PL quenching, where the intensity decays over several minutes until it reaches a reasonably stable value. We investigate the SAW-induced PL quenching as a function of the amplitude of the SAW in-plane electric field, laser excitation power, and temperature of the sample. We show that increasing the piezoelectric field leads to more efficient exciton and carrier manipulation while excitation power and temperature play minor roles on the quenching dynamics. Moreover, we characterize the slow PL quenching dynamics and provide a phenomenological interpretation based on the results of the origins of persistent photoconductivity observed in the process of PL recovery after the SAW is turned off. In addition, we show that the SAW induces the excitonic Stark effect in the monolayers, which allows us to determine the first experimental values of the in-plane exciton and trion polarizabilities of a MoSe₂ ML.

6.1 PL emission in the absence of a SAW

Figure 6.1a shows an optical microscopy image (150X magnification) of the MoSe₂ ML transferred to a LiNbO₃ substrate. The ML is indicated by the yellow arrow. Low temperature (5K) μ PL experiments reveal the presence of two emission peaks centered at 1.635eV and 1.67eV associated, respectively, to negative trion (X^-) and neutral exciton (X^0) emissions [100,144], as shown in Figure 6.1b. These experiments were performed using a 457nm laser at 100 μ W power with 100X objective lens and PL was integrated during 10s.

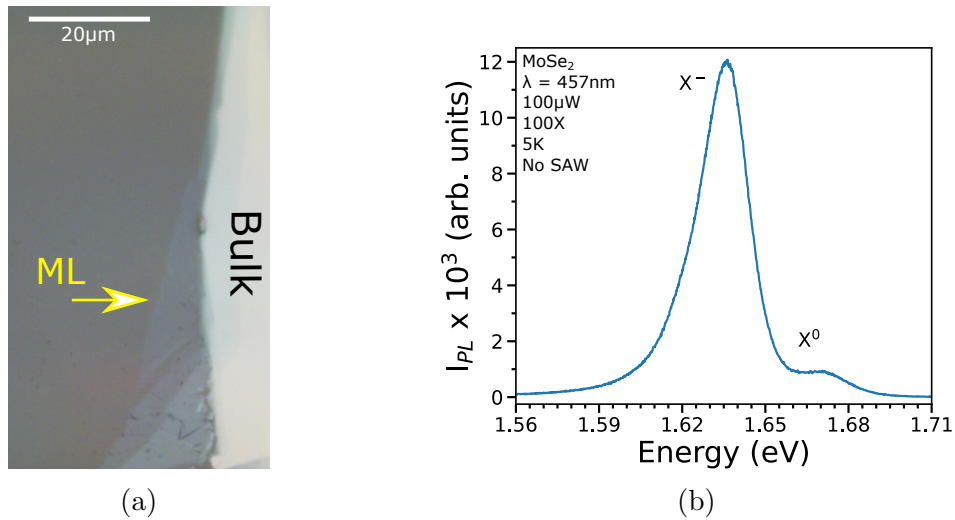


Figure 6.1: (a) Optical microscopy image of the MoSe₂ sample showing the ML. (b) Low-temperature μ PL spectra of the MoSe₂ ML acquired with a 457nm laser at an excitation power of 100 μ W with a 100X objective lens in the absence of a SAW beam.

We observe a small blueshift of approximately 15 meV of the emission lines in comparison to MoSe₂ MLs transferred to SiO₂ substrates [144]. This energy shift is attributed to the net effect of bandgap renormalization due to the strong decrease of the neutral exciton binding energy in the high dielectric constant of the environment provided by the LiNbO₃ substrate [5, 18, 36], as discussed in Chapter 2. Moreover, the mismatch between the thermal expansion coefficients of the MoSe₂ ML and the LiNbO₃ substrate is also expected to blueshift the PL emission [36]. The predominance of the X^- emission is a characteristic of a n-doped ML, which can be related to the substrate [100].

The 35meV of energy separation of between X^- and X^0 emission peaks is attributed to the X^- binding energy which is very similar to the reported values for MoSe₂ MLs on different substrates [100, 103]. As discussed in chapter 2, this is in agreement with recent results which indicate that, in contrast to the neutral exciton, the trion binding energy is much more dependent on the TMD ML constituents than on the surroundings [103].

We also carried out SAW measurements on a MoS₂ ML transferred to a LiNbO₃ substrate. Figure 6.2a shows an optical microscopy image (150X magnification) of the sample, in which the ML region is outlined in yellow to indicate the full extension. Figure 6.2b shows the low temperature μ PL spectra of the ML in the absence of a SAW (blue) and in the presence of a 25dBm SAW beam (orange). All the spectra were acquired using a 457nm laser at 350 μ W power with 100X objective lens and PL was integrated through 10s. The PL spectrum of the ML exhibits two emission bands: one centered in 1.93eV and a wider band centered in 1.77eV. These emission bands are typical signatures of the MoS₂ ML system and are attributed to the excitonic emission (X^0 and X^- complexes) [67] and sub-bandgap defect-related localized states (LS) [145].

We observed that the PL emission of the MoS₂ ML changed over time as we kept performing more measurements, probably due to a degradation process. Figure 6.2c shows the MoS₂ PL spectrum (in the absence of a SAW) after several experiments. The PL was acquired using a 532nm laser at 1mW power with 20X objective lens and PL was integrated through 10s. We point that the spectra of the ML shown in Figures 6.2b and 6.2c were measured under different experimental conditions, which might affect the PL signal. The wider laser spot provided by the 20X objective lens used to acquire the spectrum shown in Figure 6.2c also reduces the PL signal in comparison to the 100X objective lens due to the wider laser spot, which decreases the excitation intensity. However, the PL spectrum shown in Figure 6.2c exhibits an uneven suppression of the individual emission peaks, leading to an inversion of the excitonic and LS intensity ratio. Furthermore, the ML PL signal is also unevenly suppressed in comparison to the background signal.

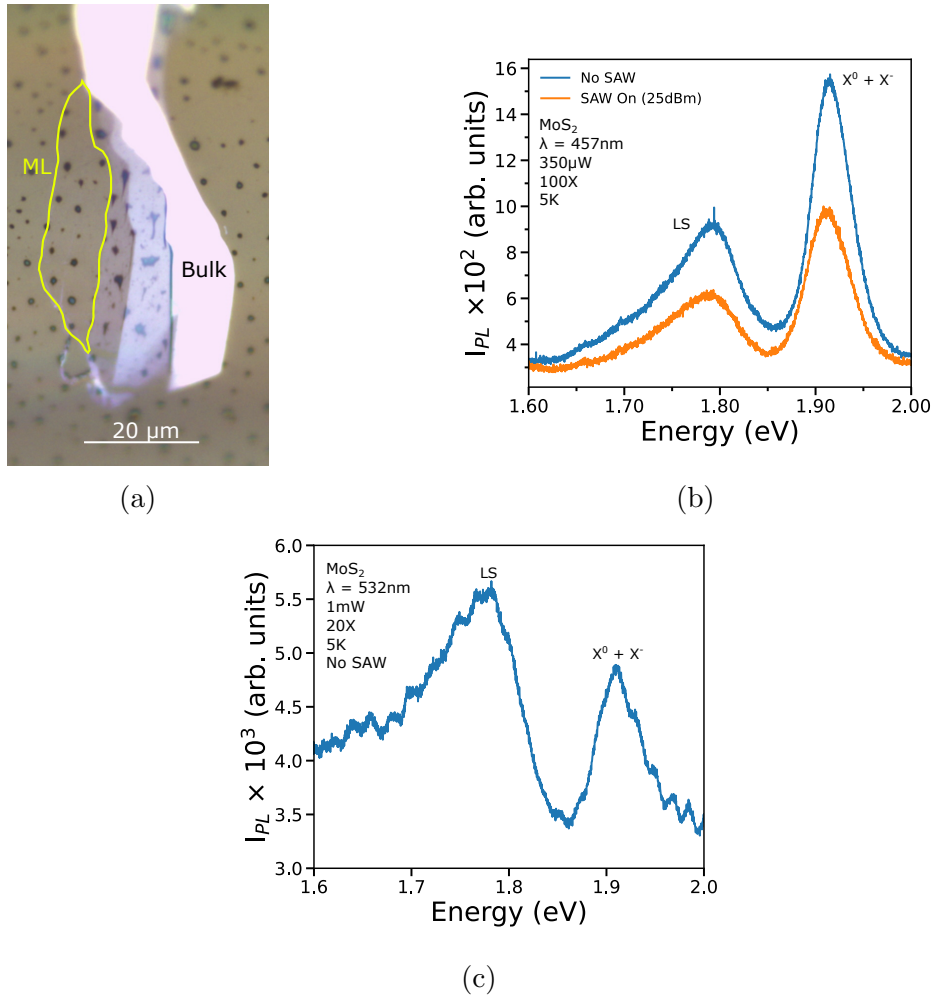


Figure 6.2: (a) Optical microscopy image of the MoS₂ sample, in which the ML is outlined in yellow. (b) Low-temperature μ PL spectra of the MoS₂ acquired with a 457nm laser at an excitation power of $350\mu\text{W}$ with a 100X objective lens in the absence of a SAW beam (blue) and in presence of a 25dBm SAW beam (orange). (c) Low-temperature μ PL spectrum of the MoS₂ after the degradation. Measurement was carried out using a 532nm laser at an excitation power of 1mW with a 20X objective lens in the absence of a SAW beam.

Despite the PL modification caused by the ML degradation, we still have enough intensity to carry out the SAW-modulated experiments. Moreover, the behavior of the ML PL when in presence of a SAW did not change over time and follows the same one observed in Figure 6.2b, so that we carried out all the SAW experiments with the MoS₂ PL as shown in Figure 6.2c.

6.2 Acoustically modulated PL spectroscopy

In order to characterize the effects of the application of propagating SAW beams on MoS₂ and MoSe₂ ML samples, we performed low-temperature continuous wave (CW) μ PL experiments and followed the PL emission at the generation spot in three stages. We start by monitoring the PL signal without a SAW for reference. After that, the SAW beam is turned on at the time t_{ON} and is kept for approximately 15 minutes before it is turned off at the time t_{OFF} . To illustrate, Figure 6.3 shows a μ PL spectral map assembled by sequentially recording MoSe₂ ML spectra as a function of time during the experiment. The horizontal dashed white lines indicate when a SAW with a in-plane electric field $E_1 = 24\text{kV/cm}$ is turned on and off. The white spectrum shows the PL emission before the SAW is turned on. The horizontal dashed orange lines indicate time intervals of ~ 2 minutes in which we averaged the PL spectra before the SAW beam is turned on and off to calculate the degree of PL quenching (Q_{PL}).

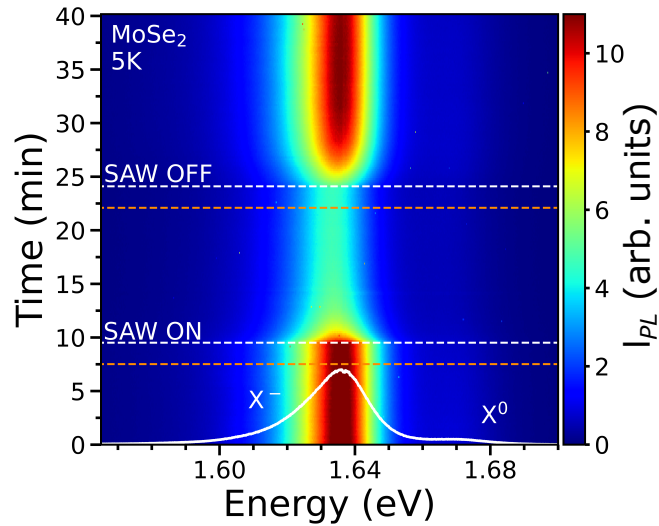


Figure 6.3: Map of the MoSe₂ ML PL emission as a function of time recorded at 5 K with 100 μ W laser excitation. The white horizontal dashed lines indicate when the SAW ($E_1 = 24$ kV/cm) is turned on and off during the experiment. The horizontal orange lines indicate the time window of 2 minutes from where PL is averaged to calculate Q_{PL} . The white spectrum illustrates the PL emission before the SAW is turned on.

We observe in Figure 6.3 that the PL emission immediately begins to be quenched and redshifted once the SAW beam is turned on and recovers the initial state when the beam is turned off. Moreover, we note that the SAW-induced quenching of the PL is not an instantaneous effect as in most common III-V nano-structured semiconductors [51, 130]. In our case, the PL intensity decays progressively through several minutes after the acoustic beam is turned on, before it reaches a reasonably stable level. After the SAW beam is turned off, the PL recovery builds up in the scale of minutes.

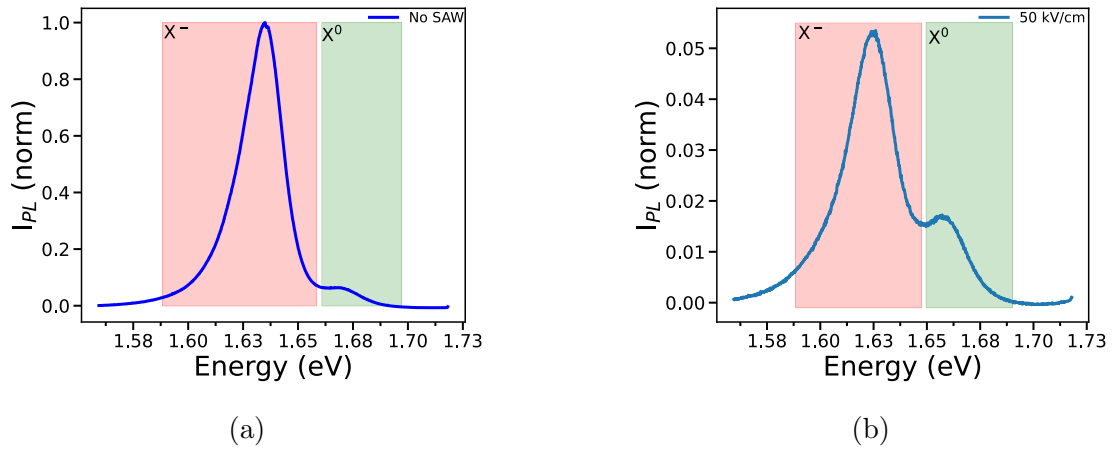


Figure 6.4: Spectral regions used to integrate the individual emission lines of the MoSe₂ ML in the absence of SAW (a), and under the maximum applied SAW power (b). We indicate the X⁰ and X⁻ regions in green and red, respectively.

Several attempts were made in order to fit the PL spectra using Gaussian, Lorentzian or Voigt functions. However, we were not able to construct reliable scripts to fit the data accurately for all measurements which compose the PL maps (like the one shown in Figure 6.3) because of the PL quenching and redshift during the time the maps were measured. As an alternative, we adopted spectral windows for exciton and trion emissions as indicated in Figure 6.4 by the green and red regions, respectively. Figure 6.4a shows the spectral regions used in the absence of SAW, while Figure 6.4b shows the regions used when the maximum SAW power was applied, corresponding to $E_1 = 50\text{kV/cm}$. Since the SAW shifts the PL peaks, the boundaries of the spectral regions are chosen to minimize the overlap between the individual emission lines. As we observe, a considerable contribution ($\sim 50\%$)

to the X⁰ emission comes from the tail of the X⁻ peak, so that the PL quenching of the neutral exciton is slightly underestimated in our analysis due to the faster quenching of the trion emission.

6.3 PL quenching dynamics

Figure 6.5 shows the normalized (and background subtracted) integrated PL profile of the X⁻ emission line of the MoSe₂ ML from Figure 6.3. In order to quantify the dynamics of the SAW-driven PL decay and recovery, we fitted the time transients of the PL intensity with exponential functions, as shown in Figure 6.5. The blue arrow indicates the degree of PL quenching.

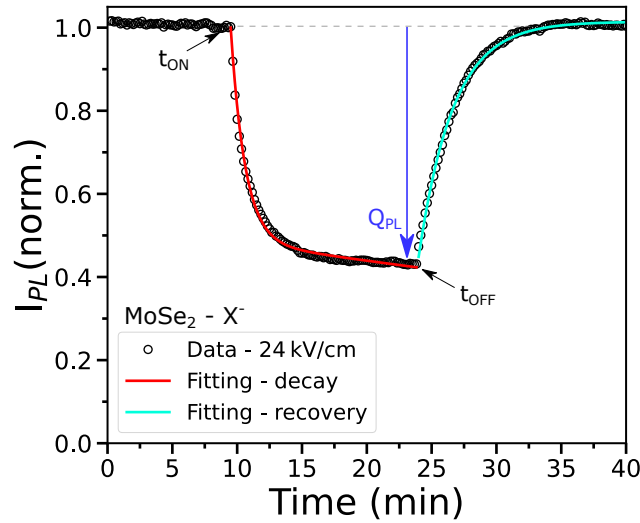


Figure 6.5: Fits of the PL decay (red solid line) and recovery (cyan solid line) transients of the X⁻ emission line when the sample is submitted to a 24 kV/cm in-plane field of the SAW.

The decay behavior of the PL intensity could only be adjusted using an exponential function with two decay constants in the form:

$$I_{PL}(t) = A \exp \left\{ \frac{-(t - t_{ON})}{\tau_{q1}} \right\} + (1 - A) \exp \left\{ \frac{-(t - t_{ON})}{\tau_{q2}} \right\}, \quad (6.1)$$

where τ_{q1} and τ_{q2} time constants are attributed to a fast initial decay and a slow

process, respectively. A is an amplitude parameter for the exponential decay.

As discussed below, the time constants τ_{q1} and τ_{q2} are of different orders of magnitude. Furthermore, $\tau_{q1} \ll (t_{OFF} - t_{ON}) \ll \tau_{q2}$, so that $A = Q_{PL}$. However, Equation 6.1 was used only to determine the decay time constants.

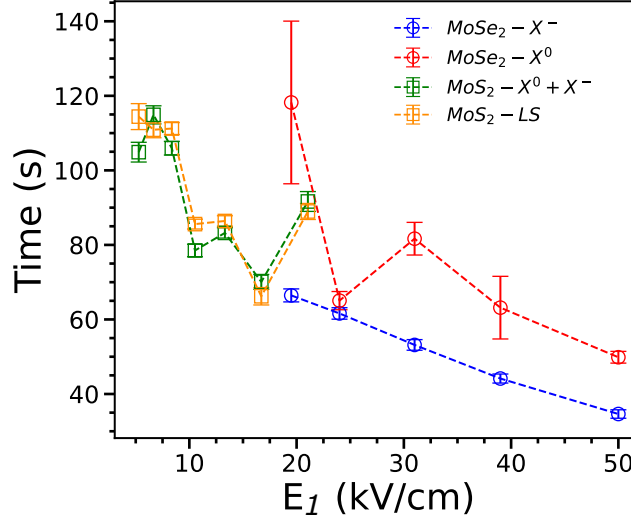


Figure 6.6: Fast PL decay component (τ_{q1}) as a function of SAW E_1 for the X^- (blue circles) and X^0 (red circles) emission lines of the MoSe₂ ML and the $X^0 + X^-$ (green squares) and LS (orange squares) emission bands of the MoS₂ ML.

Figure 6.6 shows the τ_{q1} decay constant as a function of E_1 for X^- (blue circles) and X^0 (red circles) emission lines of the MoSe₂ ML and $X^0 + X^-$ (green squares) and LS (orange squares) emission bands of the MoS₂ ML. A clear decrease trend is observed. The trend suggests that the MoS₂ and MoSe₂ MLs behave in a similar way under similar values of the SAW piezoelectric field. Moreover, for the MoSe₂ ML, the decay of the X_0 emission seems to be slower than the one of X^- , while the values of τ_{q1} obtained for both excitonic and LS emissions of the MoS₂ ML are very similar within the entire range of E_1 .

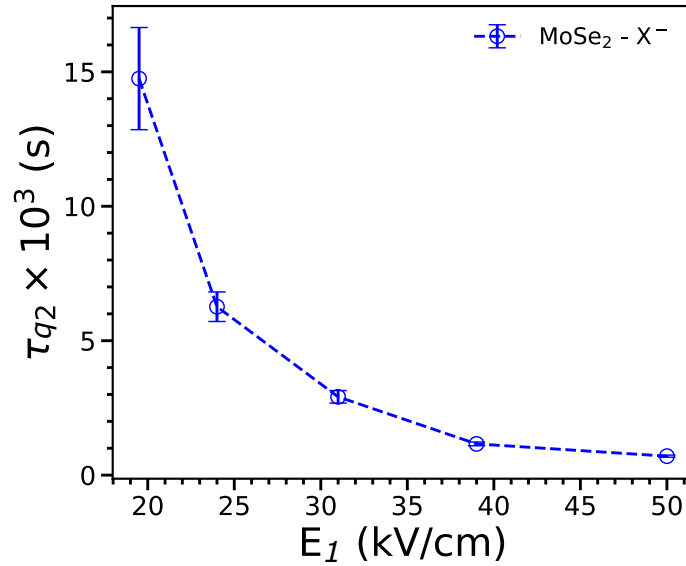


Figure 6.7: Slow PL decay component (τ_{q_2}) as a function of E_1 for the X^- emission of the MoSe₂ ML.

Figure 6.7 shows the values of τ_{q_2} for the X^- emission of the MoSe₂ ML. The time window of 15 minutes that we probed in our experiments under the presence of the SAW beam does not allow us to precisely determine the dependence of the long decay time constant τ_{q_2} on E_1 . However, our double exponential decay fit indicates that τ_{q_2} also decreases with E_1 . For the highest value of E_1 (50 kV/cm) we obtain $\tau_{q_2} \approx 12$ min, which is already comparable to our experimental time window and considerably smaller than the value of $\tau_{q_2} \approx 100$ min obtained for $E_1 = 24$ kV/cm. The X^0 emission of the MoSe₂ ML and both emission lines of the MoS₂ ML exhibit much higher values of τ_{q_2} even at high values of E_1 and are consequently out of our time scale. For this purpose, these constants are not discussed here.

The PL recovery dynamic was also investigated. The cyan solid line in Figure 6.5 is a fit of the experimental data with a build-up transient given by [146]:

$$I_{PL}(t) = 1 - Q_{PL} \exp \left\{ \frac{-(t - t_{OFF})}{\tau_r} \right\}, \quad (6.2)$$

where τ_r is the PL recovery time constant. Equation 6.2 is based on the results of photoconductivity experiments conducted on TMD MLs [35–37, 39], which demonstrate the existence of a slow time transient on the build-up and decrease of the

photocurrent due to persistent photoconductivity (PPC). The PPC is mainly attributed to the presence of defect states that act as traps for electrons and holes, decreasing the radiative decay rate.

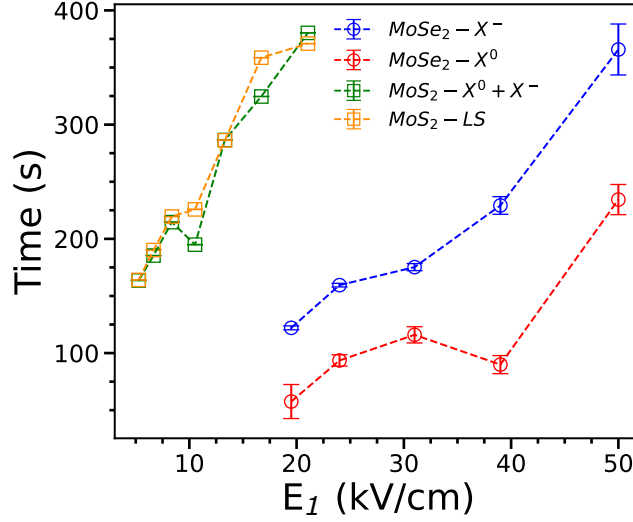


Figure 6.8: PL recovery (τ_r) time as a function of SAW E_1 for X^- (blue circles) and X_0 (red circles) emission lines of the MoSe₂ ML and the $X^0 + X^-$ (green squares) and LS (orange squares) emission bands of the MoS₂ ML.

Figure 6.8 shows the PL recovery time constant τ_r as a function of E_1 . The recovery process takes place in the 100s - 400s time range, being slower than the decay process (τ_{q1}). For MoSe₂, the X^0 recovery seems to be faster than the X^- one and, on the other hand, no big differences between the emission lines of the MoS₂ are observed. Moreover, for both MLs, as E_1 increases, more time is needed to recover the initial PL intensity, but there is no trend solely determined by E_1 , as observed in quenching times presented in Figure 6.6. This indicates that the PL recovery, determined by the PPC dynamics, is sample dependent, as expected.

The obtained values of the time constants reveal slow processes of PL decay and recovery in comparison with the SAW-induced PL quenching observed in III-V quantum well systems [52, 147]. On the other hand, they are in agreement with the results of photoconductivity experiments carried out in TMD MLs [35–37, 39]. In these experiments, slow decrease and build-up of the photocurrent measurement was observed in the presence and the absence of an in-plane field, respectively, which

has been attributed to potential fluctuations along the carrier transport path. In field-effect devices, decay constants between 10 s and 2 minutes (consistent with τ_{q_1}) have been attributed to electron trapping and release process at these potential fluctuations during transport induced by the in-plane piezoelectric field [35, 133]. Recent experiments also indicate that, for non-encapsulated MLs, the local valence band potential fluctuations associated with the strain due to coupling with the substrate are larger than in the conduction band, which makes the electrons more mobile than holes on the TMD plane [132, 133], as represented on Figure 6.9.

The slow decay constant τ_{q_2} can possibly be related to hole drift by the in-plane SAW field. In this way, our results suggest that electrons are drifted away from the laser generation spot at rates associated to τ_{q_1} , in more efficient process than the drift of holes, which takes place at rates associated to τ_{q_2} . This is a consequence of the uneven balance of conduction and valence band potential fluctuations along the carrier transport path [35, 133], as depicted in Figure 6.9. The transport rates for both carriers, however, increase as the in-plane SAW piezoelectric field amplitude is increased, thus indicating that higher acoustic fields or larger mobilities could lead to more efficient acoustic carrier transport in 2D systems.

The presence of two decay constants with different time scales might also arise from a non-uniform distribution of the depth of the potential fluctuations induced by the substrate, as observed in [132]. In this situation, τ_{q_1} relates to shallow fluctuations while τ_{q_2} relates to deeper fluctuations.

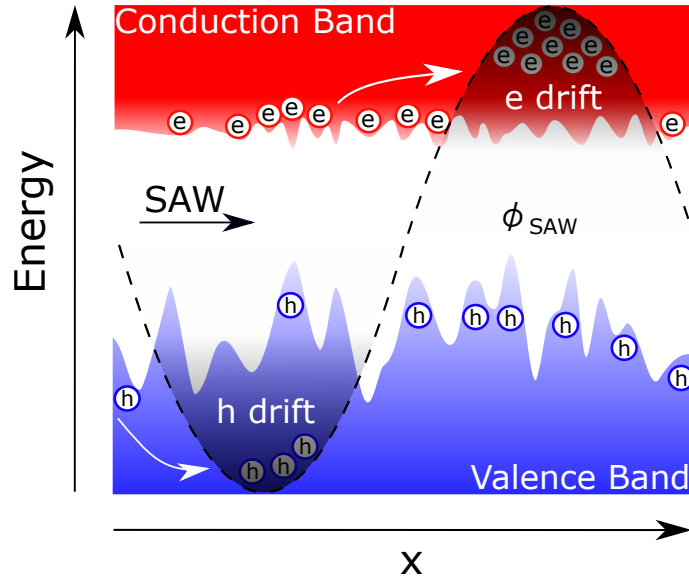


Figure 6.9: Illustration of the conduction and valence bands potential fluctuations along the carrier transport path. The SAW modulated piezoelectric potential ϕ_{SAW} (not to scale with the potential fluctuations) is represented by the dashed line.

The PL recovery process, on the other hand, possibly follows a complex dynamics which may depend of the rearrangement of carriers in the potential fluctuations, carrier tunneling from the substrate, or even rearrangement of adatoms on the ML surface after the in-plane piezoelectric field is turned off. This explains why, differently from the quenching process which is determined only by the driving SAW piezoelectric field, the recovery process seems to be more characteristic of each sample.

6.4 SAW-induced PL quenching degree

Our experiments reveal that when in presence of a SAW, the excitonic PL is progressively quenched, reaching a minimum level after a given time. The degree of PL quenching can be determined by taking into account the PL intensity at the exact moment in which the SAW is turned off. When $t \rightarrow t_{OFF}$, Equations 6.1 and 6.2 lead to:

$$Q_{PL} = 1 - I_{PL}(t_{OFF}), \quad (6.3)$$

where $I_{PL}(t_{\text{OFF}})$ is the normalized PL intensity at the time $t = t_{\text{OFF}}$. Q_{PL} is also indicated in Figure 6.5 by a blue arrow.

The following subsections bring the analysis of Q_{PL} on the SAW experiments which were carried out with the MoSe₂ and MoS₂ MLs as a function of acoustic power and two additional series of SAW experiments carried out with the MoS₂ ML sample as a function of the temperature and laser excitation power.

6.4.1 Acoustic power

Figures 6.10a and 6.10b show the resulting quenching profiles of X^- and X^0 emissions of the MoSe₂ ML, respectively, while Figures 6.10c and 6.10d show the profiles of the excitonic ($X^0 + X^-$) and LS emission bands of the MoS₂ ML sample, respectively. The experiments were conducted with different values of the SAW in-plane electric field. The experiments conducted on the MoSe₂ ML used SAW fields in the range of 19.5 - 50 kV/cm, while fields in the range of 5 - 21 kV/cm were employed on the MoS₂ ML due to the difference of the output power of each device, as discussed in Chapter 5. Figures 6.10.a-d show that the quenching degree depends on the amplitude of the applied acoustic field.

We observe some fluctuations on some of the the PL profiles, especially the 50kV/cm (purple) profile of the X^- emission and the X^0 PL profiles of the MoSe₂ ML. We attribute these fluctuations to mechanical instabilities of the optical setup. In the MoSe₂ experiments, we used a 100X objective lens, which produces a spot of $\sim 1 \mu\text{m}$, so that even small drifts can induce fluctuations in the PL signal. Since the quenching dynamics is very slow, when the sample moves the PL excitation spot moves to a region of the sample which has not been optically excited, leading to the "bumps" in the PL decay profile. The MoSe₂ X^0 profiles, shown in Figure 6.10b exhibit a more pronounced instability due to lower density of X^0 when compared to the X^- population, which leads to lower a PL signal and also a subsequent higher signal to noise ratio. The resulting profiles of both excitonic and LS emissions lines of the MoS₂ ML, on the other hand, exhibit much lower fluctuations when compared to the MoSe₂ ML because, in these experiments, we used a 20X objective lens,

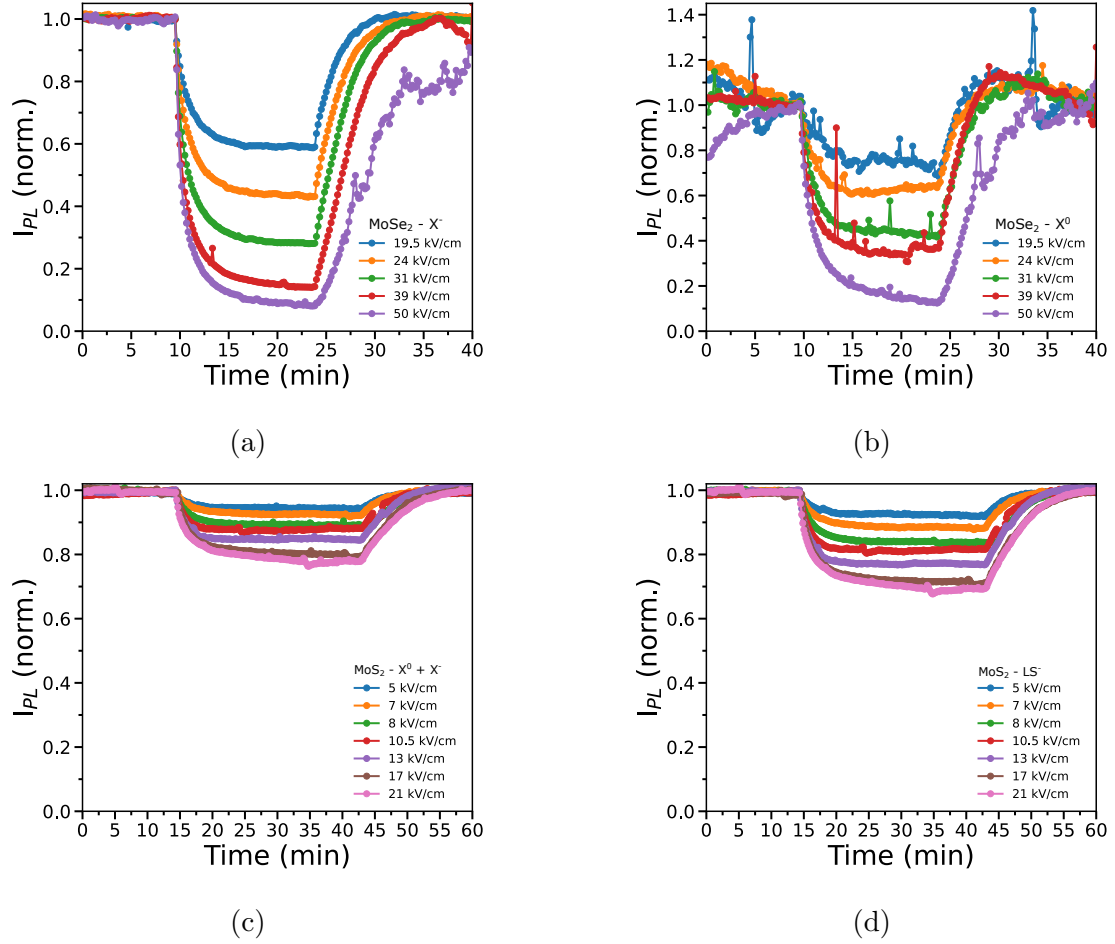


Figure 6.10: Time transients of X^- (a) and X^0 (b) emissions of the MoSe₂ ML sample and excitonic ($X^0 + X^-$) (c) and defect-related (d) emission bands of the MoS₂ ML sample for different values of E_1 .

which produces a wider spot ($\sim 5\mu\text{m}$) and minimizes the effects of the mechanical instabilities. Note that the experiments in the MoS₂ sample last 50% longer than the ones in the MoSe₂ ML and fluctuations are fully minimized.

Figure 6.11 shows Q_{PL} of the X^- (blue circles) and X^0 (red circles) emission lines of the MoSe₂ sample and $X^0 + X^-$ (green squares) and LS (orange squares) emission bands of the MoS₂ sample as a function of the SAW in-plane piezoelectric field E_1 . We averaged the PL signal during two minutes before turning on and off the SAW beam (indicated by the orange horizontal dashed lines in Figure 6.3) to calculate Q_{PL} with Equation 6.3. The uncertainty of Q_{PL} is estimated using the standard deviation of the averaged PL intensity. The values of the errors are

approximately equal to 0.001 on the case of both emission lines of the MoS₂ ML and the X⁻ emission of the MoSe₂ ML, but reaches up to 0.007 on the case of the X⁰ emission of the MoSe₂ ML, where the signal exhibits the most intense fluctuations, as discussed.

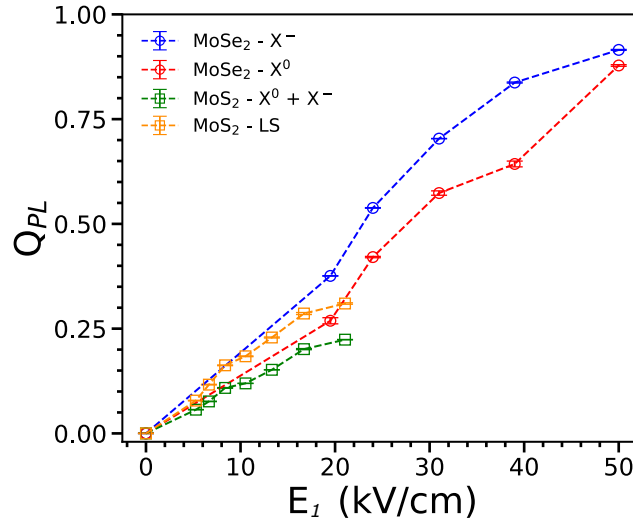


Figure 6.11: PL quenching (Q_{PL}) as a function of E_1 for X⁻ (blue circles) and X⁰ (red circles) emission lines of the MoSe₂ ML and X⁰ + X⁻ (green squares) and LS (orange squares) emission bands of the MoS₂ ML.

We observe in Figure 6.11 that Q_{PL} increases almost linearly with E_1 for all the emission lines of both samples and reaches 90% at high fields on the MoSe₂ sample. At low fields, the X⁰ + X⁻ and LS emission bands of the MoS₂ ML are quenched by, approximately 6% and 8%, respectively, indicating that the the SAW interacts with excitonic complexes even at very low effective powers. Furthermore, as in the case of the decay times presented in Figure 6.6, Q_{PL} depends only on the amplitude of E_1 . This fact is expected due to similar electronic and optical properties of the materials and demonstrates that the observed effect is solely due to the SAW driving piezoelectric field.

As a final remark, SAW experiments were carried out on the LiNbO₃ substrate in order to evaluate the contribution of possible SAW-driven effects of the substrate broad emission to the calculated Q_{PL} of the MoS₂ emission bands, shown in Figure 6.2c. There is no emission associated to the substrate in the spectral region of the

MoSe₂ ML. Figure 6.12a shows the PL spectra measured on the MoS₂ ML (blue) and the LiNbO₃ surface (green) in the absence a SAW beam. We note that, since the ML has degraded over time, it's PL emission is on the same order of magnitude of the LiNbO₃ PL (measured outside the ML), which suggests that the substrate might be responsible for a portion of the overall PL signal measured on the ML. Figure 6.12a also shows the PL spectra of this ML (orange) and the substrate (red) when a SAW beam with $E_1 = 9\text{kV/cm}$ is applied, revealing that the PL emission of the substrate is also affected. Figure 6.12b shows the degree of Q_{PL} obtained at different E_1 amplitudes. The values of Q_{PL} attributed to the substrate were calculated using the same spectral window of each emission of the ML. We observe that the degree of Q_{PL} of both ML and substrate emissions exhibits a growth trend as the piezoelectric field is increased, but the PL signal of the ML is systematically more quenched. This fact shows that the degree of ML PL quenching is larger than the one of the substrate. In this situation, our results suggest that the values of Q_{PL} of the emission bands of the MoS₂ ML displayed in this section may be slightly underestimated.

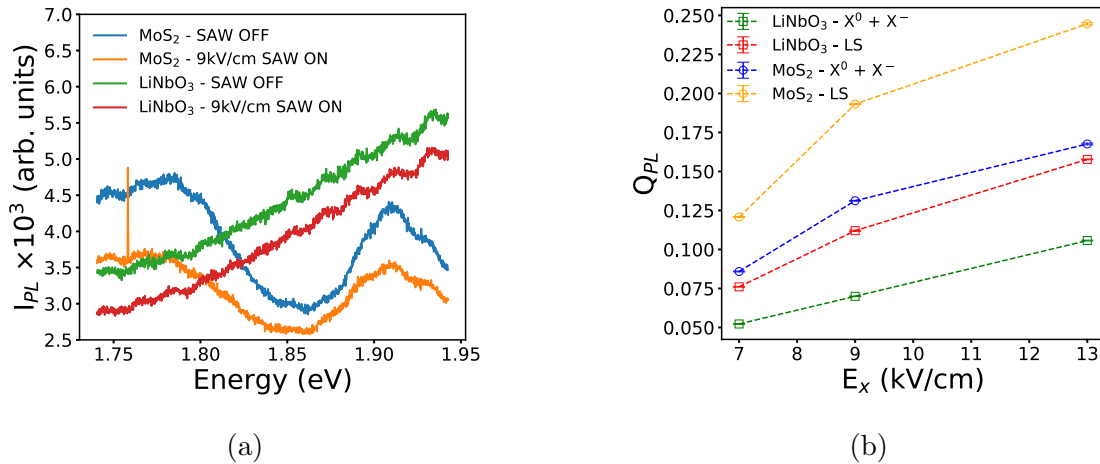


Figure 6.12: (a) PL spectra of the MoS₂ ML and the LiNbO₃ substrate before and after a SAW beam with 9kV/cm in-plane electric field is turned on. (b) Degree of Q_{PL} achieved in the SAW experiments conducted on the MoS₂ ML and the LiNbO₃ substrate. Q_{PL} of the substrate is calculated using the same spectral window of each emission band of the ML.

6.4.2 Temperature

Figure 6.13 shows the temperature dependence of Q_{PL} of the MoS₂ X^0+X^- (green squares) and LS (orange triangles) emission bands of the MoS₂ ML. The experiments were carried out at a constant E_1 amplitude of 8kV/cm and a laser line with $\lambda = 532\text{nm}$, a constant excitation power of 1mW, and a 20X objective lens. Figure 6.13 shows that Q_{PL} slightly decreases as the temperature increases, possibly due to the extra thermal energy which makes the carrier drift process less efficient. The small decrease indicates that, up to 150K, the temperature of the sample has a minor role on the Q_{PL} when compared to the SAW field amplitude. This fact also leads us to infer that there is no significant contribution of possible SAW-induced heating effects (which is commonly observed when the nominal RF power applied to SAW-generating device is large [67]) in the results presented in Figure 6.11, where Q_{PL} steadily increases with the acoustic power.

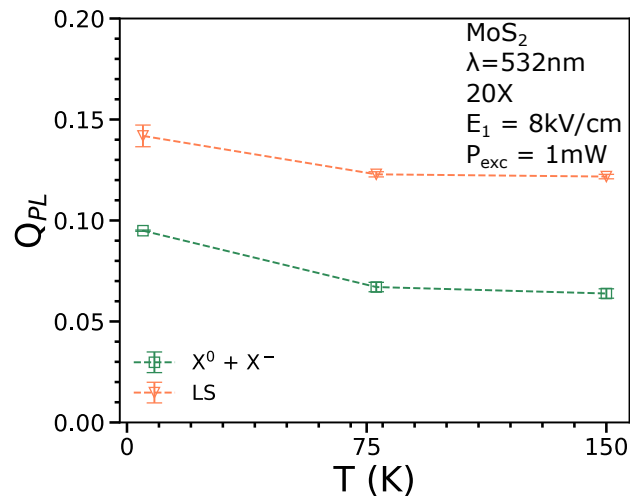


Figure 6.13: PL quenching (Q_{PL}) as function of the temperature for $X^0 + X^-$ (green squares) and LS (orange triangles) emission bands of the MoS₂ ML.

6.4.3 Laser power

Figure 6.14 shows the behavior of Q_{PL} for the $X^0 + X^-$ and LS emission bands of MoS₂ sample as a function of laser excitation power (P_{exc}). We conducted

these experiments at a constant E_1 amplitude of 8 kV/cm on the MoS₂ ML sample at 78K and 150K and, once again, the experiments were carried out using the $\lambda = 532\text{nm}$ laser line and the 20X objective lens. No drastic changes or trend in Q_{PL} can be detected in Figure 6.14 within the range of excitation powers used in our experiments. This means that, even at relatively weak acoustic fields (i) the PL quenching efficiency does not decrease with the excited exciton density up to liquid nitrogen temperatures and (ii) no laser-induced heating can be detected in the experiments. The observations reveal the stability of the SAW-driven mechanism responsible for the PL quenching.

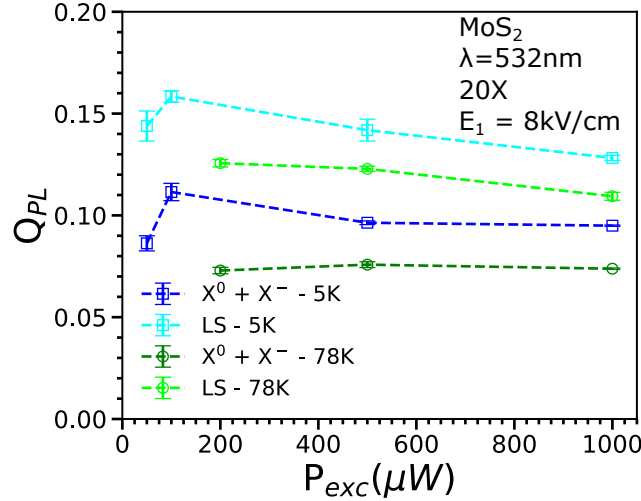


Figure 6.14: Q_{PL} as function of P_{exc} for the $X^0 + X^-$ and LS emission bands of the MoS₂ ML at 5K (blue and cyan, respectively) and 78K (dark and light green, respectively).

6.4.4 Thermal stability

In order to discuss the thermal stability of our experiments, we present discussion on the SAW-induced heating process. Figure 6.15 shows the two-dimensional time evolution map of the PL with SAW in the MoSe₂ ML under the highest value of E_1 which was applied to this sample (50 kV/cm, which corresponds to an input RF power of +26dBm). The map starts at minute 10 and stops at minute 25, when the SAW beam is turned on and off, respectively. The color scale is intentionally

saturated in order to highlight the X⁻ emission after PL is considerably quenched. After the SAW is turned on, for all acoustic powers, the PL redshifts and stabilizes at a constant wavelength. When the SAW is turned off, the PL quickly blueshifts back to its unperturbed state and starts to recover its intensity.

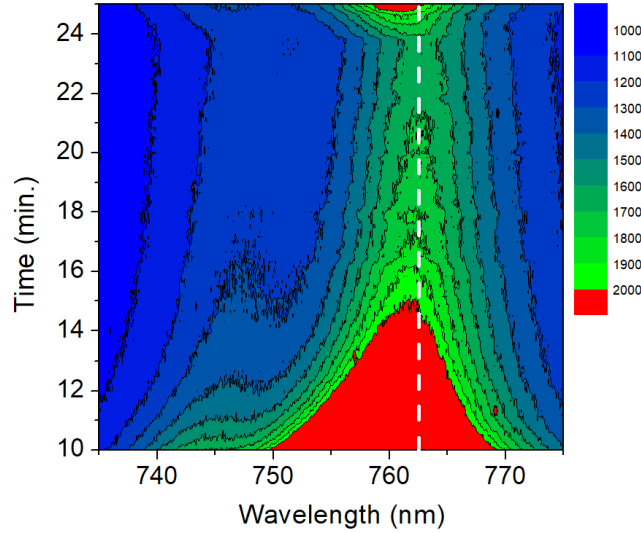


Figure 6.15: PL saturated quenching map of the MoSe₂ X⁰ and X⁻ emission lines at the highest acoustic power applied on this sample (26 dBm). White dashed line is a guide for the eye. The map starts and finishes at the minutes 10 and 25, when the SAW is turned on and off, respectively.

Considering a simple heat exchange model for a body at a given initial temperature T_i placed in contact with a medium at a different temperature, the body temperature $T(t)$ tends exponentially to the equilibrium value T_{eq} over time as:

$$T(t) = T_{eq} + (T_i - T_{eq})e^{-bt}, \quad (6.4)$$

where b is the thermal time constant. In lumped systems, $b = 1/R_t C_t$, where R_t is the resistance to heat transfer and C_t is the lumped thermal capacitance of the solid. The thermal time constant b essentially depends on the heat transfer coefficient and on the body characteristics like specific heat, volume, and contact area.

In the presence of heating due to the RF power applied to the FEUDT, depending on the thermal equilibrium dynamics, two scenarios could be observed. If b is low, the body temperature would tend slowly to thermal equilibrium and the

red-shift would always increase during the time that PL is monitored. On the other hand, if b is high, the PL emission would redshift and stabilize, which is the behavior observed in the experiments, as shown in Figure 6.15. In all experiments, the redshift of the PL peaks stabilize after a given time (associated with τ_{q1}), thus b is not expected to depend on the acoustic power.

Moreover, a temperature increase after the SAW is turned on should lead to a decrease in the PL quenching degree in time, which is not observed in Figure 6.15. This is the same behavior observed in the experiments performed in the MoS₂ ML shown in Figures 6.10c and 6.10d, where we applied even higher nominal acoustic powers (up to 30 dBm), but no extra PL redshift or change in QL was observed.

The experiments demonstrate that the parameter which really determines the amplitude of the redshift is not the applied power, but rather the SAW piezoelectric field. As discussed in chapter 5, higher nominal RF powers were applied to the MoS₂ due to the reduced power conversion and yet, the redshifts observed are smaller than the ones of the MoSe₂ ML. These considerations led us to exclude any significant contribution of SAW-induced heating to the redshift and the PL quenching observed in our experiments.

6.5 Exciton dissociation

Figure 6.16 shows the ratio $I_{PL}^{X^-}/I_{PL}^{X^0}$ between the two integrated intensities of X⁻ and X⁰ emissions of the MoSe₂ ML as a function of E_1 . The ratio drops from a factor of more than 15 in the absence of the SAW to about 3 at $E_1 = 50$ kV/cm, demonstrating that the SAW quenches more efficiently the X⁻ emission as compared to X⁰, which is consistent with the larger Q_{PL} shown in Figure 6.11. Moreover, as discussed in Chapter 2, the calculated binding energy of the neutral exciton is 52 meV, which is larger than the measured 35 meV of the trion binding energy, suggesting that the SAW-driven process of dissociation might privilege the trion due to the smaller binding energy.

Figure 6.17 shows the dissociation rate (τ_{dis}^{-1}) as a function of E_1 , calculated

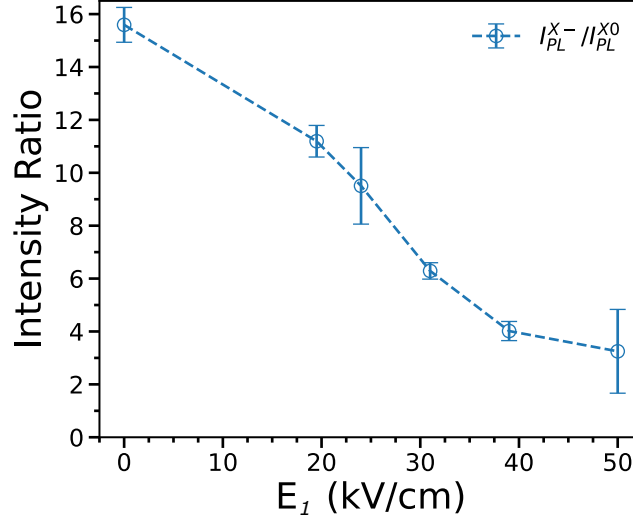


Figure 6.16: X⁻ and X⁰ intensity ratio $I_{PL}^{X^-}/I_{PL}^{X^0}$ as a function of E_1 .

with Equation 3.43 for three different situations. The orange circles correspond to τ_{dis}^{-1} calculated using $E_B^{X^0} = 500$ meV, which represents the neutral exciton in the low dielectric screening regime which is typically achieved when a TMD ML is placed over a SiO₂/Si substrate or encapsulated in h-BN. The purple circles represent the situation of strong dielectric screening, as discussed in chapter 2, where the full interaction potential is used to calculate the 52 meV neutral exciton binding energy in the MoSe₂ ML on the LiNbO₃ substrate as 52 meV. The green circles represent the MoSe₂ X⁻ complex, which has a binding energy of 35 meV.

Figure 6.17 shows that, under the weak dielectric screening regime (orange circles) the dissociation rate is negligible within the range of E_1 values which were used on our experiments, indicating that the SAW effects would be very small in this situation, as reported by Rezk and coworkers [67], where only a small PL quenching could be achieved in similar experiments. On the other hand, τ_{dis}^{-1} exhibits an onset around 35 kV/cm for the X⁰ emission line at the strong dielectric screening regime (purple circles). The calculated dissociation rate for the X⁻, in turn, exhibits an onset around 20 kV/cm and becomes greater than 30 ns⁻¹ around 30 kV/cm, which is comparable to the trion radiative decay rate at low temperature [105], as discussed in Chapter 2.

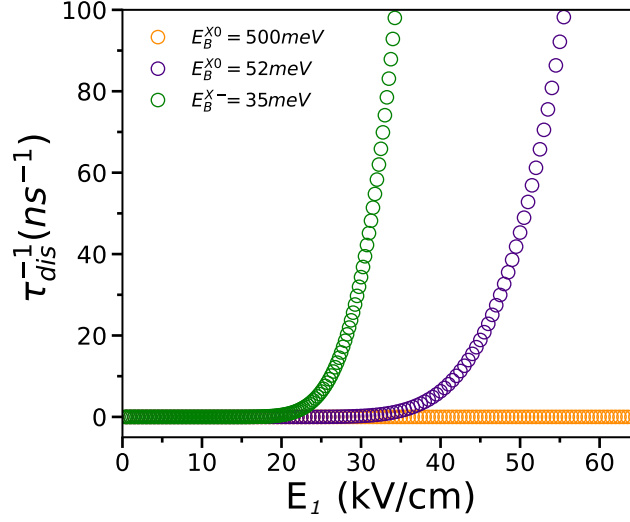


Figure 6.17: Field-induced dissociation rate τ_{dis}^{-1} as a function of the SAW in-plane electric field E_1 . τ_{dis}^{-1} is calculated with Equation 3.43 for the neutral exciton on SiO₂ substrate (orange circles) where $E_B^{X0} = 500$ meV, neutral exciton (purple circles) and negative trion (green circles) on LiNbO₃ substrate, where $E_B^{X0} = 52$ meV and $E_B^{X-} = 35$ meV respectively.

The onset of PL quenching in our experiments, however, is observed at even lower fields than the ones shown in Figure 6.17. For the MoSe₂ ML, at $E_1 = 19.5$ kV/cm, which is the lowest field, Q_{PL} was approximately 30%. Moreover, for the MoS₂ ML, in-plane fields lower than 10 kV/cm already yielded observable PL quenching levels. The predictions obtained with equation 3.43 are, nevertheless, in very good agreement with the experiments in the sense of showing that the onset of PL quenching associated with the dissociation of both exciton complexes is expected at fields which are very similar to the experimental values.

Besides the tunnel dissociation, as discussed above, alternative mechanisms are also reported to promote the exciton dissociation and reduce the PL onset to lower piezoelectric fields. A relevant contribution to exciton dissociation comes from the impact with accelerated electrons due to the high in-plane SAW piezoelectric field. This mechanism leads to lower quenching PL quenching onsets than the expected in GaAs quantum wells [148]. Furthermore, as trion dissociation starts, the number of free electrons in the system raises and might intensify the neutral exciton dissociation. Moreover, the SAW modulated strain may also have a small contribution to

exciton dissociation [45, 127] explaining the onset at fields lower than expected for τ_{dis}^{-1} observed in the experiments for both exciton and trion.

Yet another factor contributing to the PL quenching is the SAW-induced transport of carriers away from the laser generation spot. This effect can be evaluated by calculating the minimum value of carrier mobility ($\mu_{carrier}$) required for an efficient acoustic transport, which is given as:

$$\mu_{carrier} = \frac{v_{SAW}}{E_1}, \quad (6.5)$$

being $v_{SAW} = 3959 \text{ m/s}$ the SAW propagation velocity on the X direction of a Y128° LiNbO₃ surface, and E_1 is the in-plane piezoelectric field amplitude. In our case, the minimum carrier mobility is $\approx 20 \text{ cm}^2/\text{Vs}$ for $E_1 = 20 \text{ kV/cm}$, which is smaller than typical low-temperature values for exfoliated MoSe₂ MLs, measured as $50 \text{ cm}^2/\text{Vs}$ at room temperature and $200 \text{ cm}^2/\text{Vs}$ at liquid Nitrogen temperature [149], thus indicating that the degree of PL quenching in our experiments is also affected by the carrier transport away from the laser excitation spot.

6.6 SAW-induced excitonic Stark effect

Besides the SAW-induced PL quenching, Figures 6.18a and 6.18b also show that the X^- and X^0 emissions of the MoSe₂ and the excitonic emission band of the MoS₂ ML redshift as the SAW power increases. The inset in Figure 6.18a shows the normalized PL intensity in the absence of a SAW (in blue) and with a 50 kV/cm in-plane SAW piezoelectric field E_1 (in purple) indicating the redshift of X^0 and X^- emission lines. Figure 6.19 displays the PL energy shift (ΔE) of the X^0 (red circles) and X^- (blue circles) emissions of the MoSe₂ ML and the excitonic emission band (green squares) of the MoS₂ ML as a function of E_1 . We observe that, at $E_1 = 50 \text{ kV/cm}$, $\Delta E = 11.6 \text{ meV}$ for X^- and 9.2 meV for X^0 emissions of the MoSe₂, while the MoS₂ excitonic emission exhibits very small energy shifts at low fields. ΔE exhibit a quadratic behavior, which is typical of the Stark effect.

As discussed in chapter 3, the total energy modulation promoted by the prop-

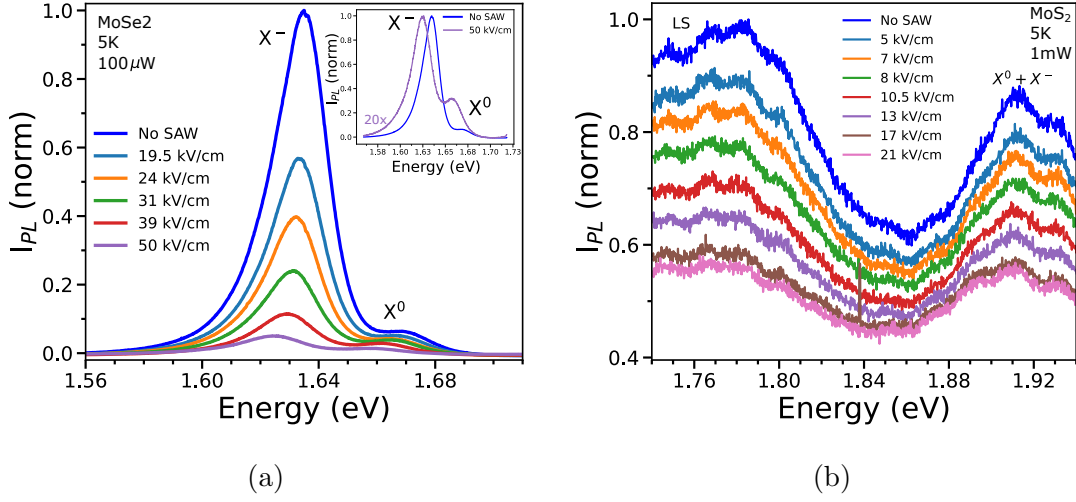


Figure 6.18: MoSe₂ (a) and MoS₂ (b) ML PL spectra (average for 2 minutes) before the SAW is turned on (blue) and for different in-plane SAW fields (remaining spectra) before it is turned off. The inset in (a) shows the normalized PL intensity in the absence of a SAW (in blue) and with a 50 kV/cm in-plane SAW piezoelectric field E_1 (in purple) indicating the redshift of X^0 and X^- emission lines.

agating SAW beam is a superposition of the piezoelectric field Stark effect (ΔE_{Stark}) and the strain-induced bandgap modulation (ΔE_{strain}), as stated in equation 3.42. The dashed gray line in Figure 6.19 is the linear contribution ΔE_{strain} obtained from the $\delta V/V$ values calculated for each acoustic power by adopting the value $a_0 = 30$ meV/% reported for MoSe₂ MLs [127, 150]. The red and blue solid lines are fittings with equation 3.42 (taking ΔE_{strain} into account) of the X^0 and X^- experimental ΔE values, respectively. They reproduce very well the experimental data, thus showing that the in-plane piezoelectric field E_1 is the major responsible for the PL redshift.

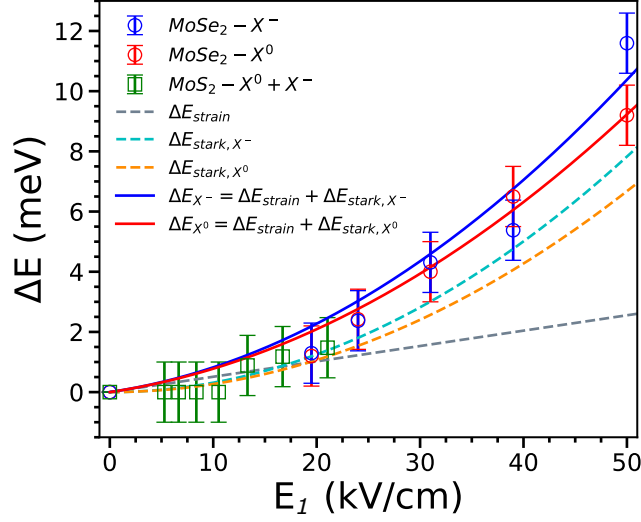


Figure 6.19: MoSe₂ X⁻ (blue circles) and X⁰ (red circles) emissions redshift (ΔE) as a function E_1 . The gray dashed line is the calculated hydrostatic strain contribution (ΔE_{strain}). The solid blue and red lines are fits to the experimental data of X⁻ and X⁰ emissions, respectively. The dashed cyan and orange lines are the Stark shift contributions (ΔE_{Stark}) to ΔE extracted from the fits. The values of ΔE for the X⁰ + X⁻ emission of MoS₂ (green squares) are also shown.

From the fittings, we isolate ΔE_{Stark} for each excitonic emission, as shown in cyan and orange dashed lines in Figure 6.19. We obtain the first experimental values of $\alpha_{X^0} = (53 \pm 5) \times 10^{-4} \text{ meV}/(\text{kV}/\text{cm})^2$ and $\alpha_{X^-} = (63 \pm 7) \times 10^{-4} \text{ meV}/(\text{kV}/\text{cm})^2$ for the MoSe₂ neutral exciton and trion in-plane polarizabilities, respectively. However, in order to compare with the reported values of the literature, we will refer to the obtained values of polarizabilities in units of $10^{-5} \text{ meV}/(\text{kV}/\text{cm})^2$ as $\alpha_{X^0} = (530 \pm 50) \times 10^{-5} \text{ meV}/(\text{kV}/\text{cm})^2$ and $\alpha_{X^-} = (630 \pm 70) \times 10^{-5} \text{ meV}/(\text{kV}/\text{cm})^2$. Moreover, since the neutral exciton and trion binding energies are quite similar in our system, it is reasonable to expect that the individual in-plane polarizabilities will exhibit similar magnitudes, as observed.

Table 6.1 brings the values of X⁰ and X⁻ in-plane polarizabilities (α) of MoSe₂ and WSe₂ MLs placed on different substrates. Pedersen [151] calculates the in-plane polarizability of the neutral exciton for a MoSe₂ ML as $\approx 15 \times 10^{-5} \text{ meV}/(\text{kV}/\text{cm})^2$ when the relative dielectric constant of the environment is $\sim 5\epsilon_0$, and $\approx 60 \times 10^{-5} \text{ meV}/(\text{kV}/\text{cm})^2$ for a relative dielectric constant of $\sim 10\epsilon_0$, thus indicating that the

Table 6.1: Values of X⁰ and X⁻ in-plane polarizabilities (α) of MoSe₂ and WSe₂ MLs placed on different substrates, which are labeled by the dielectric constant ε in terms of the vacuum permittivity (ε_0).

Material		α (10^{-5} meV/(kV/cm) ²)	$\varepsilon(\varepsilon_0)$	Reference
MoSe ₂	X ⁰	530	56 (LiNbO ₃)	[69]
		6.5	4 (h-BN-encapsulated)	[129]
		15	5	[151]
		60	10	[151]
	X ⁻	630	56 (LiNbO ₃)	[69]
		200	4 (h-BN-encapsulated)	[129]
WSe ₂	X ⁰	10	4 (h-BN-encapsulated)	[38]
		90	56 (LiNbO ₃)	[68]

polarizability is expected to increase with the substrate dielectric constant, which is in agreement with our measurement of larger polarizabilities at a higher dielectric constant. Cavalcante and coworkers [129] calculates the neutral exciton in-plane polarizability on the order of $\sim 6.5 \times 10^{-5}$ meV/(kV/cm)² for an encapsulated MoSe₂ ML, which also corroborates the dependence of the polarizability on the dielectric constant.

A similar behaviour is observed for WSe₂ MLs. The neutral exciton in-plane polarizability has been measured by Massicote and coworkers [38] as $\alpha_{X^0} \approx 10.4 \times 10^{-5}$ meV/(kV/cm)² for h-BN-encapsulated WSe₂ ML, while a recently reported experiment by Datta and coworkers [68] measure the in-plane polarizability of the neutral exciton of a WSe₂ ML placed over a LiNbO₃ substrate as $\approx 90 \times 10^{-5}$ meV/(kV/cm)², which is an increase of almost 10x when compared to the weak dielectric screening situation.

The obtained value for the trion polarizability is also compatible with theoretical predictions. Cavalcante and coworkers [129] calculates a high trion in-plane polarizability on the order of $\sim 200 \times 10^{-5}$ meV/(kV/cm)² for an encapsulated

MoSe₂ ML. The dielectric constant of the LiNbO₃ substrate is $56\epsilon_0$, so that it is reasonable to find a higher value of polarizability in the experiments.

Figure 6.19 also presents the redshift observed for the excitonic emission band ($X^0 + X^-$) of MoS₂ (green dots). We did not detect any measurable energy shift on the LS emission, probably due to the large band width. Due to the lower piezoelectric fields achieved on this device, we were able to probe only the low electric field limit on this sample. However, the small redshifts observed for fields above 10 kV/cm indicate that the polarizability of MoS₂ and MoSe₂ are similar, as expected from the theoretical calculations [129, 151].

CHAPTER 7

Conclusions

We investigated the manipulation of the excitonic dynamics in two-dimensional TMD MLs using traveling SAWs fields.

We demonstrated that the strong dielectric screening provided by the LiNbO₃ substrate reduced the neutral exciton binding energy and increased the field-induced dissociation. The optically-generated excitonic complexes were dissociated by the traveling piezoelectric field of the SAW, which caused a suppression of the PL emission intensity. The PL quenching exhibited an almost linear growth trend with the SAW in-plane piezoelectric field and reached up to 90 %. Sample temperature and laser excitation power did not have significant contribution to the quenching promoted by the SAW. Also, we did not observe effects of heating in our results, which indicate a highly stable process. Moreover, the PL quenching dynamics was characterized by slow decay and recovery processes, which we attributed to the presence of potential fluctuations along the SAW transport path that acted as traps for the charge carriers and limited the efficient transport and prevented a more efficient drift process.

The excitonic emission energies were also red-shifted in the presence of the SAW beam. We proposed an acoustically-induced Stark effect model which allowed us to obtain the first measurement of the in-plane polarizabilities of both neutral exciton and negative trion of the MoSe₂ non-encapsulated ML within the strong dielectric screening condition as $\alpha_{X^0} = (530 \pm 50) \times 10^{-5} \text{ meV}/(\text{kV}/\text{cm})^2$ and $\alpha_{X^-} = (630 \pm 70) \times 10^{-5} \text{ meV}/(\text{kV}/\text{cm})^2$, respectively. Our results exhibited good

agreement with theoretical calculations that estimate an increase of the polarizability at higher values of dielectric constant.

Our findings demonstrated the applicability of SAWs as an effective contactless technique to manipulate many-body excitonic dynamics and modify the light emission properties of TMD MLs under the strong dielectric screening regime. In this way, we bring a new perspective by combining given experimental conditions: the highly piezoelectric platform and the strong dielectric screening provided by the LiNbO_3 . To our knowledge, our work is the first report of low-temperature acoustic modulation experiments in MoSe_2 MLs under strong dielectric screening.

Furthermore, we point the potential of the acoustic modulation of TMD MLs for future applications, such as light emission, carrier transport, sensing, and storing. From a basic research point of view, the entire discussion of the basic physics is extendable for other TMD materials, such as WS_2 and WSe_2 . Also, the entire platform (physical description, computational models and the experimental setup) can be used to investigate the acoustic modulation of van-der-Waals heterostructures and other two-dimensional systems.

CHAPTER 8

Publications

1. **Acoustically-Driven Stark Effect in Transition Metal Dichalcogenide Monolayers.** Diego Scolfaro, Matheus Finamor, Luca O. Trinchão, Bárbara L. T. Rosa, Paulo V. Santos, Fernando Iikawa and Odilon D. D. Couto Jr. ACS Nano - 2021- 15, 9, 15371–15380
2. **Rolled-Up Quantum Wells Composed of Nanolayered InGaAs/GaAs Heterostructures as Optical Materials for Quantum Information Technology.** Leonarde N. Rodrigues, Diego Scolfaro, Lucas da Conceição, Angelo Malachias, Odilon D. D. Couto Jr, Fernando Iikawa and Christoph Deneke. ACS Applied Nano Materials - 2021- 4 (3), 3140-3147..

Bibliography

- [1] K. S. Novoselov, A. K. Geim, S. V. Morozov, D. Jiang, Y. Zhang, S. V. Dubonos, I. V. Grigorieva, and A. A. Firsov. Electric field effect in atomically thin carbon films. *Science*, 306(5696):666–669, 2004.
- [2] K. S. Novoselov, D. Jiang, F. Schedin, T. J. Booth, V. V. Khotkevich, S. V. Morozov, and A. K. Geim. Two-dimensional atomic crystals. *Proc. Natl. Acad. Sci. USA*, 102:10451, 2005.
- [3] H. H. Huang, X. Fan, D. J. Singh, and W. T. Zheng. Recent progress of tmd nanomaterials: phase transitions and applications. *Nanoscale*, 12(3):1247–1268, 2020.
- [4] P. Avouris and F. Xia. Graphene applications in electronics and photonics. *Mrs Bulletin*, 37(12):1225–1234, 2012.
- [5] G. Wang, A. Chernikov, M. M. Glazov, T. F. Heinz, X. Marie, T. Amand, and B. Urbaszek. Excitons in atomically thin transition metal dichalcogenides. *Rev. Mod. Phys.*, 90:021001, 2018.
- [6] K. Khan, A. K. Tareen, M. Aslam, R. Wang, Y. Zhang, A. Mahmood, Z. Ouyang, H. Zhang, and Z. Guo. Recent developments in emerging two-dimensional materials and their applications. *Journal of Materials Chemistry C*, 8(2):387–440, 2020.

-
- [7] T. Cheiwchanchammangij and W. R. L. Lambrecht. Quasiparticle band structure calculation of monolayer, bilayer, and bulk MoS₂. *Phys. Rev. B*, 85:205302, 2012.
- [8] K. F. Mak, C. Lee, J. Hone, J. Shan, and T. F. Heinz. Atomically thin MoS₂: a new direct-gap semiconductor. *Phys. Rev. Lett.*, 105:136805, 2010.
- [9] A. Splendiani, L. Sun, Y. Zhang, T. Li, J. Kim, C. Chim, G. Galli, and F. Wang. Emerging photoluminescence in monolayer MoS₂. *Nano letters*, 10(4):1271–1275, 2010.
- [10] K. F. Mak, K. He, J. Shan, and T. F. Heinz. Control of valley polarization in monolayer MoS₂ by optical helicity. *Nature nanotechnology*, 7(8):494, 2012.
- [11] D. Xiao, G. B. Liu, W. Feng, X. Xu, and W. Yao. Coupled spin and valley physics in monolayers of MoS₂ and other group-VI dichalcogenides. *Phys. Rev. Lett.*, 108:196802, 2012.
- [12] X. Xu, W. Zao, D. Xiao, and T. F. Heinz. Spin and pseudospins in layered transition metal dichalcogenides. *Nature Phys.*, 10:343, 2014.
- [13] K. F. Mak and J. Shan. Photonics and optoelectronics of 2D semiconductor transition metal dichalcogenides. *Nature Photon.*, 10:216, 2016.
- [14] J. R. Schaibley, H. Yu, G. Clark, P. Rivera, J. S. Ross, K. L. Seyler, W. Yao, and X. Xu. Valleytronics in 2D materials. *Nat. Rev. Mater.*, 1:16055, 2016.
- [15] N. S. Arul and V. D. Nithya. *Two dimensional transition metal dichalcogenides: synthesis, properties, and applications*. Springer, 2019.
- [16] T. Mueller and E. Malic. Exciton physics and device application of two-dimensional transition metal dichalcogenide semiconductors. *NPJ 2D Materials and Applications*, 2(1):1–12, 2018.
- [17] M. Samadi, N. Sarikhani, M. Zirak, H. Zhang, H. Zhang, and A. Z. Moshfegh. Group 6 transition metal dichalcogenide nanomaterials: synthesis, applications and future perspectives. *Nanoscale Horizons*, 3(2):90–204, 2018.

- [18] A. Raja, A. Chaves, J. Yu, G. Arefe, H. M. Hill, A. F. Rigosi, T. C. Berkelbach, P. Nagler, C. Schueller, T. Korn, C. Nuckolls, J. Hone, L. E. Brus, T. F. Heinz, D. R. Reichman, and A. Chernikov. Coulomb engineering of the bandgap and excitons in two-dimensional materials. *Nature Commun.*, 8:15251, 2017.
- [19] A. K. Geim and I. V. Grigorieva. Van der waals heterostructures. *Nature*, 499:4, 2013.
- [20] H. Fang, C. Battaglia, C. Carraro, S. Nemsak, B. Ozdol, J. S. Kang, H. A. Bechtel, S. B. Desai, F. Kronast, A. A. Unal, et al. Strong interlayer coupling in van der waals heterostructures built from single-layer chalcogenides. *Proceedings of the National Academy of Sciences*, 111(17):6198–6202, 2014.
- [21] P. Rivera, J. R. Schaibley, A. M. Jones, J. S. Ross, S. Wu, G. Aivazian, P. Klement, K. Seyler, G. Clark, N. J. Ghimire, et al. Observation of long-lived interlayer excitons in monolayer MoSe₂-WSe₂ heterostructures. *Nature communications*, 6(1):1–6, 2015.
- [22] L. Wang, E. Shih, A. Ghiotto, L. Xian, D. A Rhodes, C. Tan, M. Claassen, D. M Kennes, Y. Bai, B. Kim, et al. Correlated electronic phases in twisted bilayer transition metal dichalcogenides. *Nature Materials*, 19(8):861–866, 2020.
- [23] M. R. Molas, C. Faugeras, A. O. Slobodeniuk, K. Nogajewski, M. Bartos, D. M. Basko, and M. Potemski. Brightening of dark excitons in monolayers of semiconducting transition metal dichalcogenides. *2D Materials*, 4(2), 2017.
- [24] A. Srivastava, M. Sidler, A. V. Allain, D. S. Lembke, A. Kis, and A. Imamoglu. Optically active quantum dots in monolayer WSe₂. *Nature Nanotechnology*, 10(6):491–496, 2015.
- [25] P. Tonndorf, R. Schmidt, R. Schneider, J. Kern, M. Buscema, G. A. Steele, A. Castellanos-Gomez, H. S. J. van der Zant, S. M. de Vasconcellos, and R. Bratschitsch. Single-photon emission from localized excitons in an atomically thin semiconductor. *Optica*, 2(4):347–352, 2015.

- [26] Y. Zhou, G. Scuri, D. S. Wild, A. A High, A. Dibos, L. A. Jauregui, K. Shu, C. and De Greve, K. Pistunova, A. Y Joe, et al. Probing dark excitons in atomically thin semiconductors via near-field coupling to surface plasmon polaritons. *Nature Nanotechnology*, 12(9):856–860, 2017.
- [27] M. Koperski, K. Nogajewski, A. Arora, V. Cherkez, P. Mallet, J. Veuillen, J. Marcus, P. Kossacki, and M. Potemski. Single photon emitters in exfoliated WSe₂ structures. *Nature Nanotechnology*, 10(6):503–506, 2015.
- [28] C. Chakraborty, L. Kinnischtzke, K. M. Goodfellow, R. Beams, and A. N. Vamivakas. Voltage-controlled quantum light from an atomically thin semiconductor. *Nature Nanotechnology*, 10:507, 2015.
- [29] Y. He, G. Clark, J. R. Schaibley, Y. He, M. Chen, Y. Wei, X. Ding, Q. Zhang, W. Yao, X. Xu, et al. Single quantum emitters in monolayer semiconductors. *Nature nanotechnology*, 10(6):497–502, 2015.
- [30] B. Radisavljevic, A. Radenovic, J. Brivio, V. Giacometti, and A. Kis. Single-layer Mos₂ transistors. *Nature nanotechnology*, 6(3):147–150, 2011.
- [31] Z. Yin, H. Li, H. Li, L. Jiang, Y. Shi, Y. Sun, G. Lu, Q. Zhang, X. Chen, and H. Zhang. Single-layer MoS₂ phototransistors. *ACS nano*, 6(1):74–80, 2012.
- [32] M. Amani, D. H. Lien, D. Kiriya, J. Xiao, A. Azcatl, J. Noh, R. Madhvapathy, R. Addou, K. C. Santosh, M. Dubey, K. Cho, R. M. Wallace, S. C. Lee, H. He, J. W. Ager, X. Zhang, E. Yablonovitch, and A. Javey. Near-unity photoluminescence quantum yield in MoS₂. *Science*, 350(6264):1065–1068, 2015.
- [33] E. J. Sie, J. W. McIver, Y.H. Lee, L. Fu, J. Kong, and N. Gedik. Valley-selective optical stark effect in monolayer WS₂. *Nature Mater.*, 14:290, 2014.
- [34] J. Kim, X. Hong, C. Jin, S. F. Shi, C. Y. S. Chang, M. H Chiu, L. J. Li, and F. Wang. Ultrafast generation of pseudo-magnetic field for valley excitons in WSe₂ monolayers. *Science*, 346:1205, 2014.

- [35] J. Lee, S. Pak, Y. Lee, Y. Cho, J. Hong, P. Giraud, H. S. Shin, S. M. Morris, J. I. Sohn, S. Cha, et al. Monolayer optical memory cells based on artificial trap-mediated charge storage and release. *Nature Communications*, 8(1):1–8, 2017.
- [36] E. Preciado, F. J.R. Schuelein, A. E. Nguyen, D. Barroso, M. Isarraraz, G. von Son, I-H Lu, W. Michailow, B. Moeller, V. Klee, J. Mann, A. Wixforth, L. Bartels, and H. J. Krenner. Scalable fabrication of a hybrid field-effect and acousto-electric device by direct growth of monolayer MoS₂/LiNbO₃. *Nature Communications*, 6:8593, 2015.
- [37] F. Y. Shih, Y. C. Wu, Y. S. Shih, M. C. Shih, T. S. Wu, P. H. Ho, C. W. Chen, Y. F. Chen, Y. P. Chiu, and W. H. Wang. Environment-insensitive and gate-controllable photocurrent enabled by bandgap engineering of MoS₂ junctions. *Scientific Reports*, 7(October 2016):1–8, 2017.
- [38] M. Massicotte, F. Violla, P. Schmidt, M. B. Lundberg, S. Latini, S. Hastrup, M. Danovich, D. Davydovskaya, K. Watanabe, T. Taniguchi, V. I. Fal'ko, K. S. Thygesen, T. G. Pedersen, and F. H.L. Koppens. Dissociation of two-dimensional excitons in monolayer WSe₂. *Nature Communications*, 9(1):1–7, 2018.
- [39] J. Pak, I. Lee, K Cho, J. K. Kim, H. Jeong, W. T. Hwang, G. H. Ahn, K. Kang, W. J. Yu, A. Javey, S. Chung, and T. Lee. Intrinsic optoelectronic characteristics of MoS₂ phototransistors via a fully transparent van der waals heterostructure. *ACS Nano*, 13:9646, 2019.
- [40] J. Klein, Wierzbowski, A. Regler, Becker, F. Heimbach, K. Mueller, M. Kaniber, and J. J. Finley. Stark effect spectroscopy of mono- and few-layer MoS₂. *Nano Lett.*, 16:1554, 2016.
- [41] J. G. Roch, N. Leisgang, G. Froehlicher, P. Makk, K. Watanabe, T. Taniguchi, C. Schönenberger, and R. J. Warburton. Quantum-Confined Stark Effect in

- a MoS₂ Monolayer van der Waals Heterostructure. *Nano Letters*, 18(2):1070–1074, 2018.
- [42] A. Castellanos-Gomez, R. Roldan, E. Cappelluti, M. Buscema, F. Guinea, H. S. J. van der Zant, and G. A. Steele. Local strain engineering in atomically thin MoS₂. *Nano Lett.*, 13:5361, 2013.
- [43] K. He, C. Poole, K. F. Mak, and J Shan. Experimental demonstration of continuous electronic structure tuning via strain in atomically thin MoS₂. *Nano Lett.*, 13:2931, 2013.
- [44] H. Li, A. W. Contryman, X. Qian, S. M. Ardakani, Y. Gong, X. Wang, J. M. Weisse, C. H. Lee, J. Zhao, P. M. Ajayan, J. Li, H. C. Manoharan, and X. Zheng. Optoelectronic crystal of artificial atoms in strain-textured molybdenum disulphide. *Nature Commun.*, 6:7381, 2015.
- [45] E. Blundo, M. Felici, T. Yildirim, G. Pettinari, D. Tedeschi, A. Miriametro, B. Liu, W. Ma, Y. Lu, and A. Polimeni. Evidence of the direct-to-indirect band gap transition in strained two-dimensional WS₂, MoS₂, and WSe₂. *Phys. Rev. Res.*, 2:012024, 2020.
- [46] J. Feng, X. Qian, C. W. Huang, and J. Li. Strain-engineered artificial atom as a broad-spectrum solar energy funnel. *Nat. Photon.*, 6:866, 2012.
- [47] T. Li, F. and Shen, C. Wang, Y. Zhang, J. Qi, and H. Zhang. *Recent Advances in Strain-Induced Piezoelectric and Piezoresistive Effect-Engineered 2D Semiconductors for Adaptive Electronics and Optoelectronics*, volume 12. Springer Singapore, 2020.
- [48] P. Delsing, A. N. Cleland, M. J. A. Schuetz, J. Knörzer, G. Giedke, J. I. Cirac, K. Srinivasan, M. Wu, K. C. Balram, C. Bäuerle, T. Meunier, C. J. B. Ford, P. V. Santos, E. Cerda-Méndez, H. Wang, H. J. Krenner, E. D S Nysten, M. Weiß, G. R. Nash, L. Thevenard, C. Gourdon, P. Rovillain, M. Marangolo, J. Duquesne, G. Fischerauer, W. Ruile, A. Reiner, B. Paschke, D. Denysenko, D. Volkmer, A. Wixforth, H. Bruus, M. Wiklund, J. Reboud, J. M

- Cooper, Y. Fu, M. S. Brugger, F. Rehfeldt, and C. Westerhausen. The 2019 surface acoustic waves roadmap. *Journal of Physics D: Applied Physics*, 52(35):353001, 8 2019.
- [49] S. Volz, J. Ordonez-Miranda, A. Shchepetov, M. Prunnila, J. Ahopelto, T. Pezeril, G. Vaudel, V. Gusev, P. Ruello, E. M. Weig, et al. Nanophononics: state of the art and perspectives. *The European Physical Journal B*, 89(1):1–20, 2016.
- [50] D. Royer and E. Dieulesaint. *Elastic waves in solids I: Free and guided propagation*. Springer Science & Business Media, 1999.
- [51] M. Weiss and H. J. Krenner. Interfacing quantum emitters with propagating surface acoustic waves. *J. Phys.D: Appl. Phys.*, 51:373001, 2018.
- [52] C. Rocke, S. Zimmermann, A. Wixforth, J. P. Kotthaus, G. Böhm, and G. Weimann. Acoustically driven storage of light in a quantum well. *Physical Review Letters*, 78(21):4099, 1997.
- [53] C. Rocke, A. O. Govorov, A. Wixforth, G. Böhm, and G. Weimann. Exciton ionization in a quantum well studied by surface acoustic waves. *Physical Review B*, 57(12):R6850, 1998.
- [54] J. A. H. Stotz, R. Hey, P. V. Santos, and K. H. Ploog. Coherent spin transport via dynamic quantum dots. *Nature Materials*, 4:585, 2005.
- [55] O. D. D. Couto, Jr., F. Iikawa, J. Rudolph, R. Hey, and P. V. Santos. Anisotropic spin transport in (110) GaAs quantum wells. *Phys. Rev. Lett.*, 98:036603, 2007.
- [56] J. Rudolph, R. Hey, and P. V. Santos. Long-range exciton transport by dynamic strain fields in a GaAs quantum well. *Physical Review Letters*, 99(4):047602, 2007.

-
- [57] R. P. G. McNeil, M. Kataoka, C. J. B. Ford, C. H. W. Barnes, D. Anderson, G. A. C. Jones, I. Farrer, and D. A. Ritchie. On-demand single-electron transfer between distant quantum dots. *Nature*, 477(7365):439, 2011.
- [58] D. A. Fuhrmann, S. M. Thon, H. Kim, D. Bouwmeester, P. M. Petroff, A. Wixforth, and H. J. Krenner. Dynamic modulation of photonic crystal nanocavities using gigahertz acoustic phonons. *Nature Photon.*, 5:605, 2011.
- [59] F. J. R. Schülein, E. Zallo, P. Atkinson, O. G. Schmidt, R. Trotta, A. Rastelli, A. Wixforth, and H. J. Krenner. Fourier synthesis of radiofrequency nanomechanical pulses with different shapes. *Nature Nanotechnol.*, 10:512, 2015.
- [60] O. D. D. Couto, Jr., S. Lazic, F. Iikawa, J. A. H. Stotz, U. Jahn, R. Hey, and P. V. Santos. Photon anti-bunching in acoustically pumped quantum dots. *Nature Photon.*, 3:645, 2009.
- [61] D. A. Golter, T. Oo, M. Amezcua, K. A. Stewart, and H. Wang. Optomechanical quantum control of a nitrogen-vacancy center in diamond. *Phys. Rev. Lett.*, 116:143602, 2016.
- [62] C. Ruppert, F. Foerster, A. Zrenner, J. B. Kinzel, A. Wixforth, H. J. Krenner, and M. Betz. Radio frequency electromechanical control over a surface plasmon polariton coupler. *ACS Photon.*, 1:91, 2014.
- [63] M. M. de Lima Jr, M. van der Poel, P. V. Santos, and J. M. Hvam. Phonon-induced polariton superlattices. *Physical Review Letters*, 97(4):045501, 2006.
- [64] A. Hernández-Mínguez, Y. T. Liou, and P. V. Santos. Interaction of surface acoustic waves with electronic excitations in graphene. *Journal of Physics D: Applied Physics*, 51(38):383001, 2018.
- [65] S. Zheng, E. Wu, Z. Feng, R. Zhang, Y. Xie, Y. Yu, R. Zhang, Q. Li, J. Liu, W. Pang, et al. Acoustically enhanced photodetection by a black phosphorus-MoS₂ van der waals heterojunction p-n diode. *Nanoscale*, 10(21):10148–10153, 2018.

- [66] S. Zheng, E. Wu, and H. Zhang. Anomalous acoustoelectric currents in few-layer black phosphorus nanocrystals. *IEEE Transactions on Nanotechnology*, 17(3):590–595, 2018.
- [67] A. R. Rezk, B. Carey, A. F. Chrimes, D. W. M. Lau, B. C. Gibson, C. Zheng, M. S. Fuhrer, L. Y. Yeo, and K. Kalantar-zadeh. Acoustically-driven trion and exciton modulation in piezoelectric two-dimensional MoS₂. *Nano Lett.*, 16:849, 2016.
- [68] K. Datta, Z. Li, Z. Lyu, and P. B. Deotare. Piezoelectric modulation of excitonic properties in monolayer WSe₂ under strong dielectric screening. *ACS nano*, 15(7):12334–12341, 2021.
- [69] D. Scolfaro, M. Finamor, L. O. Trinchão, B. L. T. Rosa, P. V. Santos, F. Iikawa, and O. D. D. Couto Jr. Acoustically-driven Stark effect in transition metal dichalcogenide monolayers. *ACS Nano*, submitted, 2021.
- [70] A. R. Rezk, S. Walia, R. Ramanathan, H. Nili, J. Z. Ou, V. Bansal, J. R. Friend, M. Bhaskaran, L. Y. Yeo, and S. Sriram. Acoustic–excitonic coupling for dynamic photoluminescence manipulation of quasi-2D MoS₂ nanoflakes. *Adv. Opt. Mater.*, 3:888, 2015.
- [71] G. Huang and Y. Mei. Electromagnetic wave propagation in a rolled-up tubular microcavity. *J. Mat. Chem. C*, 5:2758, 2017.
- [72] A. Chernikov, T. C. Berkelbach, H. M. Hill, A. Rigosi, Y. Li, O. B. Aslan, D. R. Reichman, M. S. Hybertsen, and T. F. Heinz. Exciton binding energy and nonhydrogenic Rydberg series in monolayer WS₂. *Physical review letters*, 113(7):76802, 2014.
- [73] Z. Ye, T. Cao, K. O’Brien, H. Zhu, X. Yin, S. G. Wang, Y. and Louie, and X. Zhang. Probing excitonic dark states in single-layer tungsten disulphide. *Nature*, 513(7517):214, 2014.

- [74] M. M. Ugeda, A. J. Bradley, S. Shi, H. Felipe, Y. Zhang, D. Y. Qiu, W. Ruan, S. Mo, Z. Hussain, Z. Shen, et al. Giant bandgap renormalization and excitonic effects in a monolayer transition metal dichalcogenide semiconductor. *Nature Materials*, 13(12):1091–1095, 2014.
- [75] K. He, N. Kumar, L. Zhao, Z. Wang, K. F. Mak, H. Zhao, and J. Shan. Tightly bound excitons in monolayer WSe₂. *Physical Review Letters*, 113(2):026803, 2014.
- [76] S. Manzeli, D. Ovchinnikov, D. Pasquier, O. V. Yazyev, and A. Kis. 2D transition metal dichalcogenides. *Nature Reviews Materials*, 2, 2017.
- [77] W. Wu, L. Wang, Y. Li, F. Zhang, L. Lin, S. Niu, D. Chenet, X. Zhang, Y. Hao, Tony F. Heinz, et al. Piezoelectricity of single-atomic-layer MoS₂ for energy conversion and piezotronics. *Nature*, 514(7523):470–474, 2014.
- [78] E. N. Esfahani, T. Li, B. Huang, X. Xu, and J. Li. Piezoelectricity of atomically thin WSe₂ via laterally excited scanning probe microscopy. *Nano Energy*, 52:117–122, 2018.
- [79] Z. Y. Zhu, Y. C. Cheng, and U. Schwingenschlögl. Giant spin-orbit-induced spin splitting in two-dimensional transition-metal dichalcogenide semiconductors. *Physical Review B - Condensed Matter and Materials Physics*, 84(15):1–5, 2011.
- [80] A. Kormányos, G. Burkard, M. Gmitra, J. Fabian, V. Zolyomi, N. D. Drummond, and v. Falko. k·p theory for two-dimensional transition metal dichalcogenide semiconductors. *2D Materials*, 2:022001, 2015.
- [81] A. Klein, S. Tiefenbacher, V. Eyert, C. Pettenkofer, and W. Jaegermann. Electronic band structure of single-crystal and single-layer WS₂: Influence of interlayer van der waals interactions. *Physical Review B*, 64(20):205416, 2001.

- [82] G. Kioseoglou, A. T. Hanbicki, M. Currie, A. L. Friedman, D. Gunlycke, and B. T. Jonker. Valley polarization and intervalley scattering in monolayer MoS₂. *Applied Physics Letters*, 101(22), 2012.
- [83] W. H. Lin, W. S. Tseng, C. M. Went, M. L. Teague, G. R. Rossman, H. A. Atwater, and N. C. Yeh. Nearly 90% Circularly Polarized Emission in Monolayer WS₂ Single Crystals by Chemical Vapor Deposition. *ACS Nano*, 14(2):1350–1359, 2020.
- [84] H. Zeng, J. Dai, W. Yao, D. Xiao, and X. Cui. Valley polarization in MoS₂ monolayers by optical pumping. *Nature nanotechnology*, 7(8):490, 2012.
- [85] L. Yang, N. A. Sinitsyn, W. Chen, J. Yuan, J. Zhang, J. Lou, and S. A. Crooker. Long-lived nanosecond spin relaxation and spin coherence of electrons in monolayer MoS₂ and WS₂. *Nature Phys.*, 11:830, 2014.
- [86] R. Schmidt, A. Arora, G. Plechinger, P. Nagler, A. G. del Aguila, M. V Balotnin, P. C. M. Christianen, S. M. de Vasconcellos, C. Schueller, T. Korn, and R. Bratschitsch. Magnetic-field-induced rotation of polarized light emission from monolayer WS₂. *Physical Review Letters*, 117:077402, 2016.
- [87] M. Fox. *Optical properties of solids*. American Association of Physics Teachers, 2002.
- [88] C. F. Klingshirn. *Semiconductor optics*. Springer Science & Business Media, 2012.
- [89] H. C. Kamban and T. G. Pedersen. Field-induced dissociation of two-dimensional excitons in transition metal dichalcogenides. *Physical Review B*, 100(4):1–8, 2019.
- [90] M. Shinada and S. Sugano. Interband optical transitions in extremely anisotropic semiconductors. I. bound and unbound exciton absorption. *Journal of the Physical Society of Japan*, 21(10):1936–1946, 1966.

-
- [91] X. L. Yang, S. H. Guo, F. T. Chan, K. W. Wong, and W. Y. Ching. Analytic solution of a two-dimensional hydrogen atom. I. nonrelativistic theory. *Physical Review A*, 43(3):1186, 1991.
- [92] Natalia S Rytova. Screened potential of a point charge in a thin film. *Moscow University Physics Bulletin*, 22(18), 1967.
- [93] L. V. Keldysh. Coulomb interaction in thin semiconductor and semimetal films. *Journal of Experimental and Theoretical Physics Letters*, 29:658, 1979.
- [94] L. S. R. Cavalcante, A. Chaves, B. Van Duppen, F. M. Peeters, and D. R. Reichman. Electrostatics of electron-hole interactions in van der waals heterostructures. *Physical Review B*, 97(12):125427, 2018.
- [95] G. B. Arfken and H. J. Weber. *Mathematical methods for physicists*, 1999.
- [96] K. Wang, K. De Greve, L. A. Jauregui, A. Sushko, A. High, Y. Zhou, G. Scuri, T. Taniguchi, K. Watanabe, M. D. Lukin, et al. Electrical control of charged carriers and excitons in atomically thin materials. *Nature Nanotechnology*, 13(2):128, 2018.
- [97] D. Y. Qiu, H. Felipe, and S. G. Louie. Optical spectrum of MoS_2 : many-body effects and diversity of exciton states. *Physical review letters*, 111(21):216805, 2013.
- [98] A. J. Chaves, R. M. Ribeiro, T. Frederico, and N. M. R. Peres. Excitonic effects in the optical properties of 2D materials: an equation of motion approach. *2D Materials*, 4(2):025086, 2017.
- [99] P. R. Gray, P. J. Hurst, S. H. Lewis, and R. G. Meyer. *Analysis and design of analog integrated circuits*. John Wiley & Sons, 2009.
- [100] P. Soubelet, J. Klein, J. Wierzbowski, R. Silvioli, F. Sigger, A. V Stier, K. Gallo, and J. J. Finley. Charged exciton kinetics in monolayer MoSe_2 near ferroelectric domain walls in periodically poled LiNbO_3 . *Nano Letters*, 21(2):959–966, 2021.

-
- [101] K. Andersen, S. Latini, and K. S. Thygesen. Dielectric genome of van der waals heterostructures. *Nano letters*, 15(7):4616–4621, 2015.
- [102] A. V. Stier, N. P. Wilson, G. Clark, X. Xu, and S. A. Crooker. Probing the influence of dielectric environment on excitons in monolayer WSe₂: insight from high magnetic fields. *Nano Letters*, 16(11):7054–7060, 2016.
- [103] D. V. Tuan, M. Yang, and H. Dery. Coulomb interaction in monolayer transition-metal dichalcogenides. *Phys. Rev. B*, 98:125308, 2018.
- [104] J. S. Ross, S. Wu, H. Yu, N. J. Ghimire, A. M Jones, G. Aivazian, J. Yan, D. G. Mandrus, D. Xiao, W. Yao, and Others. Electrical control of neutral and charged excitons in a monolayer semiconductor. *Nature Communications*, 4:1474, 2013.
- [105] C. Robert, D. Lagarde, F. Cadiz, G. Wang, B. Lassagne, T. Amand, A. Balocchi, A. Renucci, S. Tongay, B. Urbaszek, and X. Marie. Exciton radiative lifetime in transition metal dichalcogenide monolayers. *Physical review B*, 93(20):205423, 2016.
- [106] G. D. Shepard, J. V. Ardelean, O. A. Ajayi, D. Rhodes, X. Zhu, J. C. Hone, and S. Strauf. Trion-species-resolved quantum beats in MoSe₂. *ACS Nano*, 11(11):11550–11558, 2017.
- [107] Z. Wang, L. Zhao, K. F. Mak, and J. Shan. Probing the spin-polarized electronic band structure in monolayer transition metal dichalcogenides by optical spectroscopy. *Nano Letters*, 17(2):740–746, 2017.
- [108] M. M. Glazov, T. Amand, X. Marie, D. Lagarde, L. Bouet, and B. Urbaszek. Exciton fine structure and spin decoherence in monolayers of transition metal dichalcogenides. *Physical Review B*, 89(20):201302, 2014.
- [109] G. Wang, L. Bouet, D. Lagarde, M. Vidal, A. Balocchi, T. Amand, X. Marie, and B. Urbaszek. Valley dynamics probed through charged and neutral exciton emission in monolayer WSe₂. *Physical Review B*, 90(7):075413, 2014.

-
- [110] G. Wang, E. Palleau, T. Amand, S. Tongay, X. Marie, and B. Urbaszek. Polarization and time-resolved photoluminescence spectroscopy of excitons in MoSe₂ monolayers. *Applied Physics Letters*, 106(11):112101, 2015.
- [111] M. Palummo, M. Bernardi, and J. C. Grossman. Exciton radiative lifetimes in two-dimensional transition metal dichalcogenides. *Nano Letters*, 15(5):2794–2800, 2015.
- [112] T. Korn, S. Heydrich, M. Hirmer, J. Schmutzler, and C. Schller. Low-temperature photocarrier dynamics in monolayer MoS₂. *Applied Physics Letters*, 99(10):2–5, 2011.
- [113] T. Jakubczyk, K. Nogajewski, M. R. Molas, M. Bartos, W. Langbein, M. Potemski, and J. Kasprzak. Impact of environment on dynamics of exciton complexes in a WS₂ monolayer. *2D Materials*, 5(3):031007, 2018.
- [114] D. S. Ballantine Jr, R. M. White, S. J. Martin, A. J. Ricco, E. T. Zellers, G. C. Frye, and H. Wohltjen. *Acoustic wave sensors: theory, design and physico-chemical applications*. Elsevier, 1996.
- [115] A. C. T. Covacevise. Modulation of planar optical microcavities by surface acoustic waves. Master’s thesis, University of Campinas, Campinas, Brazil, 2014.
- [116] D. Morgan. *Surface acoustic wave filters: With applications to electronic communications and signal processing*. Academic Press, 2010.
- [117] O. D. D. Couto Jr. *Acoustically induced spin transport in (110) GaAs quantum wells*. PhD thesis, Humboldt Universitat zu Berlin, 2008.
- [118] M. M. de Lima Jr. and P. V. Santos. Modulation of photonic structures by surface acoustic waves. *Reports on Progress in Physics*, 68(7):1639, 2005.
- [119] L. Rayleigh. On waves propagated along the plane surface of an elastic solid. *Proc. London Math. Soc.*, 17:4, 1885.

- [120] D. Royer and E. Dieulesaint. *Elastic Waves in Solids II: Generation, Acousto-optic Interaction, Applications*. Springer Science & Business Media, 1999.
- [121] K. A. Ingebrigtsen. Surface waves in piezoelectrics. *J. Appl. Phys.*, 40:2681, 1967.
- [122] R. S. Weis and T. K. Gaylord. Lithium niobate: summary of physical properties and crystal structure. *Applied Physics A*, 37(4):191–203, 1985.
- [123] T. Kannan. Finite element analysis of surface acoustic wave resonators. Master's thesis, University of Saskatchewan, 2006.
- [124] H. Zhu, Y. Wang, J. Xiao, M. Liu, Z. J. Xiong, S. and Wong, Z. Ye, Y. Ye, X. Yin, and X. Zhang. Observation of piezoelectricity in free-standing monolayer MoS₂. *Nature Nanotechnology*, 10(2):151–155, 2015.
- [125] N. Iguiniz, R. Frisenda, R. Bratschitsch, and A. Castellanos-Gomez. Revisiting the buckling metrology method to determine the young's modulus of 2D materials. *Adv. Mater.*, 31:1807150, 2018.
- [126] K. N. Duerloo, M. T. Ong, and E. J. Reed. Intrinsic piezoelectricity in two-dimensional materials. *J. Phys. Chem. Lett.*, 3:2871, 2012.
- [127] F. A. Benimetskiy, V. A. Sharov, P. A. Alekseev, V. Kravtsov, K. B. Agapev, I. S. Sinev, I. S. Mukhin, A. Catanzaro, R. G. Polozkov, E. M. Alexeev, A. I. Tartakovskii, A. K. Samusev, M. S. Skolnick, D. N. Krizhanovskii, I. A. Shelykh, , and I. V. Iorsh. Measurement of local optomechanical properties of a direct bandgap 2D semiconductor. *APL Mater.*, 7:101126, 2019.
- [128] M. Cardona and Y. Y. Peter. *Fundamentals of semiconductors*, volume 619. Springer, 2005.
- [129] L. S. R. Cavalcante, D. R. Da Costa, G. A. Farias, D. R. Reichman, and A. Chaves. Stark shift of excitons and trions in two-dimensional materials. *Physical Review B*, 98(24):1–6, 2018.

- [130] C. Rocke, O. Govorov, A. Wixforth, G. Böhm, and G. Weimann. Exciton ionization in a quantum well studied by surface acoustic waves. *Phys. Rev. B*, 57:R6850, 1998.
- [131] D. A. B. Miller, D. S. Chemla, T. C. Damen, A. C. Gossard, W. Wiegmann, T. H. Wood, and C. A. Burrus. Electric field dependence of optical absorption near the band gap of quantum-well structures. *Physical Review B*, 32(2):1043–1060, 1985.
- [132] B. G. Shin, G. H. Han, S. J. Yun, H. M. Oh, J. J. Bae, Y. J. Song, C. Y. Park, and Y. H. Lee. Indirect bandgap puddles in monolayer MoS₂ by substrate-induced local strain. *Adv. Mater.*, 28:9378, 2016.
- [133] M. D Tran, J. Kim, H. Kim, M. H. Doan, D. L. Duong, and Y. H. Lee. Role of hole trap sites in MoS₂ of inconsistency of optical and electrical phenomena. *ACS Appl. Mater. Interfaces*, 10:10580, 2018.
- [134] A. K. Harman, S. Ninomiya, and S. Adachi. Optical constants of sapphire (α -Al₂O₃) single crystals. *Journal of Applied Physics*, 76(12):8032–8036, 1994.
- [135] K. Datta, Z. Lyu, Z. Li, T. Taniguchi, K. Watanabe, and P. B. Deotare. Spatiotemporally controlled room-temperature exciton transport under dynamic strain. *Nature Photonics*, pages 1–6, 2022.
- [136] J. H. Hines and D. C. Malocha. A simple transducer equivalent circuit parameter extraction technique. In *1993 Proceedings IEEE Ultrasonics Symposium*, pages 173–177. IEEE, 1993.
- [137] W. R. Smith, H. M. Gerard, J. H. Collins, T. M. Reeder, and H. J. Shaw. Analysis of interdigital surface wave transducers by use of an equivalent circuit model. *IEEE. Trans. Mic. Theory and Tech.*, 11:856, 1969.
- [138] K Yamanouchi and H Furuyashiki. New low-loss saw filter using internal floating electrode reflection types of single-phase unidirectional transducer. *Electronics Letters*, 20(24):989–990, 1984.

- [139] M. K. Ekström, T. Aref, J. Runeson, J. Björck, I. Boström, and P. Delsing. Surface acoustic wave unidirectional transducers for quantum applications. *Applied Physics Letters*, 110(7):073105, 2017.
- [140] B. Achour, N. Aloui, N. Fourati, C. Zerrouki, and N. Yaakoubi. Modelling and simulation of saw delay line sensors with comsol multiphysics. In *MOL2NET 2018, International Conference on Multidisciplinary Sciences, 4th edition*, page 5887. MDPI, 2018.
- [141] D. J. Pradeep, N. R. Krishnan, and H. B. Nemade. Simulation of unidirectional interdigital transducers in saw devices using comsol multiphysics. In *Proceedings of the COMSOL Conference, Hannover, Germany*, pages 4–6, 2008.
- [142] M. M. Elsherbini, M. F. Elkordy, and A. M. Gomaa. Using comsol to model high frequency surface acoustic wave (saw) device. *Journal of Electrical and Electronics Engineering Research*, 8(1):1–8, 2016.
- [143] Q. Liu and J. Tao. The perfectly matched layer for acoustic waves in absorptive media. *The Journal of the Acoustical Society of America*, 102(4):2072–2082, 1997.
- [144] F. Cadiz, C. Robert, G. Wang, W. Kong, X. Fan, M. Blei, D. Lagarde, M. Gay, M. Manca, T. Taniguchi, K. Watanabe, T. Amand, X. Marie, P. Renucci, S. Tongay, and B. Urbaszek. Ultra-low power threshold for laser induced changes in optical properties of 2D molybdenum dichalcogenides. *2D Materials*, 3(4), 2016.
- [145] S. Tongay, J. Suh, C. Ataca, W. Fan, A. Luce, J. Kang, J. S. and Liu, C. Ko, R. Raghunathanan, J. Zhou, and Others. Defects activated photoluminescence in two-dimensional semiconductors: interplay between bound, charged, and free excitons. *Scientific Reports*, 3:2657, 2013.
- [146] J. Z. Li, J. Y. Lin, H. X. Jiang, A. Salvador, A. Botchkarev, and H. Morkoc. Nature of Mg impurities in GaN. *Appl. Phys. Lett.*, 69:1474, 1996.

-
- [147] M. Weiß and H. J. Krenner. Interfacing quantum emitters with propagating surface acoustic waves. *Journal of Physics D: Applied Physics*, 51(37):aace3c, 2018.
- [148] S. K. Zhang, P. V. Santos, and R. Hey. Photoluminescence modulation by high-frequency lateral electric fields in quantum wells. *Applied Physics Letters*, 78(11):1559–1561, 2001.
- [149] S. Larentis, B. Fallahazad, and E. Tutuc. Field-effect transistors and intrinsic mobility in ultra-thin MoSe₂ layers. *Appl. Phys. Lett.*, 101:223104, 2012.
- [150] D. Lloyd, X. Liu, J. W Christopher, L. Cantley, A. Wadehra, B. L. Kim, B. B Goldberg, A. K Swan, and J. S. Bunch. Band gap engineering with ultralarge biaxial strains in suspended monolayer MoS₂. *Nano Lett.*, 16:5836, 2016.
- [151] T. G. Pedersen. Exciton stark shift and electroabsorption in monolayer transition-metal dichalcogenides. *Physical Review B*, 94:125424, 2016.